Quality Improvement of Molecular Beam Epitaxy Grown Topological Insulator Thin Films and *in situ* Fabrication of Devices

von

Michael Schleenvoigt

Masterarbeit in Physik

vorgelegt der

Fakultät für Mathematik, Informatik und Naturwissenschaften
der RWTH Aachen

eingereicht im

November 2017

angefertigt am

Peter Grünberg Institut (PGI-9)

Forschungszentrum Jülich

bei

Prof. Dr. Detlev Grützmacher

Zweitgutachter: Prof. Dr. Markus Morgenstern

Abstract

In 2005, Kane and Mele introduced topological insulators as a new material class in the vast field of solid state physics [1]. Since then, research on the topic led to a plethora of discoveries, ranging from two-dimensional systems to many classes of three-dimensional topological insulators [2]. Topological insulators exhibit promising features, useful for example for spintronic applications or quantum computing [2–8]. However, due to large background doping, these features are often suppressed. Therefore, measures need to be taken in order to lower the doping, enhancing the topological characteristics.

In this thesis, molecular beam epitaxy grown three-dimensional topological insulators of the tetradymite crystal class, consisting of bismuth, antimony, tellurium and selenium (V_2VI_3), are investigated. In the course of the work, three points of interest in a conventional sample are investigated with regard to the possibility to improve them. These are the interface to the substrate, the bulk and the interface to the environment.

First, the interface of the grown film to the substrate has been examined. Two approaches have been pursued to influence the growth of the film. One has been the use of prepatterned samples to grow topological insulator films in fixed structures. The other has been changing the substrate material and growing thin layers of optimized films, fit to the new surfaces, as pseudo substrates for subsequent growths.

Next, the focus has been set on the bulk of the film. In order to optimize the electronic qualities of the topological insulator, a quaternary material system has been grown via molecular beam epitaxy. The quaternary system promises less background doping and has not been grown by the means of molecular beam epitaxy before.

Thirdly, the interface to ambient conditions has been investigated. To protect the surface of the film from contaminations during *ex situ* processes, a technique to fabricate devices *in situ*, the stencil lithography, has been refined. The masks used for the technique have been fabricated by etching onto structures patterned into silicon nitride.

Lastly, to conclude the two previous chapters, Hall measurements have been performed on quaternary samples with *in situ* contacts grown via the stencil lithography method. The measurements have been performed at cryogenic temperatures and resulted in values comparable to literature.

Table of Contents

1 Introduction 1

2 Theoretical Background 3

2.1 Topology 3
2.2 Two-dimensional Systems 4
2.3 Three-dimensional TIs 7
2.4 Epitaxy and TI Crystal Structure 9

3 Experimental Methods 12

3.1 Molecular Beam Epitaxy 12
3.2 X-ray Diffractometry 14
3.3 Rutherford Backscattering Spectrometry 14
3.4 Angle-resolved Photoemission Spectroscopy 15

4 The Interface Substrate-Topological Insulator 17

4.1 Selective Area Growth 17
4.2 Improving Film Quality by Substrate Choice 25

5 Optimizing the Bulk: From the Binary to the Quaternary System 33

5.1 The Tetradymite TIs 33
5.2 The Quaternary System 35

6 The Interface to the Continuum and in situ Device Fabrication 45

6.1 Protecting the Surface States: Capping 45
6.2 In situ Device Fabrication via Stencil Lithography 47
  6.2.1 First Attempts at Quasi Grown Devices 48
  6.2.2 Holder Design and Transfer 52
  6.2.3 Mask Layout and Fabrication Process 54
  6.2.4 Results 61

7 Transport Measurements 67

7.1 The VTI Cryostat and Measurement Setup 67
7.2 Characterization of the Quaternary in situ Hall Bar 69

8 Conclusion & Outlook 79

9 References I

10 Acknowledgments XI

List of Abbreviations

AFM	Atom force microscope
ARPES	Angle-resolved photoemission spectroscopy
ARXPS	Angle-resolved X-ray spectroscopy
BZ	Brillouin zone
FM	Frank-van-der-Merwe (growth)
HLN	Hikami-Larkin-Nagaoka (equation)
HNF	Helmholtz Nano Facility
IBE	Ion beam etching
MBE	Molecular beam epitaxy
PGI	Peter Grünberg Institute
QHE	Quantum Hall effect
QSHE	Quantum spin Hall effect
RBS	Rutherford backscattering spectrometry
RHEED	Reflection high-energy electron diffraction
SEM	Scanning electron microscope
SK	Stranski-Krastanov (growth)
SOC	Spin orbit coupling
TEM	Transmission electron microscope
TI	Topological insulator
2DTI	Two-dimensional topological insulator
3DTI	Three-dimensional topological insulator
STI	Strong topological insulator
WTI	Weak topological insulator
TRIM	Time reversal invariant momentum
TRS	Time reversal symmetry
VW	Volmer-Weber (growth)
WAL	Weak anti-localization
WL	Weak localization
XRD	X-ray diffractometry
XRR	X-ray reflectometry

1 Introduction

In the vast field of condensed matter physics, topological insulator (TI) materials are a relatively young class, first predicted by Kane and Mele in 2005 [1]. Shortly after, Bernevig *et al.* independently proposed the existence of topological states in two-dimensional quantum-wells [9]. Since its discovery, the topic experienced rapid growth in many directions due to its peculiar qualities. First and foremost, most topological insulators exhibit a gapped insulating behavior in the bulk, combined with gapless surface states. Due to the topology of the electronic bands surface states arise, which are protected by time reversal symmetry (TRS) and display a Dirac-like, helical dispersion with spin locked momentum due to spin orbit coupling [2]. The topological aspect of the surface states with TRS protection distinguishes the surfaces states of the TI from surface states that are possible on conventional semiconductors. The latter can be removed by potential disorders on the surface, for example due to disorder, while the former are robust and cannot be removed. The spin locked momentum signifies that if an electron scatters and changes its momentum, it is obliged to also change its spin. This leads to a decrease in scatter probability, effectively prohibiting backscattering [6]. Therefore, TIs are a promising material for spintronic devices [7].

Equally promising is the combination of TI materials with superconductors. Via the proximity effect, superconducting properties can be induced into a topological insulator. Since the spin in a topological insulator is fixed to the momentum, the spin degree of freedom is essentially lost. Therefore, the newly created system of a topological superconductor is predicted to show spin-non-degenerate superconductivity. Fu *et al.* proposed in 2008 that such a superconductive state harbors so called Majorana fermions [10, 11]. These exotic quasiparticles are of high interest for applications in quantum computing [2–5].

There are two-dimensional (2DTI) and multiple types of three-dimensional TIs (3DTI), for example weak and strong 3DTIs [12]. All show the distinct property of having topologically protected surface states. In 2DTIs, the surface states emerge as one-dimensional edge channels, while in the 3DTIs, they appear as two-dimensional surfaces, however not necessarily on all crystal surfaces [13]. An example for a 2DTI is a HgTe/CdTe quantum well [9, 14]. The earliest 3DTI is Bi_xSb_{1-x}, whose discovery in 2007 was quickly followed by those of Bi_2Te_3, Bi_2Se_3 and Sb_2Te_3 [15, 16]. Nowadays, ternary and quaternary compounds consisting of combinations of Bi, Sb, Te and Se join the binary compounds in the research on 3DTIs. The latter mentioned 3DTIs crystallize in a tetradymite structure and are often subjected to high levels of background doping due to their elaborate chemistry [2]. This suppresses the impact of the surface states on the transport, since the bulk contributes many charge carriers, although being named insulating. Reducing the bulk contributions by improving the film qualities is thus the goal of this work.

This thesis consists of six major parts. In the following first part, the theoretical background of topological insulators will be explained. Moreover, the growth mechanics and the crystal structure of the investigated TIs will be briefly detailed. In the third chapter, the experimental methods utilized for this work will be introduced. The following three chapters will concentrate on the three points of interest in a topological insulator thin film device.

First, in the fourth chapter, the interface of the film to the substrate will be investigated. This includes the choice of substrate as well as modifications of the latter, i.e. prepatterned substrates. Growth series will be performed to test, whether the right substrate can facilitate better TI films and whether patterned substrates can be used to selectively grow TIs in a molecular beam epitaxy chamber (MBE). The fifth chapter will address the bulk of the TI film, the second point of interest. As previously mentioned, tetradymite TIs struggle with high background doping due to defects in the crystal. Quaternary TIs are predicted to overcome this problem, but have yet only been produced by the Bridgman method. Therefore, attempts are undertaken to fabricate a quaternary TI in the MBE chamber of the Peter-Grünberg-Institute 9 (PGI-9). The last point of interest, the interface between the surface of the TI and ambient conditions, is investigated in the sixth chapter. There, the influence of capping will be explained and the corresponding prerequisite of protecting the surface of the TI from ambient contaminations will be satisfied by the development of a stencil lithography technique for *in situ* device fabrication. The fabrication of patterned membranes used as stencils or masks for the realization of the lithography technique will also be illustrated. Finally, in chapter 7, transport measurement results on an *in situ* grown quaternary device will be shown and evaluated, verifying the applicability of the methods developed in the previous chapters.

2 Theoretical Background

In this chapter, the theoretical foundations of topological insulators and epitaxial growth will be explained**.** First, the concept of topology will be generally explained, before the second paragraph will deal with the concept and effects of topology in two-dimensional systems. Lastly, the concept will be generalized to three dimensional systems in the third section. The explanation of topological insulator theory will follow that of M. Eschbach's Ph. D. thesis and M. Morgenstern's script of his lecture on the topic during the 48th IFF spring school [17, 18]. In a fourth and separate section, the growth of topological insulator crystals via molecular beam epitaxy and their crystal structure will be discussed.

2.1 Topology

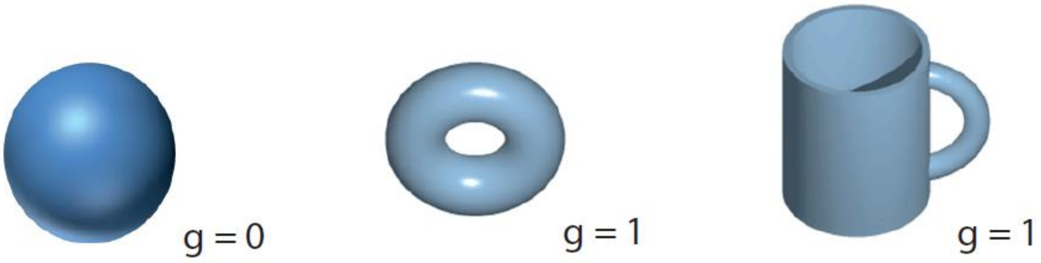

Fig. 2.1: *The genus g of different bodies determines whether they can be continuously deformed into each other. Figure adapted from [17].*

Topology is first and foremost a mathematical concept. The mathematical framework provided by the field of topology allows for the description and calculation of properties of objects that are continuously deformed. The latter includes the twisting, stretching or deformation of objects, but not discontinuous deformations like tearing. The most famous example of this is shown in Fig. 2.1. A cup is a continuous, or homeomorphous, deformation of a donut, but in order to form a donut from a sphere a hole has to be made, which would be a discontinuous operation. In mathematics, the three objects are identified by their surface and united in the class of bodies (M). The genus g of a body M then counts the number of discontinuities in the body, for the sphere g = 0, for the donut g = 1 [19]. An example for a g = 2 body is the number 8.

That the topological concept can also be applied to more abstract spaces was shown in theory by Thouless, Kosterlitz, Haldane *et al.* in the time from 1972 to 1983 and was rewarded with the Nobel Prize in Physics in 2016 [20, 21]. One example for such a space is the $\boldsymbol{k}$ space of the electrons, including a complete set of quantum numbers, which forms the relevant Hilbert space [18]. In $\boldsymbol{k}$ space, the band structure arising from the electron wave functions in a solid state system can thus be categorized similarly to geometrical objects. Therefore, a topological invariant $n \in \mathbb{Z}$ is defined. In this picture, a trivial insulator would have $n = 0$, like the genus g = 0 of the sphere, and the topological insulator with surface states would possess $n = 1$, similar to g = 1 of the torus. Thus, the two systems cannot be transformed into each other without discontinuities, which in this case would be a closing and opening of the band gap [13, 17].

2.2 Two-dimensional Systems

One of the first manifestations of a topologically protected state is the integer quantum Hall effect (QHE). It emerges when electrons are confined in two dimensions and exposed to a strong perpendicular magnetic field at low temperatures. Due to the field, the electrons move in quantized circular paths, resulting in an insulating bulk. At the boundary of the sample however, the electrons are reflected back into the sample, resulting in non-closed loops and therefore in a drift of the electrons along the edge without bias. In a Hall probe, this leads to a longitudinal resistance σ_{xx} equal to zero, while the Hall conductance shows a quantized behavior of $\sigma_{xy} = N \cdot \frac{e^2}{h}$ as shown by von Kitzling in 1980, who called N the filling factor [22]. That this bulk insulating and edge channel conductive system is different from trivial insulators not only due to quantum mechanical effects, but also due to topology, was shown two years later by Thouless, Kohmoto, Nightingale and Nijs (TKNN) [17, 20]. They introduced the TKNN invariant n, which was later shown to be identical to the filling factor N and therefore also to the Chern number C that can be related to the previously explained genus g via the Berry phase γ. If a closed path is performed in the parameter space of a quantum-mechanical system, the system acquires an additional phase, the Berry phase γ, denoted by the integral in equation (2.I). The Chern number C is then the sum of all Berry phases in the Brillouin zone (BZ), the primitive cell of a crystal's reciprocal space, via

$$C = \sum_{m=1}^{r} C_m = \sum_{m=1}^{r} \frac{1}{2\pi} \cdot \oint_{\partial BZ} d\boldsymbol{k}\, \nabla_{\boldsymbol{k}} \times \boldsymbol{A}_m(\boldsymbol{k}) \tag{2.I}$$

where r is the number of occupied bands in the BZ, ∂BZ signifies the BZ boundary and

$$\boldsymbol{A}_m(\boldsymbol{k}) = i\langle u_m(\boldsymbol{k})|\nabla_{\boldsymbol{k}}|u_m(\boldsymbol{k})\rangle \tag{2.II}$$

denotes the Berry connection. $|u_m(\boldsymbol{k})\rangle$ describes the Bloch wavefunctions of an electron in a crystal, depending on the wave vector $\boldsymbol{k}$. The integrand in (2.I) is also called the Berry curvature. Evaluating the integral for a trivial insulator results in zero, since the wavefunction does not accumulate a phase while

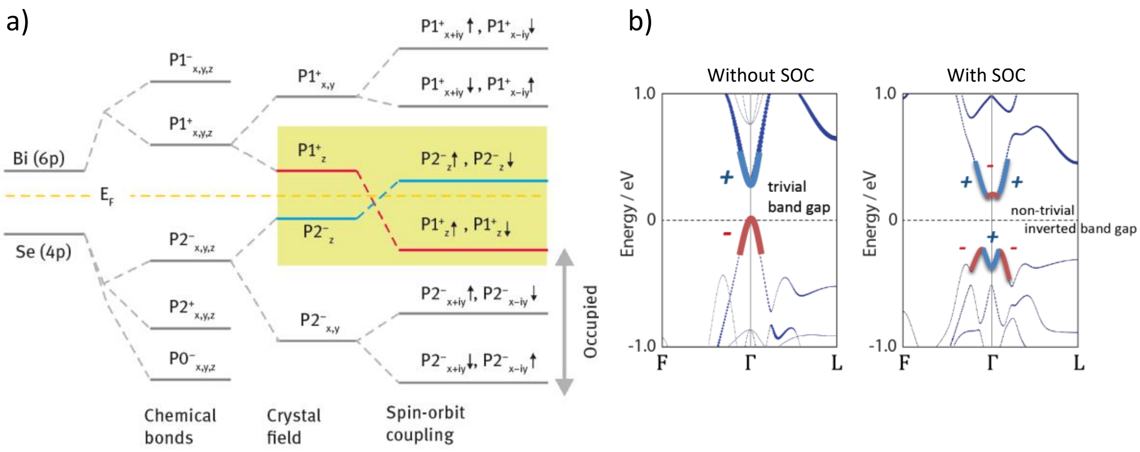

Fig. 2.2: *a) Bulk energy level structure of Bi_2Se_3. Due to chemical bonds, crystal field splitting and spin-orbit coupling, the otherwise degenerate energy levels of different p-type orbitals are shifted. If the SOC is strong, a band inversion occurs and the system is transformed into a topological phase. Figure taken from [6]. b) Calculated inverted band structure of Bi_2Te_3 with and without SOC. (+) and (–) denote the parity of the band. Adapted from [17].*

performing a closed loop, thus $C = 0$. In the case of the QHE, a phase of $\gamma = 2\pi m$, with $m \in \mathbb{Z}$, is acquired, resulting in a $C \neq 0$. Thouless *et al.* thereby showed, that the QHE can be based off a topological effect, which is protected by that topology [17, 20].

An important feature that distinguishes the QHE topologic insulator from the topological insulators considered in this work is the time reversal symmetry (TRS). The QHE discussed in the previous paragraphs exhibits no TRS, since it is broken by external magnetic fields. However, in 2005 Kane and Mele showed that this effect can be bypassed if strong spin orbit coupling (SOC) is present [1]. The SOC only influences bands with an orbital number $l \neq 0$ and results in a splitting of the otherwise degenerate spin states. The higher l, the stronger is the SOC, for example in p- or d-type bands ($l = 1$, 2 respectively). If the band gap of a semiconductor is not very large or the SOC especially strong, the valence band can cross the conduction band in $\boldsymbol{k}$ space. In Fig. 2.2 a), such a band crossing is shown for Bi_2Se_3, where due to chemical bonds, crystal field splitting and lastly SOC, the hybridized p-type bands of Bi and Se cross. This crossing causes a transition from an insulator with a trivial band gap to an insulator with a non-trivial inverted band gap in the entire bulk, as illustrated in Fig. 2.2 b) using the example of the calculated band structure of Bi_2Te_3. At the interface of such a non-trivial insulator to a trivial one, gapless states arise, since the topologic invariant describing the system can only be changed by closing and opening the band gap.

Due to the SOC, these gapless states are spin polarized, effectively locking the spin to its momentum. The locking affects the electrons so that spins of opposite direction also have

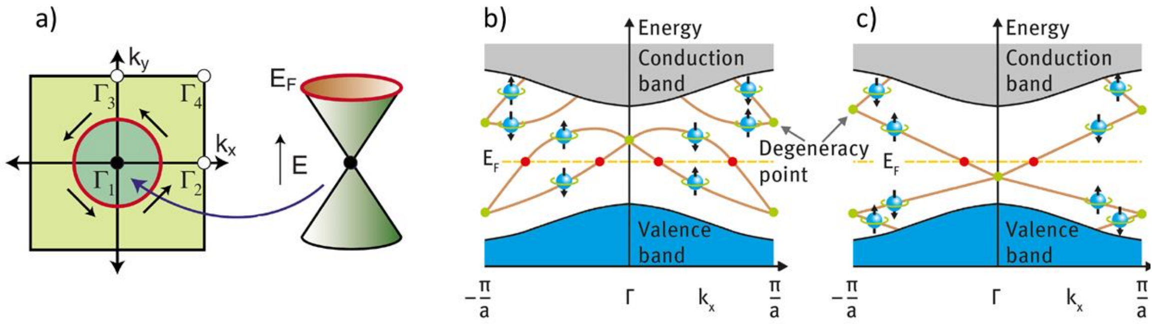

Fig. 2.3: *a) Top view of a two-dimensional Brillouin zone. The black point illustrates a Dirac point at a TRIM. The red circle indicates the cut of the Fermi level, with polarized spins due to spin-momentum locking. The Dirac cone on the right can be seen when expanding the 2D. Figure adapted from [23]. In b) and c), the band structure going from one TRIM to another is shown for the two cases of a) pairwise and b) changing connections. Figure adapted from [6].*

opposite momentum along the boundary, which is why they are called helical. Moreover, the helical spin momentum locking causes a strong suppression of backscattering. If an electron was to backscatter at a non-magnetic impurity, the spin would have to flip adiabatically. However, since the wave function acquires a phase of π from one full rotation, the interference is destructive and therefore only transmission is allowed [17, 18].

As no magnetic field needs to be applied and only time reversal invariant SOC is involved in this effect, in contrast to the QHE, the process is time reversal symmetric. Moreover, no charge is transported, because the amount of charge carriers that are transported through the edge channels in opposite directions is the same. However, a net spin transport takes place, which is why the effect was called quantum spin Hall effect (QSHE) [1, 9]. Since the Hall conductance σ_{xy} is 0 if no charge is transported, the filling factor N, the Chern number C and therefore also the TKNN invariant n are 0 in the QSHE. Thus, the non-trivial QSHE is indistinguishable from a trivial insulator. To compensate this problem, Kane and Mele established the $\mathbb{Z}_2$ topological invariant v_0 [24]. In topologically non-trivial systems with TRS $v_0 = 1$, in systems without $v_0 = 0$.

In order to identify the insulators with the invariant, first the effect of the time reversal operator on spin ½ particles in TI surface states has to be investigated. Applying the reversal operator Θ on the Hamiltonian of a $\boldsymbol{k}, \uparrow$ electron leads to

$$\Theta\mathcal{H}(\boldsymbol{k},\uparrow)\Theta^{-1} = \mathcal{H}(-\boldsymbol{k},\downarrow), \tag{2.III}$$

when Θ commutes with $\mathcal{H}$. The result of (2.III) is that every time-reversed Bloch energy eigenstate $|\psi_n(-\boldsymbol{k},\downarrow)\rangle$ is an eigenstate to the same energy as the unreversed eigenstate $|\psi_n(\boldsymbol{k},\uparrow)\rangle$. This finding is called Kramer's theorem, which states that every system with time reversal symmetry is required to exhibit a state at $-\boldsymbol{k}$ for every $E(\boldsymbol{k})$ with opposite spin and the same energy, which is therefore at least two-fold degenerate with regard to the energy [6]. SOC lifts the degeneracy, since different spin directions are affected separately. However, at special points in the Brillouin zone the spin directions are additionally degenerate. These points are called time reversal invariant momentum (TRIM) points and Dirac points can occur at their positions, as illustrated in Fig. 2.3 a). The figure shows the TRIM points in a square two-dimensional Brillouin zone, the black dot at Γ_1 indicates a Dirac point. In Fig. 2.3 b) and c) the one-dimensional projection of Fig. 2.3 a) from $\Gamma_1$to Γ_2 is shown, where $\Gamma_2$is located at $\pm\frac{\pi}{a}$, with a being the lattice constant of the system. As previously mentioned, at the interface from a topologically trivial to a non-trivial material, the band gap needs to be closed and opened again, resulting in the existence of boundary states or edge states. Due to Kramer's theorem, these states need to be degenerate at TRIM points, as indicated by the green dots in Fig. 2.3 b) and c). At momenta between TRIMs, SOC lifts the degeneracy. The difference between Fig. 2.3 b) and c) is how the edge states connect between degeneracy points. Either they connect pairwise with other degeneracy points as in b), or they connect with the valence and conduction bands and switch partners as in c). In the former case of b), the Fermi level always lies in a range of energy where no states are present in the band structure or where it cuts the edge states an even number of times. Therefore, the material is effectively band gapped and thus topologically a normal band insulator with $v_0 = 0$. In c) however the Fermi level cuts the band structure an uneven number of times from Γ_1 to Γ_2, wherever it is shifted to in the band gap. Thereby they are topologically non-trivial with $v_0 = 1$ and the surface is electronically akin to a metal. Hence, if $v_0 = 1$, a change in topology from one Γ to another is present and this leads to time reversal symmetry protected edge states with an uneven number of Fermi level cuts, making the system a topological insulator [13, 17].

2.3 Three-dimensional TIs

To generalize this concept of Kane and Mele to three dimensions, Kane and Fu developed a system of four $\mathbb{Z}_2$ invariants $v_0; (v_1 v_2 v_3)$ [15]. v_0 is the same as in the previous paragraph and called the strong topological invariant. v_{1-3} are similar to Miller indices and can be used to define a specific surface of a three-dimensional crystal. Fu and Kane illustrated the principle of the invariants on the Brillouin zone of a simple cubic lattice. The BZ contains 8 bulk TRIMs, one on each corner of the cube, and every bulk TRIM possesses a certain parity, determined by the curvature of the occupied bulk bands at the TRIM. The parity is either (+) or (-), as shown in Fig. 2.4. In the picture, four different ways to arrange the parities are shown. Additionally, the projection in the (100) direction indicating surface TRIMs is illustrated, for which the parities of the combined TRIMs are

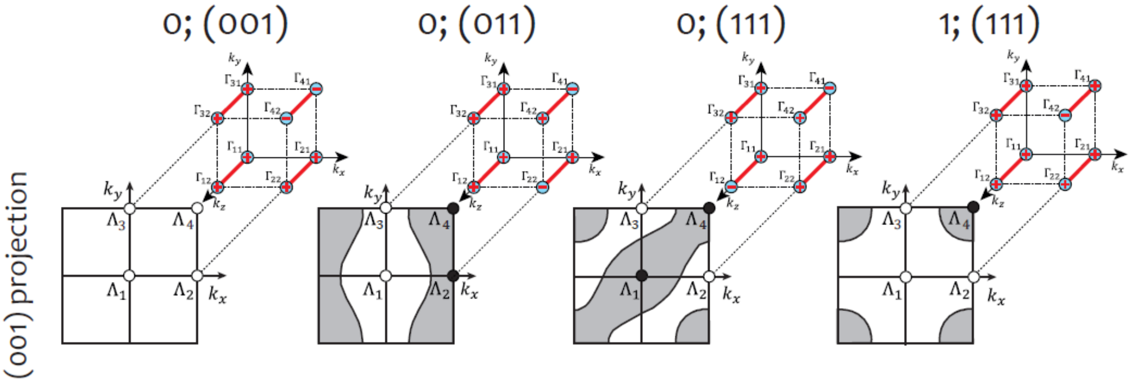

Fig. 2.4: *TRIMs in a three-dimensional cubic bulk Brillouin zone with different parities, indicated by (+) or (-). The two-dimensional projection of the BZ along the (001) direction shows the surface BZ. The parities of the TRIMs (+/white and -/black) are calculated by multiplying the parities connected by the red lines. Grey and white areas denote regions of different topology. Figure taken from [17].*

multiplied. In the first case, this leads to only positive parities (white dots), in the second there are two negative parities (black dots). When going from a positive (white area) to a negative parity (grey area), the topology has to change, resulting in spin-polarized TRS protected surface states, indicated by the black lines in Fig. 2.4, as in the previous section.

If only one TRIM in the surface projections is negative, as in 1;(111) in Fig. 2.4, a circular boundary is formed around it, which forms the so called Dirac cone of allowed electron states in the gap. This case and the cone are also shown in Fig. 2.3 a), where the black Dirac point illustrates a different parity, while the red circle indicates the circular boundary at which the Fermi level cuts the Dirac cone. The 1;(111) case is the only case in which the three-dimensional system does have an odd number of negative TRIMs (Dirac cones) on every possible surface.

To calculate the $\mathbb{Z}_2$ invariants, the parities $\delta(\Gamma)$ of the specific TRIMs need to be multiplied. For v_{1-3} the TRIMs are depending on the chosen projection plane as in (2.IV), for the v_0 invariant all are multiplied at once as in (2.V)

$$(-1)^{v_{k=1,2,3}} = \prod_{l_{i\neq k}=0,1;l_k=1} \delta(\Gamma_{l_1,l_2,l_3}), \tag{2.IV}$$

$$(-1)^{v_0} = \prod_{i=1}^{8} \delta(\Gamma_i). \tag{2.V}$$

l_1, l_2 and l_3 in (2.IV) are based off the primitive reciprocal space vectors $\boldsymbol{b_i}$ to describe the positions of the TRIM points via

$$\Gamma_{i=(l_1,l_2,l_3)} = \tfrac{1}{2}(l_1\boldsymbol{b_1} + l_2\boldsymbol{b_2} + l_3\boldsymbol{b_3}). \tag{2.VI}$$

Thus, topological insulators can be identified by their combination of the $\mathbb{Z}_2$ invariants $v_0; (v_1 v_2 v_3)$. If $v_0 = 1$, the topological insulator is called strong (STI) and all surfaces of the crystal exhibit robust spin polarized Dirac cones and therefore surface states. If $v_0 = 0$ and all $v_i = 0$, then the crystal is a trivial insulator. Is at least one $v_i \neq 0$, then it is a weak topological insulator (WTI), exhibiting surface states only on some surfaces of the crystal. The respective surfaces are indicated by which v_i are non-zero.

2.4 Epitaxy and TI Crystal Structure

The crystalline materials investigated in this work are fabricated utilizing molecular beam epitaxy. The process itself and the chamber used for the deposition of films is explained in chapter 3.1. This section will deal with the growth modes that are possible in a molecular beam epitaxy chamber. Moreover, the tetradymite crystal structure of the topological insulators examined in this work will be investigated.

In the molecular beam epitaxy chamber, the elements for the growth are evaporated onto a heated substrate. There, they condense and form crystallites of varying form and structure. According to Markov, the term epitaxy denotes the process of “oriented growth of a crystalline material on the single crystal surface of a different material” [25]. Which type of growth is preferred on the substrate depends dominantly on the relationship of the free energies involved. The latter are the surface free energy γ_S, the interface free energy γ_I and the free energy of the deposited material γ_D. The different growth modes possible by combinations of the free energies are illustrated in Fig. 2.5. If the deposited material and the substrate are the same, the process is called homoepitaxy and γ_I is 0. Moreover, γ_S and γ_D are equal. The resulting growth is called Frank-van-der-Merwe (FM) growth and illustrated in the middle column of Fig. 2.5 [26]. Neat layers of the deposited material form on the substrate, covering it uniformly and fully. If the substrate and the deposited materials are not the same, the growth process is called heteroepitaxy. In this case, there are two more possible growth mechanisms additional to FM growth. The first is the Vollmer-Weber (VW) growth, in which the surface free energy is lower than the other two combined, i.e. $\gamma_S < \gamma_I + \gamma_D$ [27, 28]. Therefore, the energy yield for a deposited adatom is higher when adhering to an already present deposit, leading to the formation of crystal islands as in the left column in Fig. 2.5. The last growth mode is the Stranski-Krastanov (SK) growth, which is a combination of the former two [29]. First $\gamma_S > \gamma_I + \gamma_D$, so that the adatoms adhere to the substrate’s surface. However, due to the different materials, strain is induced into the layers, leading to additional energy stored in the grown layers. At a critical point, the strain is high enough to cause a

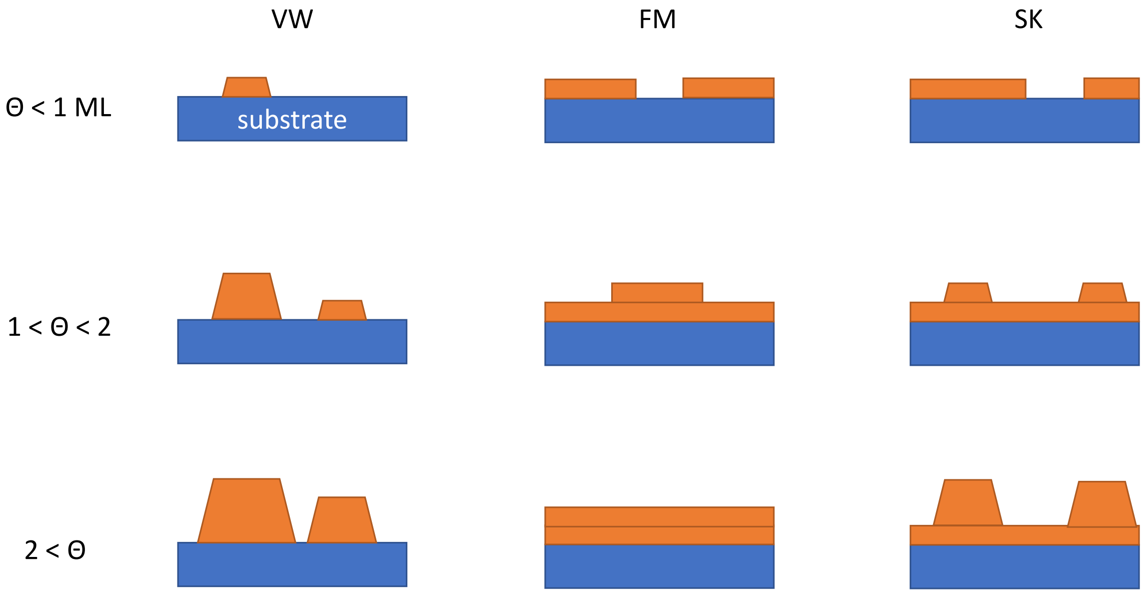

Fig. 2.5: *Progression of the growth of a crystal (orange) on a substrate consisting of a different material (blue). Θ denotes the portion of the covered surface in multiples of the number of monolayers. From left to right, the growth mechanisms are the Vollmer-Weber (VW), the Frank-van-der-Merwe (FM) and the Stranski-Krastanov (SK) growths.*

reversion of the free energies, resulting in $\gamma_S < \gamma_I + \gamma_D$ and thus island formation as in the right column of Fig. 2.5. This identification of growth processes via the free energies was summarized by Bauer. However, the processes take place at thermodynamic equilibrium, which is not the case for molecular beam epitaxy processes [25, 28, 30].

Nonetheless, the growth of topological insulators performed in this work can be compared to the FM growth due to the phenomenon of van-der-Waals growth. As shown by Koma in 1992, materials with layers held together by the van-der-Waals force are able to overcome high strains, which would conventionally lead to a VW or very rough SK growth [31]. At the interface to the substrate a conventionally bonded layer forms, which can be highly strained. The next layer of the growth is van-der-Waals bonded, thus a van-der-Waals gap exists between the layers, as shown in Fig. 2.6 a). Since only little structural information is translated through the gap, the next layers are under decreasingly lower stress. Therefore, FM growth is possible even with high lattice mismatches. However, high lattice mismatches still have influence on the initial layers and can therefore influence the further growth [16, 32, 33]. This effect will also be addressed in chapter 4.2.

Van-der-Waals bonded layers are also present in the tetradymite V_2VI_3 topological insulators investigated in this work, where V and VI denote the main-group of the elements. The crystal structure is characterized by the D_{3d}^5 $(R\bar{3}m)$ space group [16]. The heavy group V elements lead to the band inversion mentioned in the previous sections due to the arising strong spin orbit coupling. The crystals are composed of stacked quintuple layers. A quintuple layer consists of five covalently bonded layers in the

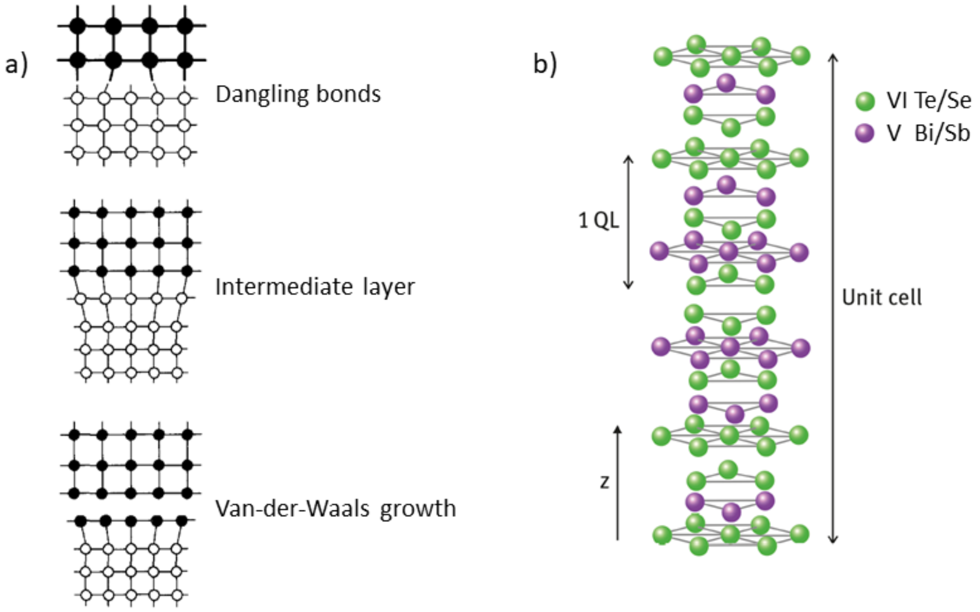

Fig. 2.6: *a) Growth modes of materials on substrates with a differing lattice constant. In the first, dangling bonds persist, while in the second an intermediate strained layer exists. Lastly, a strained first layer is created, which is bonded to subsequent layers via the van-der-Waals force, creating van-der-Waals gaps. Adapted from [31]. b) Basic unit cell of the tetradymite topological insulator crystals, illustrating the quintuple layered structure. Van-der-Waals gaps exist between the VI element double layers. Figure adapted from [6].*

sequence VI-V-VI-V-VI in z direction as illustrated in Fig. 2.6 b) [2]**.** The quintuple layers are bound by the weak van-der-Waals force, since each quintuple layer is chemically stable, resulting in an easily cleavable structure [16]. Three quintuple layers make up one unit cell of the crystal, which is shown in Fig. 2.6 b). The unit cell is roughly 3 nm high, with each quintuple layer contributing 1 nm, depending on material composition. The $\mathbb{Z}_2$ invariant in these systems is 1;(000), thus they exhibit a Dirac cone at the Γ point of the BZ on all surfaces [2].

In the last sections, the theoretical concepts of topological insulators and their growth in an MBE, which are the foundation of this work, have been established. The next chapter will introduce the experimental methods used to fabricate and examine the grown topological insulator films.

3 Experimental Methods

In this chapter, the methods utilized to fabricate and characterize the topological insulators thin films will be introduced. This includes the molecular beam epitaxy of TI thin films, the x-ray diffractometry used to investigate the crystal structure and Rutherford backscattering spectrometry, which is employed to determine the TI's stoichiometry. Lastly, the method of angular resolved photo emission spectroscopy to investigate the topological insulators band structure is introduced.

3.1 Molecular Beam Epitaxy

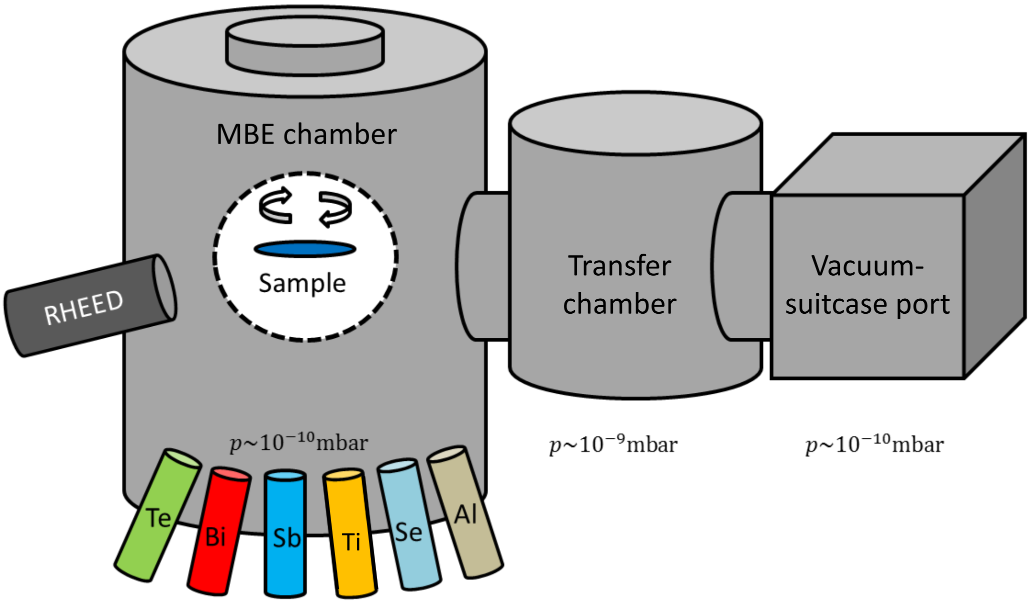

Fig. 3.1: *Diagram of the MBE setup of the PGI-9. The sample is loaded into the load lock (not shown) and moved to the growth chamber (MBE chamber) or to the vacuum-suitcase port via a manipulator in the transfer chamber. The MBE chamber is equipped with six effusion cells and a RHEED system to investigate the deposition during growth. Adapted from [28].*

The three dimensional topological insulators investigated in this work are grown by molecular beam epitaxy (MBE) in an evacuated chamber shown in Fig. 3.1. MBE is a versatile procedure to fabricate thin films of various elemental compounds with thicknesses from less than 1 nm to several 100 nm. In order to grow the films, crucibles filled with the desired materials are heated up with integrated coils to evaporate the material and reach a specific partial pressure, which forms the molecular beam. Such cells are called Knudsen cells. The Knudsen cells and the contained materials are indicated by the colored cylinders in Fig. 3.1. Since no devices to measure the partial pressure directly, or rather the resulting element flux, were installed in the MBE chamber used for this study, the temperature of the effusion cell is the essential parameter and used to set the growth rates as well as the compound ratios. The chamber used for this work consists of three parts, a load lock, a transfer chamber and finally the growth chamber. They are separated by pressure driven shutters, between which the samples are transferred with a manually operated manipulator. In the chambers, the operating pressures are $p = 10^{-8}$, 10^{-9} and 10^{-10} mbar respectively. These low pressures are needed to guarantee clean surfaces without oxidation of the surface layers and are achieved by a turbo pump and liquid nitrogen cooling of the chambers walls. A fourth part, the vacuum-suitcase port, is evacuated to $p = 10^{-8}$ when a suitcase for transfers is attached, c.f. Fig. 3.1. Inside the growth chamber, the sample is held underneath a graphite substrate heater, which can reach temperatures up to $T_S = 1000$ °C, by a rotatable rack with a rotation frequency set to 0.2 Hz. The molecular beam sources are mounted to the bottom of the chamber. Deposition of material is thus done on the downwards facing surface of the sample, hence the sample is built in upside down. Since molecular beam epitaxy is a directed technique only on this side films are grown. For the growth of topological insulators, a bismuth, an antimony, a tellurium and a selenium cell are incorporated, while for the deposition of contacts and capping an aluminum and a titanium cell are present in the setup. Additionally, a reflection high-energy electron diffraction (RHEED) system is included in the chamber, which can be used to observe the formation of the TI on the silicon. However, there is only a screen incorporated in the MBE, not an electronic detector, so that data cannot be extracted from the RHEED patterns.

Growth in the MBE chamber is performed on silicon (Si) and indium phosphide (InP) substrates oriented in the (111) direction, as this surface is akin to the topological insulator's surface. The Si substrates are cleaned before growth in the class 10 cleanroom of the Helmholtz Nano Facility (HNF). First the samples are dipped into a mixture of two parts sulfuric acid with 96 % concentration and one part hydrogen peroxide with 31 % concentration for 10 minutes. This process removes possible organic contaminations by forming an oxide layer on the substrate. This oxide layer is then removed in the second step by a 5 minute dip into hydrofluoric acid (HF) with 1 % concentration. This not only removes the oxide, but also forms a hydrogen passivated silicon surface. By heating up the cleaned sample in the MBE before growth to a temperature of 700 °C, the passivation is removed and a clean Si (111) surface is prepared. The InP substrates are cleaned with HF only, as the sulfuric acid destroys the samples. Tarakina *et al.* showed that using highly concentrated HF to create a rough surface on the InP substrate results in a smooth and domain reduced growth of Bi_2Se_3, which is why 10 % HF is used to clean the samples [32]. The dip is done for 20 min to ensure a clean and roughed up surface.

3.2 X-ray Diffractometry

The X-ray diffractometry (XRD) measurements shown in this work are performed with a BRUKER D 8 DISCOVER diffractometer. To generate the x-rays for investigations, electrons are accelerated towards a copper anode by an electric field, which results in x-rays with the characteristic Kα_1 energy and wavelength of copper (1.54 Å). The radiation is then guided through a monochromator and pointed onto the crystalline sample. The reflected x-rays are measured by a detector. Depending on the crystal lattice, the lattice constants and the angle θ of the x-ray to the sample, destructive or constructive interference is measured.

$$n \cdot \lambda = \frac{2\, a_0 \sin\theta}{\sqrt{h^2 + k^2 + l^2}} \tag{3.I}$$

Via Bragg's equation (3.I), the Miller indices (hkl) of the constructive interference peaks can be determined, which give information about the crystal lattice structure. In the equation, n is a positive integer, λ is the wavelength of the x-ray radiation and a_0 denotes the lattice constant. By rotating the sample about the Euler angles, reciprocal space maps and ϕ scans of the investigated crystal can be measured. Moreover, X-ray reflectivity (XRR) measurements can performed to determine the thickness of the deposited thin films.

3.3 Rutherford Backscattering Spectrometry

Rutherford backscattering spectrometry (RBS) is a method used to determine the stoichiometry of thin films or of the surface of bulk samples. Light atoms like hydrogen or helium are accelerated towards the surface of the sample, where an elastic, hard-sphere collision is provoked. A detector records the scattered ions and their energy. During the scattering, a certain amount of energy is transferred to the target atoms, so that the initial ion energy E_i is reduced to E_f, which are connected by:

$$E_f = k \cdot E_i \tag{3.II}$$

The factor *k* is called the kinematical factor and can be calculated by:

$$k = \left(\frac{m_1 cos\theta \pm \sqrt{m_2^2 - m_1^2 (sin\theta)^2}}{m_1 + m_2} \right)^2 \tag{3.III}$$

In the equation (3.III), m_1 and m_2 denote the masses of the projectile and the target atom, respectively, and θ the scattering angle. Since the highest energy transfer and therefore the lowest *k* is preferred to obtain a high mass resolution, the angle θ is usually set to nearly 180°, which is also the reason for the name backscattering. Since E_i, m_1 and θ are known, the mass of the target atom can be determined by measuring E_f and solving the equation for m_2. The stoichiometry of the investigated sample is calculated by counting the number of signals in the peak of each element. The distinct portions are then set in proportion to the absolute number of signals, resulting in the percentages of an element in the compound.

3.4 Angle-resolved Photoemission Spectroscopy

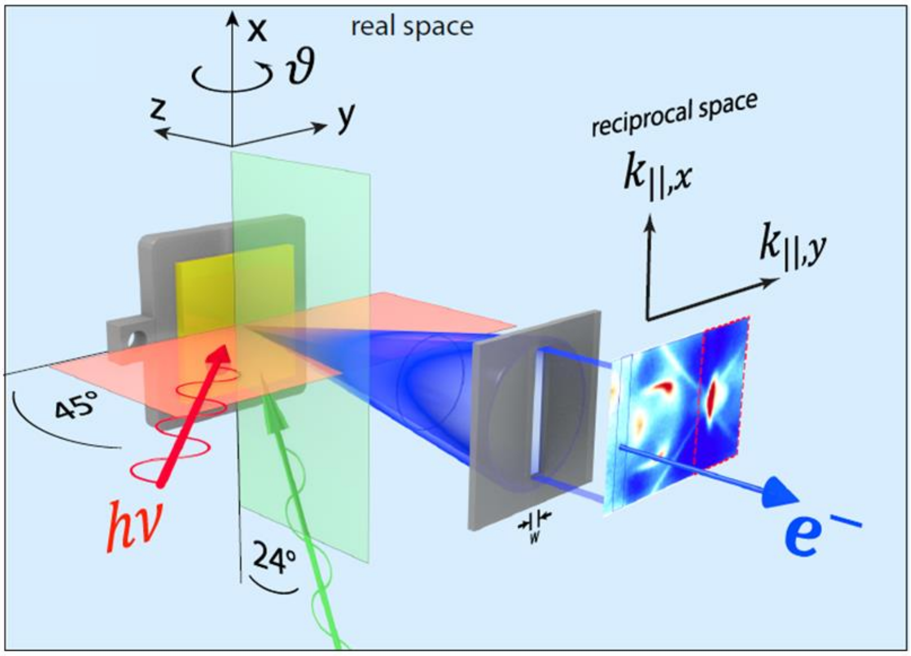

Fig. 3.2: *Diagram of the functionality of ARPES. Light from a helium (red) or xenon (green) lamp irradiates the surface to be investigated. The electrons freed from the samples band structure due to the photoelectric effect pass through a slit and are detected resolved by their momentum. Taken from [28].*

As the Dirac cone is the prominent feature of topological insulators, investigating it is of high importance. To measure the electronic band structure and therefore the Dirac cone, angle-resolved photoemission spectroscopy (ARPES) is performed. ARPES provides information about the surface and the bulk band structure respectively. Measuring a clear band structure moreover indicates a high crystallinity of the grown topological insulator film.

For ARPES, which is a highly surface sensitive technique, the sample is irradiated with light from a helium or xenon lamp. The photon energies are 21.2 eV and 8.4 eV respectively. Due to the photoelectric effect, electrons are excited to high energy levels, which enables them to leave the sample electronic structure. The electron is emitted with a specific momentum and direction, which reveals information about the k-vector of the electron in the solid. With this information and specific sample rotations, it is possible to construct a three-dimensional image of the electron band structure in the sample. Since the kinetic energy of the photons from the xenon lamp is lower, they possess a longer inelastic mean free path according to the universal curve of the inelastic mean free path [17]. Thus, the xenon photons can penetrate deeper into the sample, resulting in a higher bulk sensitivity, in contrast to the highly surface sensitive helium photons.

These are the experimental methods that are used to fabricate or characterize the topological insulator films and devices investigated in this work. In the next chapters, the measurements done with them will be shown in more detail. As mentioned before, this work will concentrate on the three sites of interest in a topological insulator thin film. These are the bottom of the film, i.e. the interface to the substrate, the bulk and lastly the top of the film, the interface to the continuum. In the following chapters, the problems that arise in these regions will be illustrated and the solutions found to the problems will be explained. From the bottom to the top, the first area will be the bottom interface.

4 The Interface Substrate-Topological Insulator

The interface between the topological insulator and the substrate may at first seem negligible, as most measurements are performed on the top surface of the film, however this is not the case. Electrical transport measurements, which in an ideal TI would only probe the surface as the bulk is supposedly insulating, show that both the top and the bottom surfaces are probed [34]. Therefore, both interfaces should be optimized for transport measurements. Moreover, the bottom interface is important for the growth of the topological insulator, even though the van-der-Waals growth can compensate many obstacles like lattice mismatches [28, 32]. Not only that, but by applying additional layers of materials like silicon oxide or silicon nitride to the substrate and structuring them, it is possible to grow TI films selectively [33]. Therefore, in the following chapter, approaches to improve growth conditions and the development of prestructures for growth will be explained in detail.

4.1 Selective Area Growth

The applications of topological insulators oftentimes rely on structures, which have to be etched out of the grown films. To measure the transport properties of the samples grown in this work for example, Hall bar structures are etched into the TIs in order to characterize them. This etching, be it wet or dry chemical etching, can cause severe damage to the films, especially the topmost layers, rendering them unsuited for measurements of the surface state transport. These findings will be shown in detail in chapter 6 and 7. Therefore, it would be favorable to grow the structures in the MBE directly, avoiding the necessity of post-growth structuring. Kampmeier *et al.* showed, that this so called selective growth is realizable by using silicon on insulator (SOI) substrates [33]. Their SOI substrates consist of three layers, a 70 nm thick layer of Si (111) (the device) on top of a silicon oxide (buried oxide, BOX) layer with 300 nm thickness and lastly the Si (001) substrate underneath (handle).

The fabrication of suitable prepatterned structures is performed by first coating the Si (111) with resist and then writing the layout into it by either optical or electron beam lithography. Development later reveals the desired structure, covered with resist. With reactive ion etching, silicon not protected by the resist is etched away, leaving only a Si (111) mesa in the chosen form. Due to the aforementioned similar hexagonal crystal structures of the TIs and the Si (111) surface, the TI grows preferably on these areas. Moreover, Kampmeier *et al.* state in their work, that easy re-evaporation from the silicon oxide further suppresses nucleation on the oxide surface [33]. The TIs will hence only grow on the Si (111) mesa, enabling growth restrained to predefined patterns. But due to the free standing of the film on the plateau, the sides of the topological insulators are exposed to ambient conditions [35]. Moreover, this method is not suitable to grow sub micrometer structures, since the topological insulator thin films proceed to grow larger than the designed mesa, causing the structures to overlap in array-like designs. Therefore, another approach was taken to grow sub-µm structures, which is the growth in trenches etched into silicon nitride (Si_3N_4). As stated in his thesis, Heider managed to grow test samples with Bi_2Te_3 in trenches, which were etched into 110 nm thick Si_3N_4 to reveal the underlying Si (111) surface. However, this could only be performed successfully once and was irreproducible [35]. This was the starting point for the present study on growing low dimensional topological insulator structures.

For the substrates, phosphorous doped Si (111, n-type, >2000 Ω·cm) wafers are coated with 5 nm of SiO_2 and 20 nm of Si_3N_4 in a low pressure chemical vapor deposition chamber. As the goal for these substrates is the growth of quasi one-dimensional structures with variable length, but confined to nanometer scale widths and heights, the nitride and oxide layers can be chosen reasonably thin. The oxide layer as an intermediate buffer between the silicon surface and the nitride is used as an etch stop when etching the structures into the silicon nitride with reactive ion etching. Moreover, the oxide is used to protect the silicon, so that a pristine surface is revealed when the oxide is removed before growth. However, the most important feature of the silicon oxide interlayer is the relaxation of the silicon/nitride interface [36, 37]. In his thesis, Heider states that the only working sample broke before TI deposition [35]. Thereby, possible strain of the sample surface had presumably been removed, allowing for TI growth. By applying an oxide interlayer, potential stress at the silicon/nitride interface is prevented.

To structure the sample, the substrate is first coated with AR-P 6200 (CSAR 62), diluted 1:1 with AR 600-02 by ALLRESIST GmbH, which is a positive resist compatible with electron beam writing. After baking the resist, the sample is irradiated with electrons during an electron beam lithography process. The irradiated resist is then developed and thereby removed. Lastly, the sample is inserted into a reactive ion etching chamber and via chemical dry etching with CHF_3 and O_2 gas the exposed silicon nitride is removed, leaving the oxide intact. An example for a structured nitride surface is shown in the scanning electron microscope (SEM) image in Fig. 4.1. A more detailed description of the fabrication process is given in the master thesis of Tobias Schmitt, where the creation process and measurements of the finished prestructured samples is explained [38].

After lifting the excess resist, the samples need to be cleaned for the TI growth. As for pure silicon substrates, a two-step cleaning process with Piranha solution and subsequent hydrofluoric acid dip is performed. The Piranha solution dissolves any organic contaminations present on the sample and oxides the silicon surface, so that the following HF dip can remove the oxide to reveal a pristine Si (111) surface.

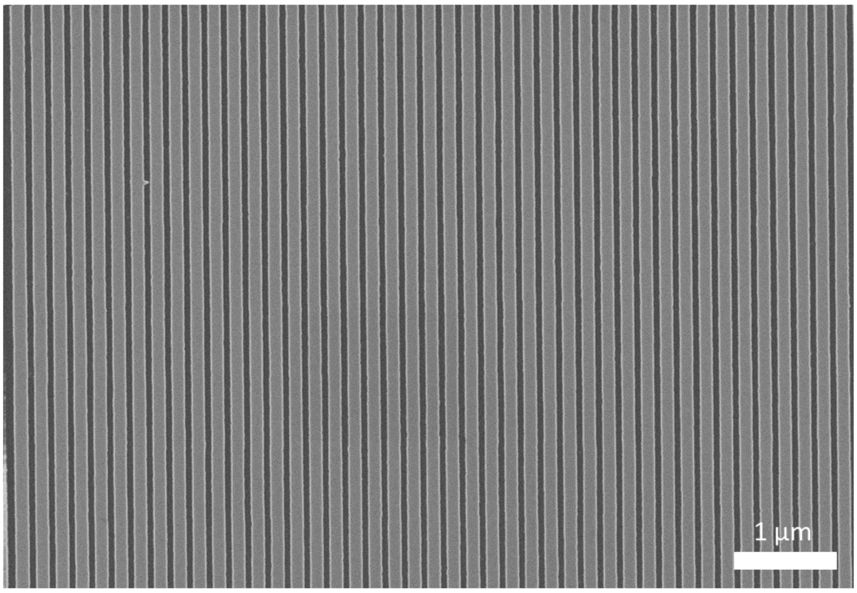

Fig. 4.1: *50 nm wide trenches defined in the Si_3N_4. The brighter surface is the structured nitride, while the dark surface denotes the Si (111) to be grown on, covered by a thin layer of silicon oxide.*

The name Piranha solution loosely refers to a mixture of sulfuric acid and hydrogen peroxide. In this work, if piranha solution is mentioned, the solution consists of two parts 96 % sulfuric acid combined with one part 36 % hydrogen peroxide solution. Given that the substrates are already covered with silicon oxide, as it acts as the etch stop for the silicon nitride etch, the oxidising effect of the piranha solution affects only contaminations on the sample. The samples are put into the mixture for 10 minutes, then rinsed and transferred into 1 % HF. There, the aforementioned oxide is removed. For simple silicon, this HF dip is done for five minutes, however this would cause a large-scale underetching. This means, that the silicon oxide underneath the silicon nitride is removed due to the isotropic etching with HF, which can cause the now freestanding silicon nitride to cave in. To prevent this, the etching needs to be timed in way, that only the oxide in the designed structure is prevented. By measuring the etch rate of the oxide, the necessary etch time is determined to be 135 seconds. This additionally includes the time to passivate the revealed silicon surface with hydrogen atoms, which are then removed by heating in the MBE to create a pristine surface with dangling bonds [39]. The latter are unsatisfied valence electrons of an atom on the surface of a solid, in this case the silicon crystal. Therefore, the samples are heated to 700 °C and then cooled to the desired growth temperature.

As the first material to be grown into the prestructured samples for tests Bi_2Te_3 is chosen, since for this material Heider already showed that selective growth is possible. The substrate temperature is set to 300 °C, with T_{Te} = 330 °C and T_{Bi} = 470 °C. As soon as the sample is cooled down to the set temperature, after 10 minutes of annealing at 700 °C for

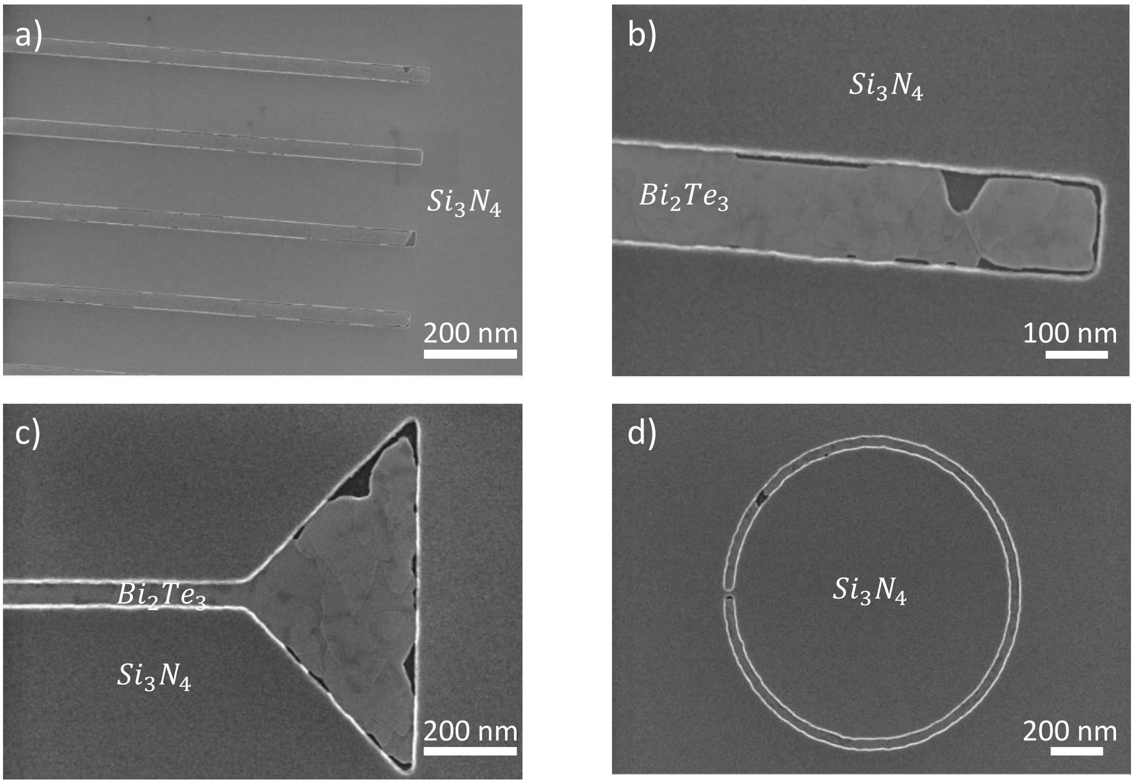

Fig. 4.2: *First growth attempt of Bi_2Te_3 on prestructured samples. a) The SEM picture shows grown film in a line array with a linewidth of 100 µm. With higher magnification, as in b), the layered structure of the film can be identified. c) Growth in the trenches with enlarged ends shows no clear improvement of quality, but the figure shows that continuous growth was also achieved in the smallest, 50 nm wide, structures. This also includes the growth in curved structures as in d). In the micrograph, two roughly 50 nm wide gaps in the film can be seen.*

hydrogen passivation removal, and the sources are at a stable temperature, the tellurium shutter is opened for 30 seconds. This saturates the dangling bonds mentioned before with a layer of tellurium, on which the topological insulator growth can commence as soon as the bismuth shutter is opened.

The results of the first growth attempt are shown in Fig. 4.2, where in a) an array of 100 nm and 20 µm long trenches is depicted. In the trenches, a smooth layer of Bi_2Te_3 is visible, comparable with the successful growth shown in T. Heider's master thesis [35]. Therefore, the assumption of using a silicon oxide interlayer for stress relaxation can be confirmed as necessary for the growth of TI on silicon within silicon nitride patterns. On the silicon nitride, next to the trenches, no crystallites are present, affirming that possible nuclei are reevaporated or suppressed entirely. The structure of the grown film can more clearly be seen in Fig. 4.2 b), where single steps in the Bi_2Te_3 are identifiable. The hole in

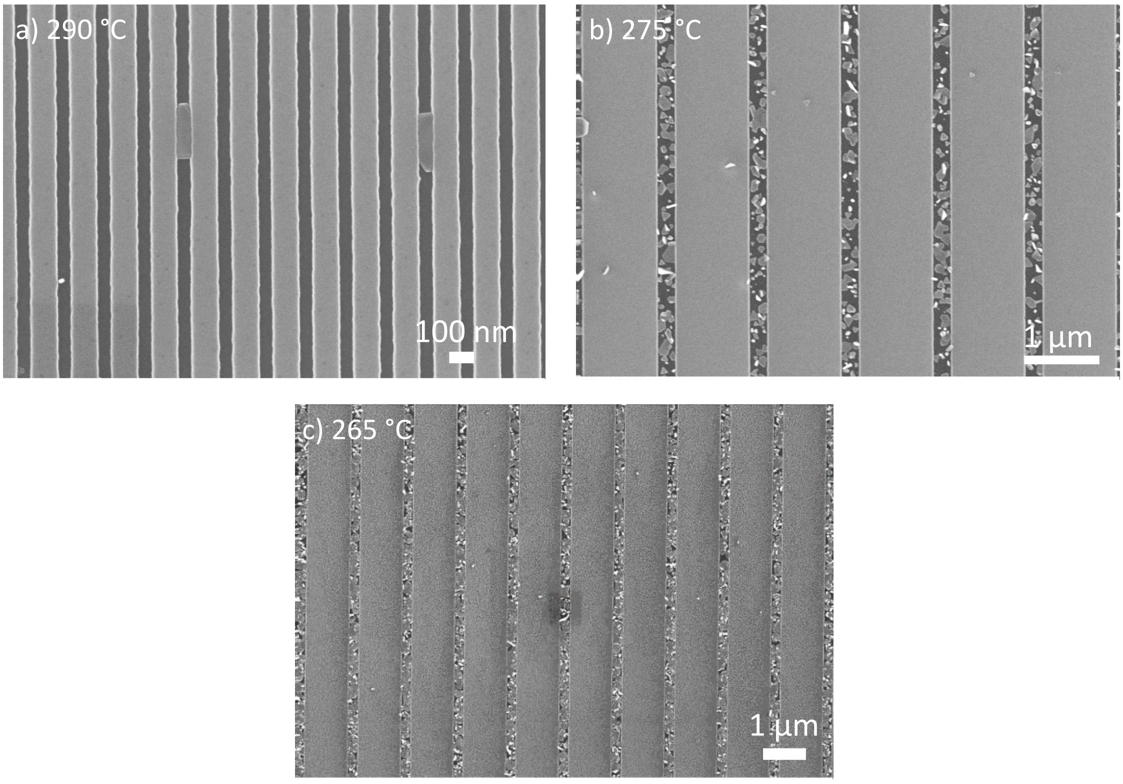

Fig. 4.3: *Predefined trenches of different widths for growth attempts of* Sb_2Te_3 *at varying substrate temperatures taken with a SEM. Micrograph a) shows the growth at 290 °C, with only little nuclei formation. In figure b) at 275 °C, a large number of single crystallites is found in the trenches, which increases further going to 265 °C substrate temperature.*

the film suggests the conclusion, that at the end of the trench and some 100 nm next to it, two nuclei formed that later grew together. Fig. 4.2 c) shows a different layout, which is designed so that the TI growth has a larger area for the initiation of the formation of a closed film. With this initial aid, the film can grow into the trench and supposedly form a continuous nanoribbon. This option of growing the ribbons was originally planned for the case that the growth in the conventional trenches was not working. However, as this is not the case, the growth in the broadening trenches presumably occurs at any point in the trench, as in the conventional trenches. Moreover, even though the width of the trench is only 50 nm, no change in film quality is visible compared to Fig. 4.2 a) and b). Lastly, Fig. 4.2 d) shows that even non-angular, but round structures can be filled with Bi_2Te_3 films of the same quality. In the film, two gaps are visible, one at the left of the structure and one slightly above. The latter is a disruption in the film as in Fig. 4.2 b), while the left is put there intentionally with nitride. This TI ring with a roughly 50 nm wide interruption could be used as a superconducting quantum interference device (SQUID), which will not be explicated further in this thesis. The design of the pre-patterned nanostructures is devised and explained by Tobias Schmitt in his master’s thesis, who also shows measurements of contacted nanostructures grown as shown in this chapter [38].

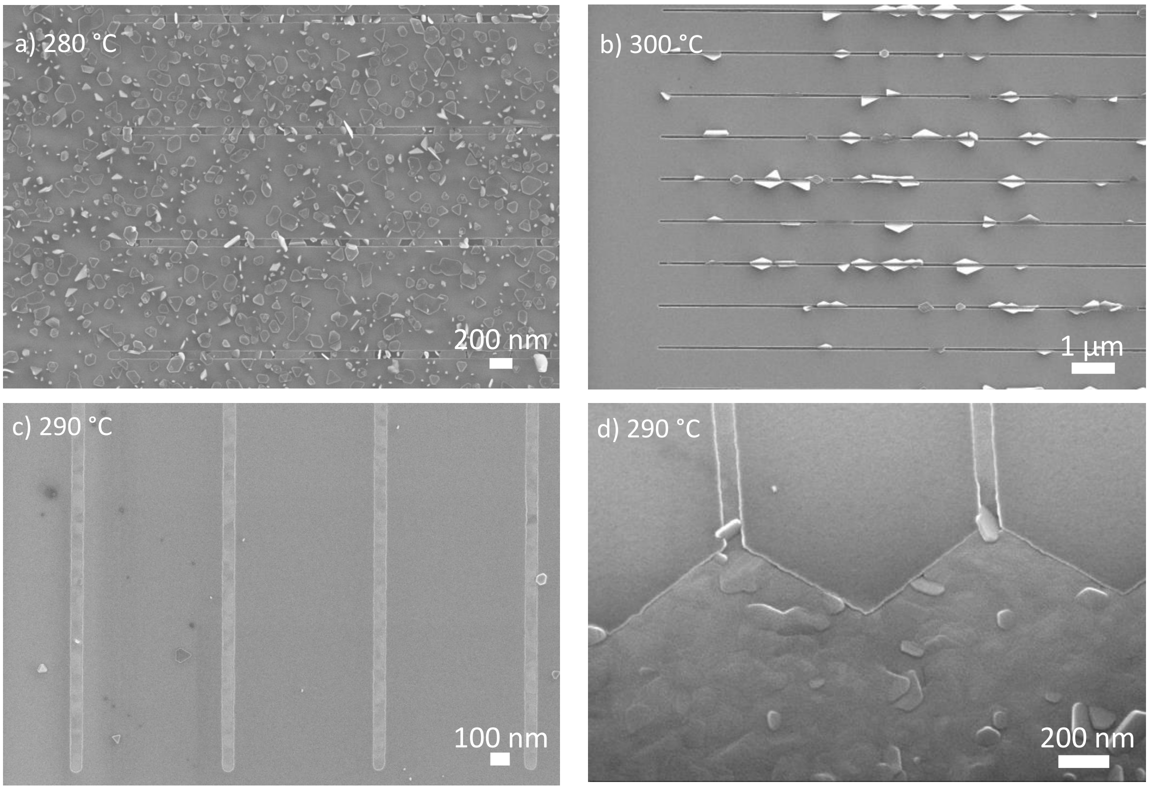

Fig. 4.4: *SEM micrographs of prestructured trenches filled with a TI stack consisting of 2 nm of* Bi_2Te_3 *and* $Bi_{2-x}Sb_xTe_3$ *on top. In a) crystallites can be found not only in the trenches, but also on the nitride, indicating a too low substrate temperature. The opposite is the case in b), where only few crystallites formed due to a substrate temperature that is too high. At 290 °C in c) and d), the growth parameters are optimal, providing smooth and continuous growth, even in the smallest structures.*

Since the fabrication of Bi_2Te_3 films in the predefined patterns as shown before could be done repeatedly, granting reproducibility, the next step is to grow Sb_2Te_3 as a precursor to the growth of the ternary compound $Bi_xSb_{2-x}Te_3$ with $x = 0.06$. The compound ratios of this TI are chosen in a way that the Dirac point and the Fermi energy in thin films are only 2 meV apart [40]. As this compound is structurally more akin to Sb_2Te_3 than to Bi_2Te_3 due to the high Sb portion, successful growth of Sb_2Te_3 in the nanostructures would also suggest effectual ternary growth. Therefore, Sb_2Te_3 is the next compound to be grown in the trenches. Some of the attempts to grow Sb_2Te_3 are shown in Fig. 4.3. The substrates were fabricated and cleaned in the same way as those for the Bi_2Te_3 growths, but as shown in Fig. 4.3 a), no continuous film is grown at 290 °C. Instead, only sporadic nucleation sites can be found. This usually indicates that the growth temperature is too high, causing the topological insulator to re-evaporate. Hence, growth attempts are performed at lower substrate temperatures. But as can be seen in Fig. 4.3 b) and c) at 275 °C and 265 °C respectively, albeit the number of nuclei is increased with decreasing temperature, no closed film is grown.

To avoid this problem of nucleation without formation of a closed film, a possibility is to grow a layered structure. As was shown by Martin Lanius *et al.*, it is possible to effectively grow Sb_2Te_3 films on top of Bi_2Te_3 [41]. Therefore, in the next attempts, before growing the antimony telluride, for 4 minutes a thin layer of Bi_2Te_3 is deposited into the trenches with a thickness of approximately 2 nm. The thickness of the Bi_2Te_3, and also of films on top, is estimated by the growth rate, since for XRR the areas covered with TI are too small, providing a signal that is not sufficient for the measurements.

The thin pseudo substrate drastically improves the growth quality, enabling the first tries to grow the ternary compound with the same procedure. For the ternary compound, the sources are set to T_{Te} = 330 °C, T_{Bi} = 450 °C and T_{Sb} = 450 °C. The results of the growth experiments of the ternary TI are shown in Fig. 4.4 a) – d). In a) the topological insulator stack was grown at a substrate temperature of 280 °C. It is clearly visible that the nucleation occurs everywhere on the sample, not only in the predefined structures. This is due to the suppression of reevaporation at low substrate temperatures. At even lower substrate temperatures, for example 270 °C, the silicon nitride is becoming gradually covered with topological insulator until it is fully covered. The exact opposite is the case for a substrate temperature of 300 °C. As shown in Fig. 4.4 b), a too high substrate temperature results in the formation of multiple crystallites instead of a closed film, comparable to the results of the Sb_2Te_3 growths. At 290 °C the substrate temperature is optimal, with little to no crystallites on the nitride and a closed film in trenches of all sizes as shown in Fig. 4.4 c). Viewing the film from a 60° angle like in Fig. 4.4 d) shows how the TI growths closely underneath the edge of the nitride. Moreover, some crystal flakes can be seen which protrude from the film, but dominantly in the larger areas of the broadening layout.

For further investigation of the grown ribbons with transport measurements, a thin layer of roughly 2-3 nm aluminum is deposited after the growth of the TI, which will oxidize and form a capping layer of AlOx. The latter is visible as a transparent layer on top of the substrate that appears grainy, as shown in Fig. 4.5 a) and b), but is continuously closed. The importance of this capping layer will be discussed in further detail in chapter 6. Moreover, to test the endpoint of the growth, a deposition of the ternary compound is performed for twice the time needed to fill the trenches. The growth shows similarities to the growth at too low temperatures, as in Fig. 4.4 a), however T_{sub} is the same as in Fig. 4.4 c). The grains adjacent to the trench probably form due to the prolonged supply with evaporated material, so that especially stable nuclei on the silicon nitride do not disperse, but grow. Meanwhile, the trenches fill up and the TI grows also on top of the nitride, widening to roughly 200 nm in width from the intended 50 nm. However, the overall structure is maintained and no connection between the separate trenches occurs. The form of the overgrowth closely resembles the free-standing structures in T. Heider's thesis [35].

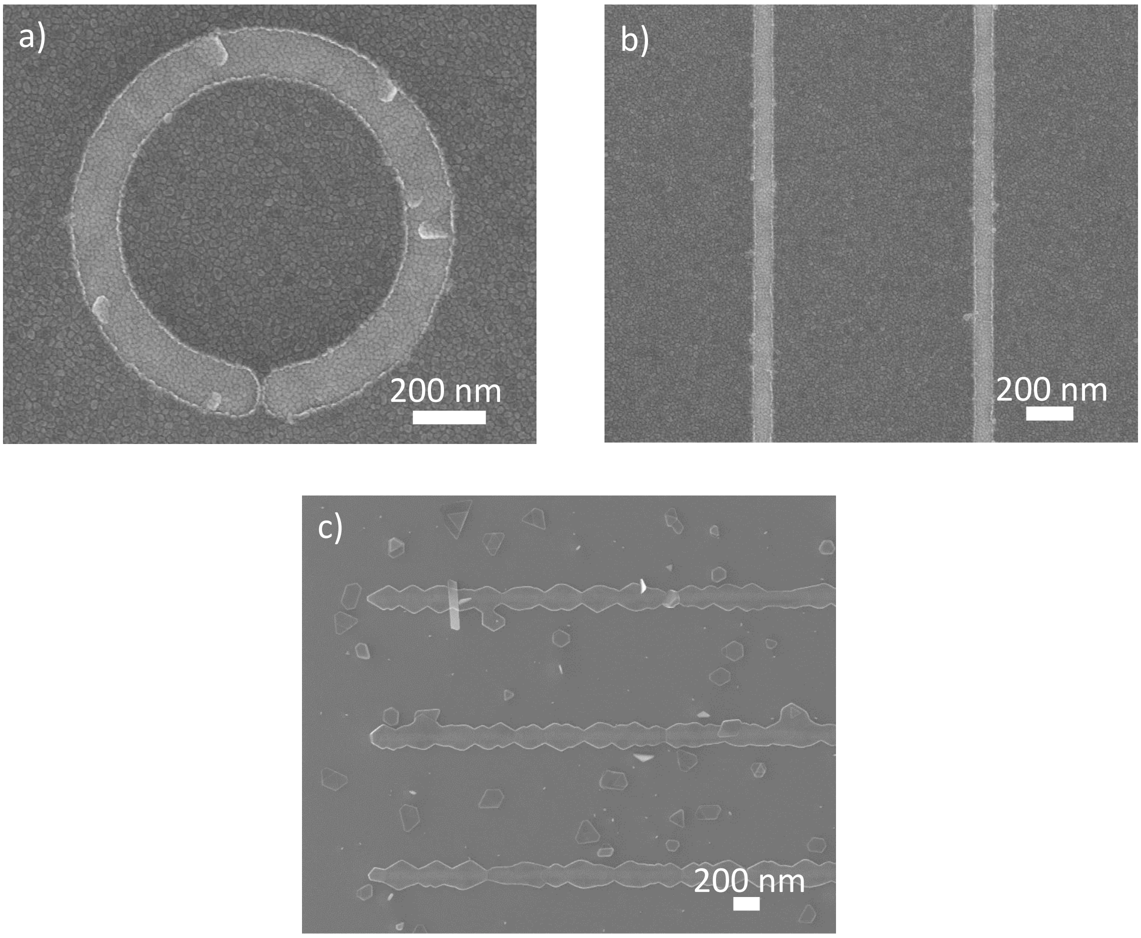

Fig. 4.5: *a) and b) show SEM micrographs of 100 nm wide prestructures filled with ternary film and covered with* AlO_x *capping, by first growing the TI film and then depositing 2-3 nm of Al, which oxidizes in ambient conditions. c) Image of a sample on which a long-time growth was performed, resulting in an overgrowth of the 25 nm deep trenches with TI.*

The work presented in this section shows that it is possible to reproducibly create nanometer sized topological insulator ribbons down to sizes of 50 nm in breadth. This is achieved by using a silicon oxide interlayer, relieving the stress that might arise due to a direct interface of silicon and silicon nitride, preventing growth. With an initial Bi_2Te_3 deposition step, even ternary compounds containing a large amount of antimony can be grown in the layouts. This enables the fabrication of lateral TI structures with complex features. Moreover, the TI in the trenches is protected from influences from the environment on its side as well as its bottom surface. The top surface can additionally be protected by a capping, resulting in an entirely protected surface of the topological insulator. But the formation of twin domains and other crystallographic defects still impairs the TIs negatively. In this section, it has however been shown that growing thin Bi_2Te_3 as a pseudo substrate for the ternary helps the latter to grow in the structures. This poses the question, whether it is possible to decrease the crystallographic effects, or even

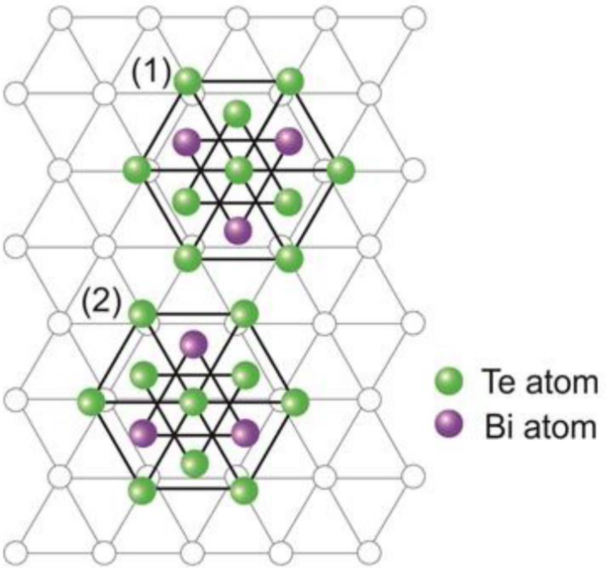

Fig. 4.6: *Bi_2Te_3 tetradymite structure grown on a (111) surface, e.g. silicon. Due to the van-der-Waals growth, the lattice mismatch only concerns the lowest layers. But, as shown in the figure, the substrate allows for two configurations. The growths are distinguished by a 60° rotation of the domains, in which the domain collinear to the Si (311) reflection is energetically more favorable. Adopted from [28].*

avoid them completely by choosing the right (pseudo) substrate in combination with the silicon nitride prestructures. This approach will be elaborated in the next section.

4.2 Improving Film Quality by Substrate Choice

The TIs investigated in this work all have a tetradymite crystal structure [2, 16]. Therefore, substrate surfaces in the (111) direction are favorable for growth as shown in Fig. 4.6. Due to the van-der-Waals growth of the TIs, which was explained in the theory section, even lattice mismatches of 14 % as between Si and Bi_2Te_3 can be compensated [42]. However, as shown in Fig. 4.6, the structurally fitting substrate still allows crystallographic defect due to domain formation. The figure shows two domains rotated by 60°, which, when they coalesce, will result in the formation of a grain boundary. As explained by Kampmeier *et al.*, this formation of so called rotated boundaries can be suppressed in Bi_2Te_3 by growing sufficiently slow, since the domain collinear to the Si (311) is energetically more favorable and will prevail given enough time and energy for the atoms to rearrange [33].

But there exists another approach to reduce the formation of twin domains and other possible defects, which, with respect to the findings of section 4.1, would allow for promising pseudo substrates. Multiple groups have shown that Bi_2Se_3 can successfully be grown on indium phosphide (InP) substrates, which has a lattice mismatch of 0.2 % to

Bi_2Se_3, with suppression of twin domains [32, 43–46]. In the course of their research, Tarakina *et al.* discovered that MBE growth of Bi_2Se_3 on InP depends largely on the roughness of the substrate surface [47]. To prepare the samples for growth, the samples were annealed to 300 °C, 570 °C, 620 °C and 730 °C. This removes the surface oxide to reveal the crystalline (111) surface of the substrate. Substrates that are not annealed higher than 300 °C are additionally dipped into 50% hydrofluoric acid (HF) beforehand to ensure oxide removal. During the annealing, a constant selenium flux is provided to suppress phosphor diffusion from the substrate. Tarakina *et al.* then showed that the ratio between the two rotated domains in Bi_2Se_3 changed gradually with the annealing temperature. At high annealing temperatures (700 °C, 620 °C) the two domains coexist, while at low annealing temperatures (570 °C, 300 °C) the formation of one domain is heavily suppressed [47]. They explained this effect by a change in surface roughness during annealing, which was later confirmed by Xie *et al.* [48]. In highly annealed samples, the surface is flattened, causing island growth with the formation of rotated domains. On rougher samples however, the hollow trenches are filled first and subsequent step flow growth suppresses rotated domain formation [16].

As stated in the introduction to this chapter, having a pristine surface to grow topological insulators on is essential for the film quality. As all TIs grown in this work have a similar crystal structure, it is possible to stack them on top of each other by changing the evaporated elements during growth in the MBE. This factor was already utilized in section 4.1. Bi_2Se_3 that was grown on InP as explained before qualifies as an excellent pseudo substrate for the tetradymite TIs grown in this work, since it can be grown very flatly and the formation of twin domains is suppressed. This suppression may then continue in the second film, leaving only antiphase defects due to steps in the substrate or pseudo substrate as possible causes for defects in the topological insulator film [47]. Moreover, doping the InP substrate with iron creates a substrate with a high electrical resistivity, $\geq 5 \cdot 10^6\ \Omega \cdot \mathrm{cm}$ (the usually used Si (111) substrates have a resistivity of $\geq 2 \cdot 10^3\ \Omega \cdot \mathrm{cm}$ [49]), which is decisive for transport measurements on the samples.

Thus, to fabricate such heterostructures, Bi_2Se_3 growths on InP are performed in the molecular beam epitaxy chamber. The InP substrates are first cleaned in the cleanroom facilities of the Helmholtz Nano Facility (HNF) with a dip into 1 % HF for 10 minutes to remove the oxide. Kept in a nitrogen atmosphere, the sample is brought to the MBE as fast as possible to prevent reoxidation. In the growth chamber, the sample is heated to 300 °C as in [47] to maintain the rough surface essential for the growth. At 140 °C substrate temperature the selenium source is opened to create a Se partial pressure so that phosphor is prevented from diffusing out of the substrate [16].

Now the correct growth parameters need to be found to grow smooth and closed Bi_2Se_3 films with suppressed twin formation. These parameters are the source temperatures and

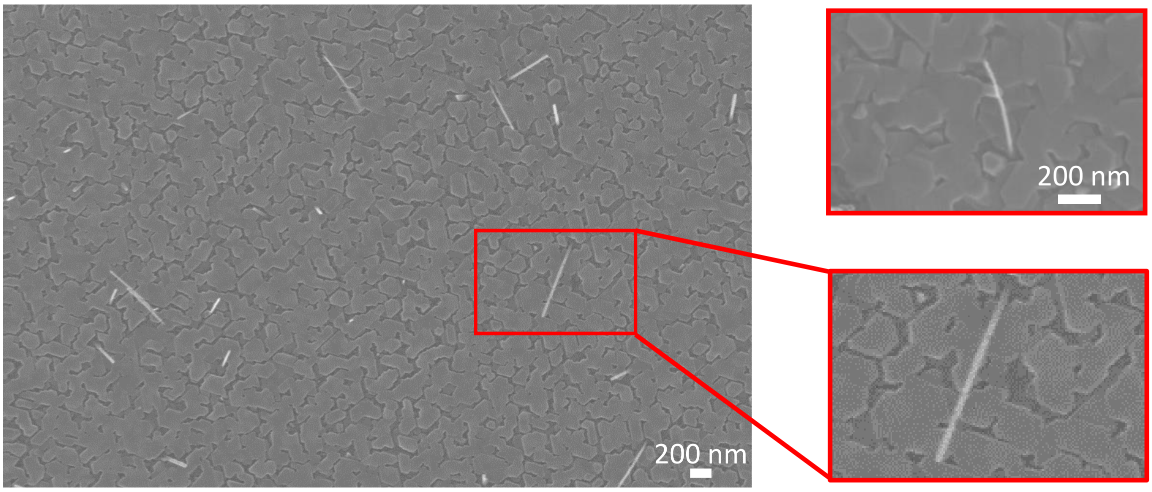

Fig. 4.7: *SEM pictures of Bi_2Se_3 grown on InP:Fe (111). The figure shows a crystalline, but neither smooth nor closed film. The original triangular shape of the crystal can still be identified, however not very sharply. Moreover, fine nanowires that grow out of the cracks in the film can be found, which vary in thickness, length and direction. The wire shown in the inset has a diameter of approximately 12 nm.*

most importantly the substrate temperature during growth after annealing. Since the growths are performed with selenium overpressure, the rate is regulated solely by the supplied bismuth flux. The first growth at 300 °C substrate temperature resulted in a rough film, as can be seen in Fig. 4.7. The characteristic triangular shape of the Bi_2Se_3 film is recognizable in the insets with higher magnification, but the film does not grow closed and the triangles are not sharply defined. Instead, it seems that first islands grow on the substrate, which then partly interconnect, forming a network of islands with holes in between. Moreover, nanowires emerging from the holes can be observed, which differ in size, direction and length. To smoothen the surface and remove the nanowires, an annealing step is introduced to the process after growth. While the selenium flux is maintained to suppress outdiffusion of Se from the Bi_2Se_3 film, the sample is heated to 300 °C and kept at that temperature for 10 minutes. The results are shown in Fig. 4.8 in the left figure. The connected areas are larger and the edges much sharper, consistent with the sharp triangular shape of Bi_2Se_3 crystals. In the SEM figures, multiple levels of film height can be identified, which is more evidently seen in the atomic force microscopy (AFM) micrograph on the right in Fig. 4.8. There, the height differences between holes and incontinuous film can be measured to be up to roughly 7 nm.

An entirely different film quality can be found on the same sample in areas where scratchmarks, caused with tweezers during cleaning, are located. As shown in Fig. 4.9 a), several micrometer large areas can be found, in which the surface was supposedly roughened by scratching. Comparing the growth inside these areas and the growth on the less roughened areas, it is evident that the rough surface brings forth a

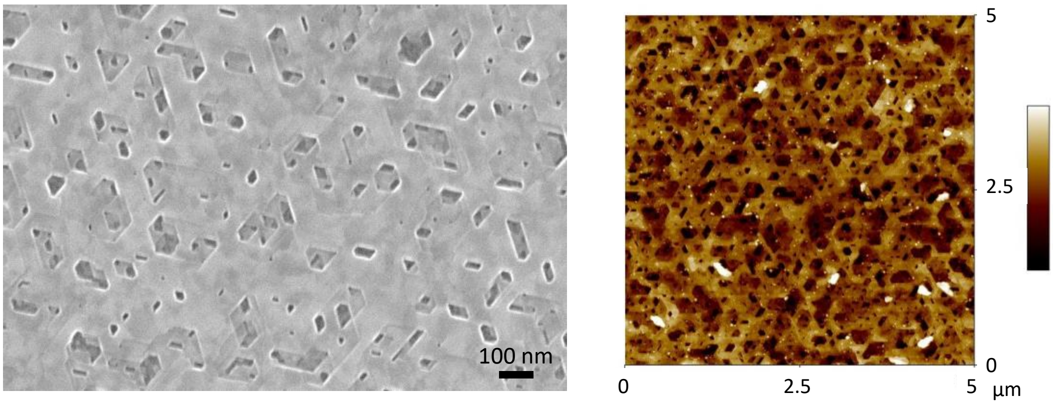

Fig. 4.8: *SEM image of Bi_2Se_3 grown on InP:Fe with the same growth parameters as in Fig. 4.7, but with an additional annealing step after growth, in this case 20 min at 330 °C. On the right, an atomic force microscope picture of the Bi_2Se_3 film surface is shown. The colorbar is fixed to the highest measured value.*

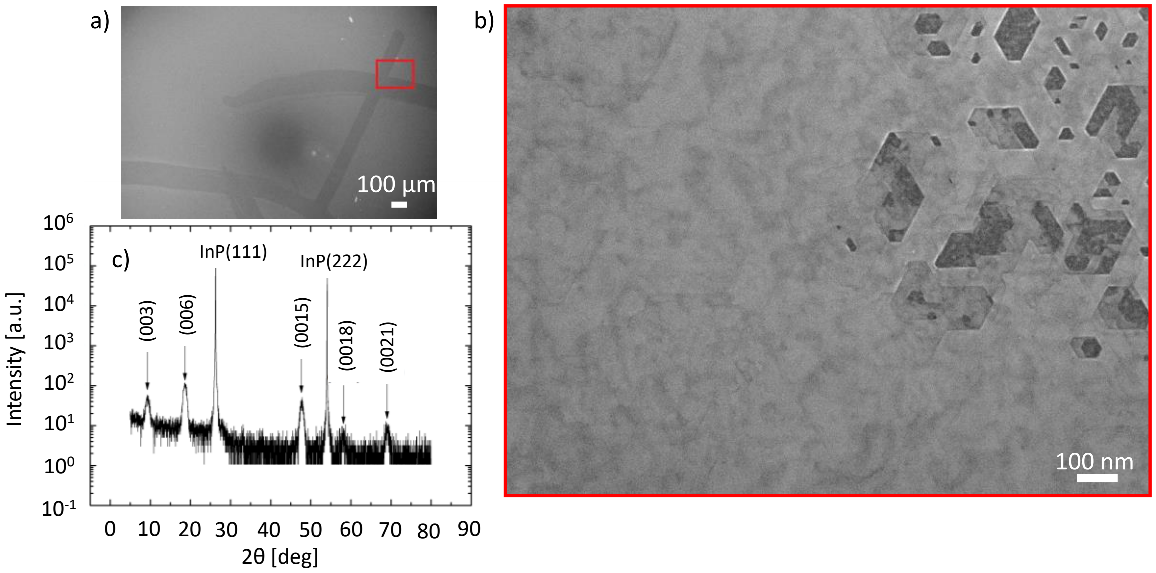

Fig. 4.9: *a) and b) SEM pictures of the growth differences between regions of changing substrate roughness. The large picture shows the highlighted region of the inset. In the large streaks on the sample, probably scratches caused with tweezers during the cleaning process, the film grows without holes. Instead, the film is smooth and of equal height as the highest islands in the discontinuous film. c) 2θ XRD scan of the film with the characteristic Bi_2Se_3 and InP peaks identified.*

much smoother surface, devoid of any holes. The height of the closed film appears to be equal to the highest level of the discontinuous layer. As shown in [44, 47], rough substrates facilitate a smoother growth, which is confirmed by the differences in film quality revealed in Fig. 4.9 b). XRD measurements of the sample show the characteristic peaks of Bi_2Se_3, shown in Fig. 4.9 c).

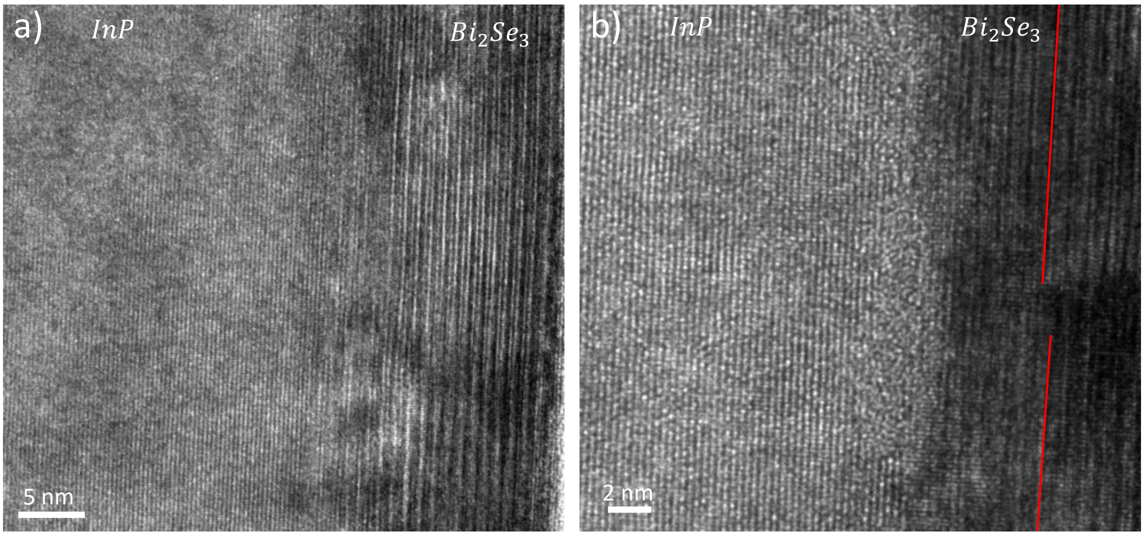

Fig. 4.10: *TEM micrographs of Bi_2Se_3 (right-hand side) grown on top of InP. The simply ordered structure of the InP is contrasted by the more complex layered structure of the TI. In between, amorphous regions are visible, which form during the preparation of the lamella with gallium ion strafing.*

Thus, to sustain a rougher substrate, the samples are cleaned in 10 % HF for 20 minutes to not only remove contaminations, but also to abrade the surface. The InP substrate is subsequently heated to 300 °C as before, but only for 5 min, to keep the surface from flattening during oxide removal. To investigate the substrate surface roughness and the growth of the TI on top, transmission electron microscopy (TEM) is done. TEM is a variant of microscopy, in which a lamella of a sample with a thickness of less than 100 nm is rayed by a focused electron beam. The electron beam scans the sample, but is not reflected as in a scanning electron microscope, but transmitted through the thin sample. The results of the growth are shown in the TEM micrographs in Fig. 4.10 a) and b). Two different crystal structures can clearly be distinguished. On the left-hand side of Fig. 4.10 a) and b) a neatly ordered, brighter material is visible, which is the InP substrate. On the right-hand side, the darker TI film is shown. In comparison to the simple structured InP crystal, with separate but equally sized and spaced lines of atoms, best visible in Fig. 4.10 b), the TI film shows a layered structure with stacks of roughly 1 nm in width, matching the lattice constant of Bi_2Se_3 [44]. In between the stacks, dark areas exist, which in the bright field micrograph correspond to areas without atoms. These areas are the van-der-Waals gaps, present in all tetradymite TIs.

At the interface of the two layers, an amorphous region can be found, best visible in Fig. 4.10 b). The amorphous regions form during the thinning of the lamella with ion milling and are not present in the original sample. Although some parts of the interface are amorphous, the transition from substrate to film is clearly identifiable. In both figures, Fig. 4.10 a) and b), the surface is not flat but rough on a nm scale, as anticipated.

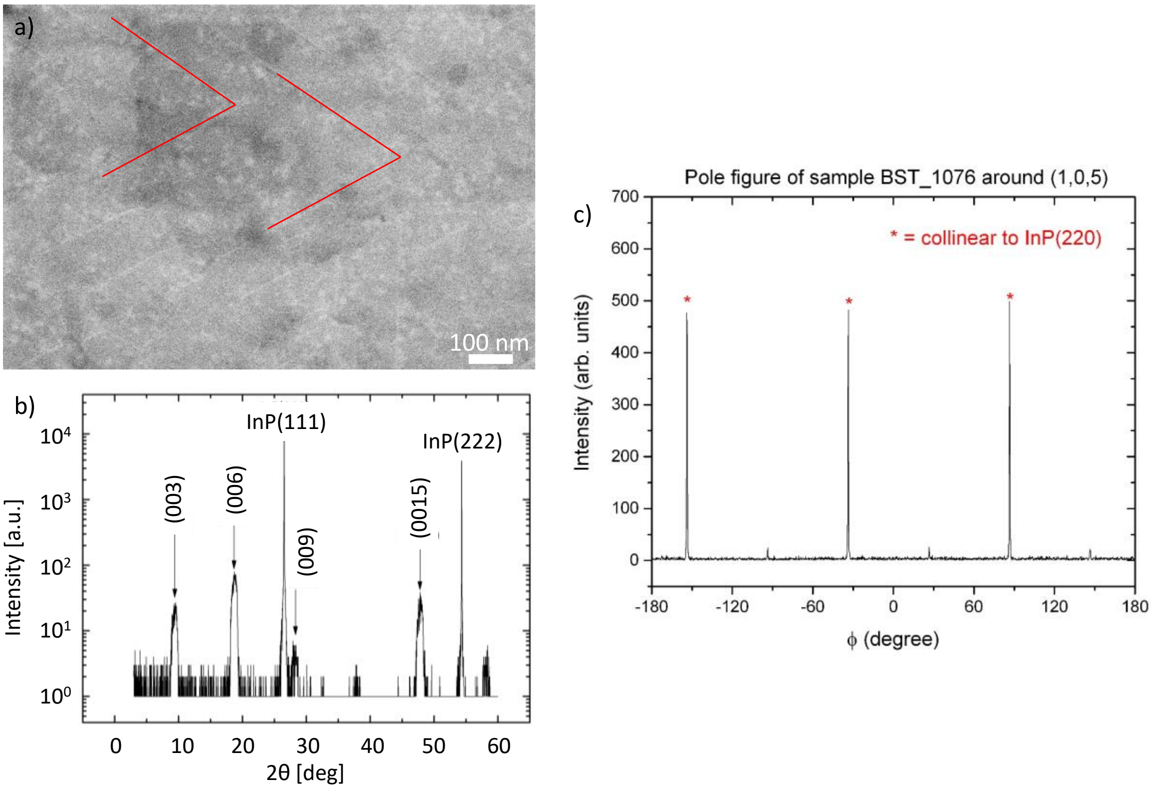

Fig. 4.11: *a) The SEM micrograph shows the surface of the* Bi_2Se_3 *grown on a rough InP substrate. Parallel terraces are faintly visible, red lines are added as a guide to the eye. Graph b) shows the XRD scan of the sample, with the peaks of* Bi_2Se_3 *and InP labelled. Figure c) shows the result of the XRD in-plane rotational phi scan. XRD Measurements performed by Gregor Mussler.*

On top of the rough surface however, the TI immediately forms its neatly ordered structure. In Fig. 4.10 b), red lines show the course of one of the van-der-Waals gaps in the TI. The gap is not continuous, but disrupted. This is an indication for a crystallographic defect that cannot be resolved with the choice of substrate, an antiphase defect. These defects occur at steps in the substrate. When the films on each steps coalesce, their unit cells are shifted by the step height in the substrate, forming two domains that are separated locally [47]. The SEM micrograph in Fig. 4.11 shows that the film is closed as in the scratched areas of the sample in Fig. 4.9, with parallel terraces tapering to the tip of a triangle, highlighted by the added red lines. In Fig. 4.11 b) the XRD peaks of Bi_2Se_3 are clearly distinguishable.

To verify, whether the grown film of Fig. 4.11 is domain free, an x-ray diffraction in-plane rotational phi scan is done. Therefore, the XRD signal on the (105) peak is measured and the sample rotated during the measurement. A large signal is detected when the x-ray detects the peak again, resulting in a peak every 120° in the tetradymite crystal structure. If two by 60° rotated domains existed, two sets of three peaks would be present. In Fig. 4.11 c), three dominant peaks with 120° distance can be identified, which are

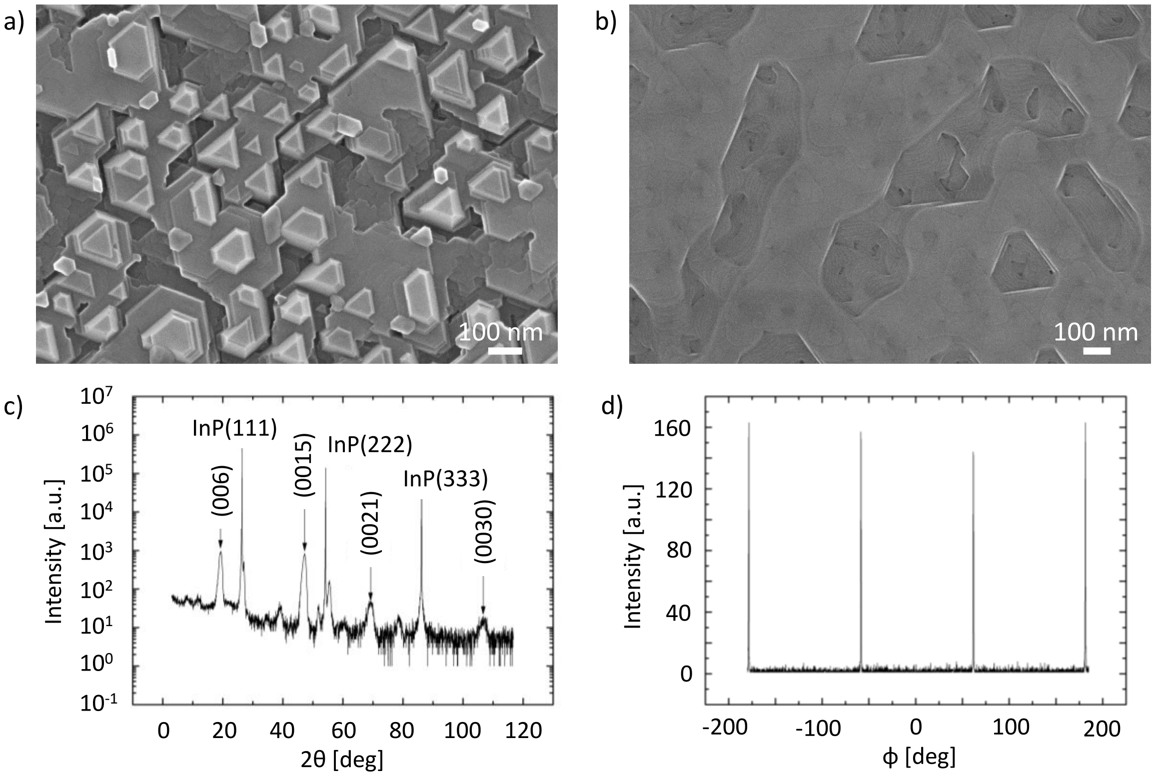

Fig. 4.12: *The SEM micrographs a) and b) show the surface of the quaternary system grown on the InP/Bi_2Se_3 substrate with the first or second process, respectively. Triangular valleys of different sizes with multiple terraces are visible on both, however a) displays a sharp island growth. Figure c) shows the XRD peaks of the film in b), with the InP substrate peaks marked. In d), the phi scan of the sample in b) is shown, exhibiting four peaks. However, the peaks at -180° and 180° equivalent. XRD measurements performed by Gregor Mussler.*

collinear to the (220) peaks of the InP substrate. Between them, located on the 60° shifted position of the peaks of the rotated domain, smaller peaks are visible, originating from the rotated domain. The difference in peak height can be directly related to the ratio of rotated domains, suggesting that the grown film is nearly domain free [47]. As has been shown in the previous paragraphs, Bi_2Se_3 was successfully grown on rough InP with almost complete suppression of rotated domains. The next step is to use the Bi_2Se_3 as a pseudo substrate. Therefore, a quaternary system is grown after depositing 10 nm of Bi_2Se_3. The quaternary system itself is further discussed in chapter 5, here, only the growth on the pseudo substrate will be discussed. After depositing the Bi_2Se_3 with $T_{sub} = 280$ °C, $T_{Se} = 110$ °C and $T_{Bi} = 560$ °C, two different process are executed to grow the quaternary on top. For the first, the Bi shutter is closed and the effusion temperatures set to $T_{Se} = 93$ °C and $T_{Bi} = 470$ °C, while the temperatures of Te and Sb are set to $T_{Te} = 330$ °C and $T_{Sb} = 417$ °C with closed shutters. Thus, the quaternary temperatures are set while still supplying Se. When the temperatures are stable, the Bi, Sb and Te shutters are opened. The result of this growth is depicted in Fig. 4.12 a). In the second process, after growing the Bi_2Se_3, the effusion cells are opened simultaneously before setting the temperatures to the previously stated quaternary values. Thereby, the stoichiometry of the grown TI changes gradually, in contrast to the first process, where it changes abruptly. The result of the second process is shown in Fig. 4.12 b).

Comparing the SEM micrographs, the difference between the two processes is clearly visible. The abrupt first process in a) leads to a pronounced island growth, showing many bright triangular islands growing on top of a discontinuous Bi_2Se_3 film. The second process on the other hand results in a smooth continuous film, although holes or valleys can still be recognized in b). Therefore, the gradual change in film stoichiometry, due to the successive change in lattice constant, results in a better adaption of the quaternary to the underlying binary system. The valleys indicate that the growth parameters can still be optimized, however they foreground an interesting feature of the film. In Fig. 4.12 b) the triangular valleys almost exclusively point in the same direction, similar to the triangular pyramids in Fig. 4.12 a). This suggests that the formation of rotated domains is also suppressed in the quaternary top layer. If both domains existed, there would also be irregular or diamond shaped valleys/islands as in Fig. 4.8 a). Hence, XRD measurements are performed to confirm the assumption on the sample fabricated by the second process. In Fig. 4.12 c) the 2θ scan is shown. The peaks of the tetradymite crystal can be identified up to high orders, indicating that a good crystal structure is existent. The phi scan in Fig. 4.12 d) verifies the existence of only a single domain. The outermost peaks are located at -180° and 180° and therefore belong to the same signal. Thus, the three peaks are located at positions separated by 120°, as expected for a crystal with only a single domain.

This section has elaborated how the choice of a suitable substrate can greatly enhance the quality of a topological insulator thin film. By reproducing the Bi_2Se_3 growths of Tarakina, Schreyeck and others on InP ([32, 43–47]), an eligible rotated domain free pseudo substrate has been grown in the MBE of PGI-9. This was verified by XRD and TEM measurements, that show the neat formation of the TI on top of the rough InP substrate and the suppression of one of the rotated domains of the TI. By growing a quaternary topological insulator without rotated domains on top of the pseudo substrate, it was proven, that having an already structurally improved pseudo substrate renders the fabrication of TI films with high crystalline order possible.

Summarizing this chapter, it was successfully shown that prestructured substrates can be used to grown TI in arbitrary patterns, additionally capping the side facets of the TI. Moreover, TI stacks were grown on lattice matched InP, resulting in rotated domain free pseudo substrates and films. In the future, further research can lead to the combination of both, having an oxide and nitride prestructure on InP for patterned, domain reduced TI films.

5 Optimizing the Bulk: From the Binary to the Quaternary System

In the previous chapter, the main topic is the interface of the substrate to the topological insulator. This included describing ways to pattern the TI, using the substrate as a gate or using pseudo substrates to enable growth of high quality films. In this chapter, the focus is put on the bulk of the TI layer. First, a brief history of three-dimensional tetradymite V_2-VI_3 topological insulators is given. In the next section, the work done to grow and characterize an MBE grown quaternary TI compound is discussed.

5.1 The Tetradymite TIs

In their paper from 2007, L. Fu and C. L. Kane, which mostly treated the topological insulators HgTe and Bi_xSb_{1-x}, predicted TI behavior in Bi_2Te_3, giving rise to a steep increase in research of V_2-VI_3 TI candidates [50]. This prediction was later picked up and concretized by H. Zhang *et al.*, including also Bi_2Se_3 and Sb_2Te_3, which all crystallize in a tetradymite structure [15, 51]. The existence of single Dirac cones on each surface in these compounds was experimentally proven shortly afterwards. An advantage of the latter simple binary V_2-VI_3 TIs is that they can easily be grown as single crystals, while also providing van-der-Waals bonded layers. These can be cleaved well to create flakes convenient for device structuring and transport measurements. [2]

However, these binary compounds suffer from large bulk contributions to the transport. For Bi_2Se_3 this is due to Se vacancies and Se_{Bi} anti-site defects in the crystal, doping the bulk with electrons (n-doping). An anti-site defect describes the presence of the wrong atom on a lattice site, in this case a Se atom on a Bi lattice site. Bi_2Te_3 on the other hand can be n- or p-doped (positive holes), depending on the dominating element in the growth environment, resulting in either Te_{Bi} or Bi_{Te} anti-site defects, respectively. Though this implicates that with the perfect compound ratio during growth, bulk insulating samples are possible, controlling the fluxes and composition on the entirety of the film is difficult. Sb_2Te_3 behaves similar to Bi_2Se_3, only inverted, with Te_{Sb} anti-site defects resulting in a p-doping. [2, 16]

In order to compensate the unintentional doping in the binary compounds, various studies showed that it is possible to create a ternary compound consisting of $Bi_2Te_{3-x}Se_x$. This alloy is a topological insulator with the established tetradymite crystal structure [52]. In the quintuple layered Bi_2Te_2Se crystal system, the second and fourth layer consist purely of bismuth, while the third middle layer only contains selenium. The first and fifth layer are lastly the tellurium layers, which also form the van-der-Waals bond to the next quintuple layer, resulting in a Te-Bi-Se-Bi-Te sequence [53]. This configuration of layers is the origin of a much higher bulk resistivity compared to the binary compounds. The Se vacancies are suppressed due to the enclosure between the Bi atoms, which is secured by the higher electronegativity of Se compared to Te. A strong bond between Bi and Se simultaneously also subdues possible Te_{Bi} and Bi_{Te} anti-site defects [2, 53]. However, this neatly ordered structure will not be perfectly reproducible in an MBE due to the small timescale, in comparison to the protracted fabrication of single crystals. Moreover, the structure is only ideal for x = 1, which will not be given in the course of this chapter. Therefore, the fixed layer structure can only be considered as a guideline for the atoms, but not be explicitly reproduced.

Another important aspect of topological insulators is the position of their Dirac cone relative to their Fermi energy. In transport measurements, it is often necessary to have the Dirac point as close as possible to the Fermi energy, so that the allowed electron states have small momenta, or k values respectively. A low momentum results in a large Fermi wavelength, which is desirable for transport and interference effects. To alter the position of the Dirac point in the tetradymite TIs, another alloying is performed. While combining Se and Te helps with the bulk insulation, combining Bi and Sb in a TI to form $Bi_{2-x}Sb_xTe_3$ can be used to shift the Fermi level with respect to the Dirac cone, as shown by J. Kellner *et al.* [40]. In pure Sb_2Te_3, the Dirac point is located slightly above the Fermi level, in Bi_2Te_3 however below, hidden in the conduction band [2, 51]. Therefore, Kellner *et al.* fabricated ternary films with an antimony ratio of 94 %, i.e. $(Bi_{0.6}Sb_{0.94})_2Te_3$, in which the Fermi level was shifted to a position only roughly 5 meV apart from the Dirac point [40, 54].

The ideal topological insulator should now incorporate both the bulk insulating behavior as well as the shiftability of the Dirac cone relative to the Fermi energy. This can be realized by forming the quaternary compound $Bi_xSb_{2-x}Te_ySe_{3-y}$. As in $Bi_2Te_xSe_{3-x}$, Se forms the middle layer in the quintuple structure in between the Bi layers, while the Bi to Sb ratio in the quaternary can be adjusted so that the Dirac point is located closely to the fermi level [2, 55–57]. Thus a topological insulator is created, which combines the Dirac cone at Fermi level with bulk insulating behavior [58–60]. The values for the compound composition, i.e. x and y in $Bi_xSb_{2-x}Te_ySe_{3-y}$, can be varied, while still maintaining bulk insulation, however the compositions with (x, y) = (1.5,1.7) and (1,1) promise the highest bulk resistances and the smallest difference between Dirac point and Fermi energy [2, 61]. This makes these compositions promising candidates for transport measurements, also involving Josephson junctions and induced superconductivity on the search for Majorana modes [62, 63].

However, within all these different features already researched by many various groups, there is one commonality between all of them. They were all grown via the Bridgman method. This a growth technique employed to grow large single crystals. To do so, the elements needed for the desired compound are carefully weighed and put into an evacuated crucible. In there, they are heated above their melting temperature and stirred to produce a homogenously mixed melt. The crucible is then cooled, with a heat gradient from one end to the other, causing the melt to crystallize. This cooling is performed extremely slowly, mostly over several days, to ensure that the atoms in the melt have time to arrange themselves in the crystal lattice. The flakes used for transport experiments for example are then exfoliated [2]. This technique allows for the production of single crystals of every stoichiometry, however the process is lengthy and the exfoliation difficult and restricted to small flakes.

Growing the quaternary topological insulator system in a MBE system would drastically reduce the time needed, allow for the combination with advanced MBE techniques and additionally it would be possible to have large samples for further experiments. However, there is no literature of MBE grown quaternary TIs, suggesting that it has never been done before, at least not successfully. Therefore, attempts to produce the quaternary system in the MBE of the PGI-9 were initiated. The results of the growths of $Bi_xSb_{2-x}Te_ySe_{3-y}$ will be shown and discussed in the next section.

5.2 The Quaternary System

To grow the $Bi_xSb_{2-x}Te_ySe_{3-y}$ system, the right temperatures for the effusion cells need to be found first. This creates a large parameter space of the effusion cell temperatures and the substrate temperature. The latter can initially be neglected, as the first growth attempts are performed on 4 inch Si (111) wafers on single wafer holders, whose heat conduction and usual substrate temperatures are known from earlier growth processes. For the effusion cell temperatures, a presumption is done: If the recipes for the growth of the two ternaries $Bi_xSb_{2-x}Te_3$ and $Bi_2Te_ySe_{3-y}$, with the compound ratios x and y for the desired quaternary, are determined by carefully adjusting the partial pressures, it may be possible to combine them. Due to growth experiments by Kellner, Weyrich *et al.* in the same chamber, the possibility to fabricate the $Bi_xSb_{2-x}Te_3$ system with varying x is already established [40, 54]. The $Bi_2Te_ySe_{3-y}$ system however has not been grown in the chamber before, since Te and Se are both deposited in overpressure, impeding finding the exact effusion cell temperatures for both. Thus, a series of growths is performed to find the right temperatures for the Te and Se cell. In order to decrease the parameter space, the temperature of the Bi and Te cells is kept constant during the growth series at 500 °C and 330 °C, respectively. First, a growth with Se at 110 °C is performed, which is the conventional temperature for the growth of Bi_2Se_3 films in the MBE chamber. This results in a ratio of $y = 0.7$, i.e. $Bi_2Te_{0.7}Se_{2.3}$, which suggests that it is possible to grow the $Bi_2Te_ySe_{3-y}$ system in the MBE chamber of the PGI-9 HN. The stoichiometry of the grown compounds is measured with two methods, Rutherford backscattering spectrometry (RBS) and by the comparison of peak positions in the x-ray diffractometry results (see chapters 3.3 and 3.2, respectively).

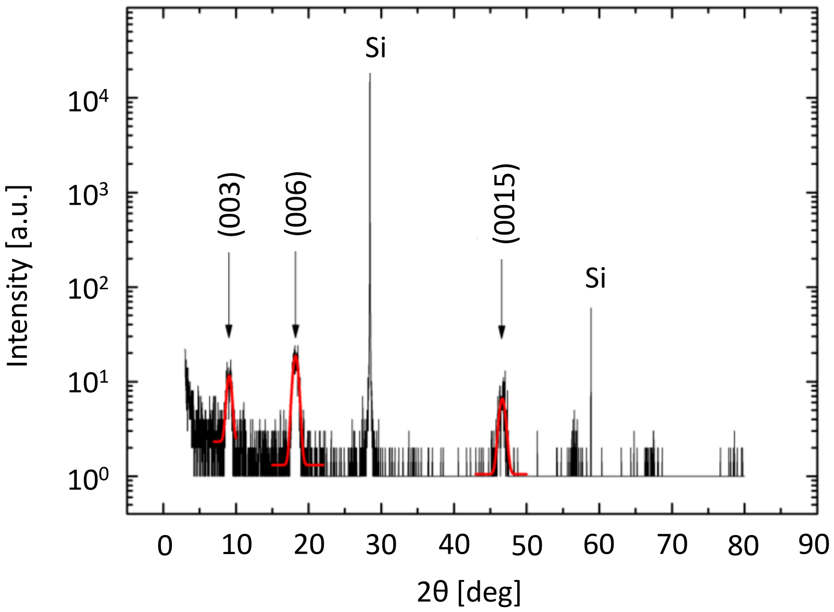

Fig. 5.1: *2θ XRD scan data of the $Bi_2Te_xSe_{3-x}$ ternary with T_{Se} = 90 °C. At the (003), (006) and (0015) reflection peaks, Gaussian curves are fitted to the data to determine the exact peak position. Measurements performed by Gregor Mussler.*

The latter method is illustrated in Fig. 5.1. In the ω/2θ scan of the ternary compound, in this case with T_{Se} = 90 °C, first the positions of the (00n) reflection peaks are identified. Gaussian curves are then fitted to the data (red curves) to determine the exact 2θ value of the peak with an error estimated from the standard deviation. The results are shown in Tab. 5.1.

Reflection	Bi_2Te_3	$Bi_2Te_xSe_{3-x}$	Bi_2Se_3
(003)	8.6°	(9.07±0.09)°	9.2°
(006)	17.4°	(18.2±0.2)°	18.6°
(0015)	44.6°	(46.6±0.5)°	47.6°

Tab. 5.1: *2θ XRD of the two binary Bi TIs and the combined ternary, taken from literature or the measurement shown in Fig. 5.1, respectively.*

Comparing the 2θ value with the values for pure Bi_2Te_3 and Bi_2Se_3, the stoichiometry can be estimated as follows. First the difference between the binary compounds is calculated and related to the difference between Bi_2Se_3 and the ternary. Multiplying the ratio by 3 results in the value of x, the portion of Te in the compound, for example for the (006) reflection:

$$x = 3 \cdot \frac{BiSe - BiTeSe}{BiSe - BiTe} \overset{(006)}{\Longrightarrow} 3 \cdot \frac{18.6° - 18.2°}{18.6° - 17.4°} = 3 \cdot \frac{0.4°}{1.2°} = 1(\pm 0.01) \qquad (5.I)$$

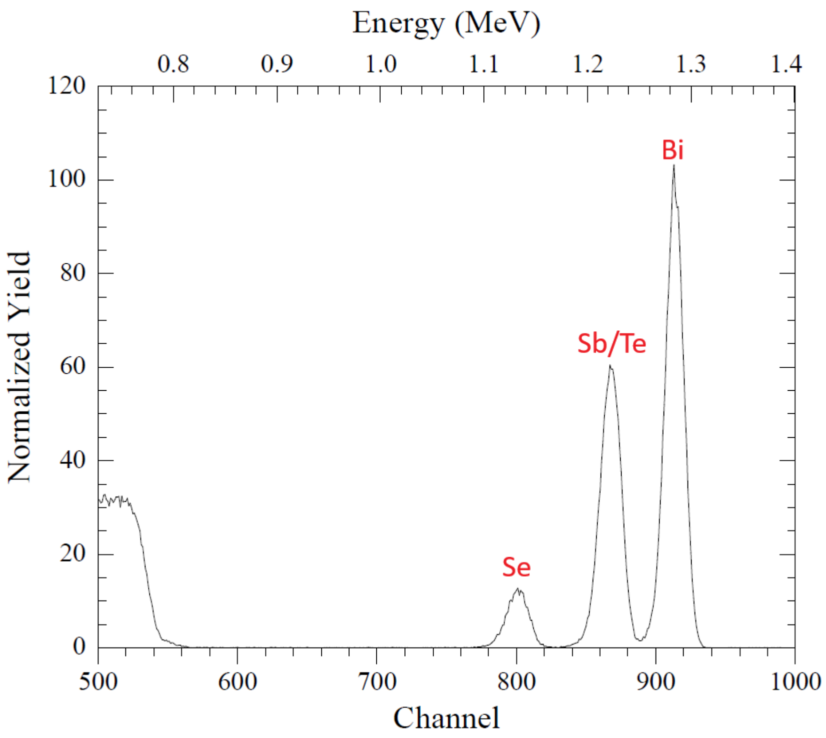

Fig. 5.2: *Example of a measurement of the stoichiometry of a quaternary sample by Rutherford backscattering spectrometry. The y axis indicates the number of signals normalized by total amount of charge carriers accelerated onto the sample. On the x axis, the channel number and the corresponding energy in MeV is plotted. Due to the similar weight of Sb and Te, the peaks are indistinguishable.*

The x values for all peaks are thereupon averaged, yielding the stoichiometry of the ternary determined by x-ray diffractometry.

In figure Fig. 5.2, the RBS data for the (1.4, 1.8) quaternary is shown exemplarily for the stoichiometry determination via RBS. From 1.0 to 1.3 MeV, three peaks are clearly distinguishable, which correspond to the elements in the compound. The plateau up to 0.8 MeV occurs due to the signal from the silicon substrate and can be neglected. The first peak at 1.15 MeV can be assigned to Se and the last peak at 1.28 MeV to Bi only. The peak in the middle at about 1.22 MeV is generated by Sb as well as Te. This is due to RBS being a highly weight sensitive method. As Bi, Se and Sb/Te all belong to different periods in the periodic system, their masses differ greatly, resulting in separate peaks. Sb and Te however are part of the same period and differ only by 6 u. To determine the stoichiometry, the program XRump is used. By inserting the peak data and corresponding element, a gross number of atoms of the corresponding element per cm^2 is calculated. For Te and Sb, the peak is evaluated twice, with Te and Sb each, and the resulting density then averaged. With the resulting elements, percentages of atoms in the compound are calculated, which then can be used to determine the ratios of Se and Bi immediately. For

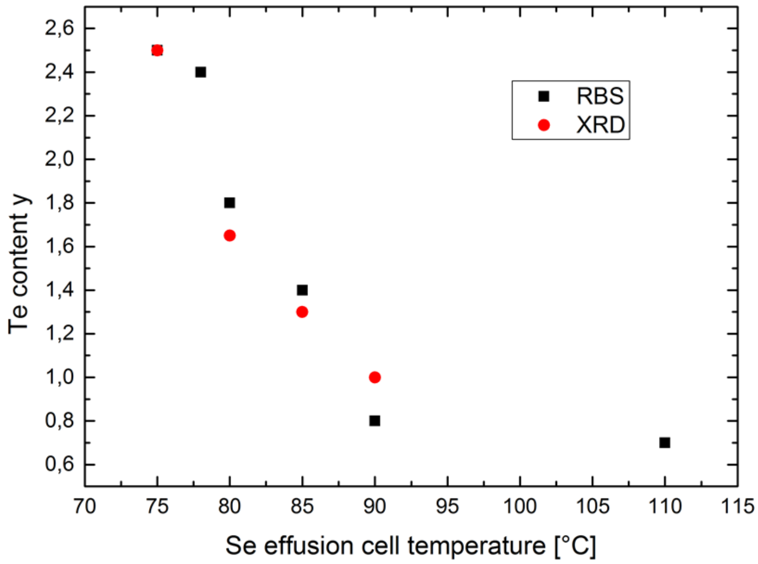

Fig. 5.3: *Results of the growth series of* $Bi_2Te_ySe_{3-y}$*. Depicted is the ratio y of Te in the compound depending on the temperature of the Se effusion cell. The black data points are determined by RBS, the red by XRD peak estimations.*

the amount of Te/Sb in the compound the determined percentage of Sb+Te has to be split up. This can be calculated with:

$$3 \cdot (Bi + Sb) = 2 \cdot (Te + Se) \tag{5.II}$$

$$SbTe = Sb + Te \tag{5.III}$$

The element symbols in the equations symbolize the percentage of the corresponding element in the quaternary system, with SbTe being the combined value determined with RBS. In pure Bi_2Te_3 the Sb and Se ratio would be 0, the Bi = 0.4 and the Te = 0.6. The first equation (5.II) originates in the set ratio between the group VI and VII elements in the quaternary VI_2VII_3 system, the second, (5.III), is trivial. Combining the two equations and solving for Te or Sb gives:

$$Te = \frac{3Bi + 3SbTe - 2Se}{5} \tag{5.IV}$$

$$Sb = \frac{2SbTe + 2Se - 3Bi}{5} \tag{5.V}$$

With the equations (5.IV) and (5.V), the percentage of Sb and Te in the quaternary can then be calculated.

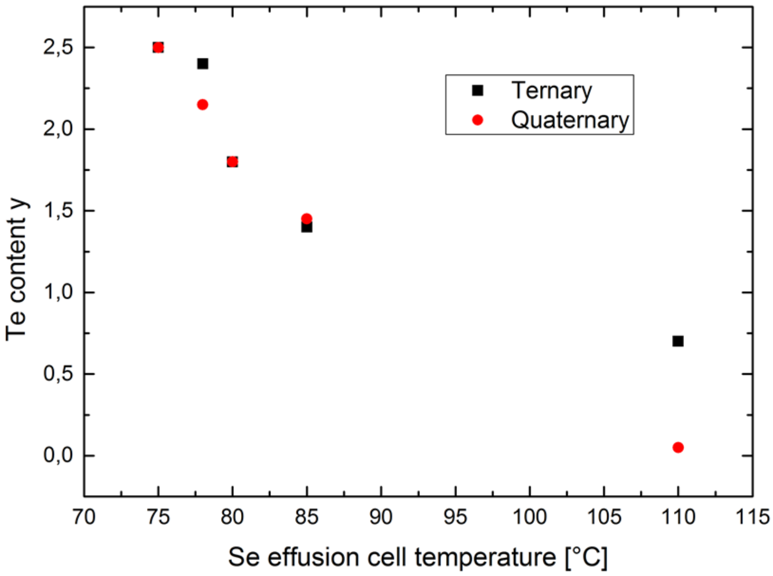

Fig. 5.4: *Comparison of the recipes for the ternary and the quaternary TI. The Bi, Sb and Te effusion cell temperatures are kept constant, only the Se temperature is shifted. Depicted is ratio of tellurium y in the compounds, determined by RBS, depending on the Se source temperature. The ternary and quaternary TI exhibit the same behavior in y with similar values.*

The result of the further growth series of the $Bi_2Te_ySe_{3-y}$ ternary is shown in Fig. 5.3. In this figure, the blue data points depict the stoichiometries measured with RBS, while the orange points show the values estimated via the relative peak position. From 75 °C to 90 °C, the Te portion in the ternary compound decreases with increasing Se effusion cell temperature as expected; the behavior is almost linear. From T_{Se} = 90 °C to 110 °C, the Te ratio is saturated at about y = 0.7.

With this result that the Te/Se ratio can be shifted by adjusting the selenium effusion cell temperature T_{Se}, it is now possible to pursue with the growth of the quaternary system. However, the set of desired (x, y) in $Bi_xSb_{2-x}Te_ySe_{3-y}$ has to be decided first. In [59], Ren *et al.* showed that there exists a line of compositions with bulk insulating behavior, but only two compositions on that line also possess a Dirac point in close proximity to the Fermi level. These are the pairs (x, y) = (1, 1) and (1.5, 1.8).

The substrates for the growths are n-type 4 inch Si (111) wafers with a high resistance (>2000 Ω·cm). As explicated in chapter 4.1, the wafers are cleaned before growths with a dip in piranha solution and a subsequent dip into 1% HF for 10 min each and then transferred to the MBE chamber. After annealing to 700 °C for hydrogen desorption, the substrate is cooled to T_{sub} = 300°C. The effusion cell temperatures are set to T_{Bi} = 470 °C, T_{Sb} = 417 °C and T_{Te} = 330 °C, corresponding to the recipe of the x =1 ternary, while the Se effusion cell temperature T_{Se} is shifted. When the set substrate temperature is reached, the Te shutter is opened first for 30 s to saturate the dangling bonds. Next, the Bi shutter is opened for 3 minutes to create a thin layer of BiTe before the Sb and Se shutters are opened subsequently. This process is adopted from the growth in the prestructures and supports a smoother crystal formation when the Sb is introduced. By contrasting the growth stoichiometries of the quaternary and the ternary system with equal T_{Se}, the assumption made beforehand can be verified, that the recipes for the two ternaries can be combined linearly. Fig. 5.4 shows the comparison of the recipes for the ternary and quaternary system. At equal T_{Se}, the Te ratio is similar for compounds with and without Sb. Moreover, for both TIs the Te ratio decreases with increasing T_{Se}. While at T_{Se} = 110 °C the ratio of Te in the system is differing by about 0.6, in the for later growths more important region from 70 °C to 85 °C, the ternary and the quaternary compounds contain similar amounts of Te in the crystal lattice. This suggests that the assumption made beforehand is true and that the ternary and quaternary recipes are linearly combinable, after carefully adjusting the effusion cell temperatures of Te and Se.

The most promising compound grown in this first growth series of the quaternary system can be found at T_{Se} = 80 °C, resulting in (x, y) = (1.1, 1.8). Over the course of this master's thesis, the Se temperature for this composition had to be changed to 93 °C due to refilling of the MBE sources and a following new ratio of Se and Te fluxes. As mentioned before, the preferable ratios are (1, 1) and (1.5, 1.8) [59]. Since in the first growth series an (1.1, 1.8) ratio was accomplished while varying the temperatures, the focus of this work is put on the (1.5, 1.8) compound for the following growths. Therefore, T_{Bi} is set to higher temperatures to increase the bismuth percentage in the TI, whereas the more complexly colluding Te and Se temperatures are kept constant. By growing a series of samples as for the Se/Te ratio, the best T_{Bi} is found at 470 °C, at which the combination (x, y) equals (1.4, 1.8), corresponding to $Bi_{1.4}Sb_{0.6}Te_{1.8}Se_{1.2}$, confirmed by Rutherford backscattering spectrometry. The RBS data for this sample is shown in Fig. 5.2. For further characterization, the sample is investigated with XRD. First, a ω/2θ scan is performed to determine the (00n) reflections, by which the lattice constant c can be calculated. The results are shown in Fig. 5.5 a). Comparing the data with those measured by Ren *et al.* shows a good agreement of the peak positions as well as the relative height of the peaks for a (1.5, 1.7) quaternary [59].

In Fig. 5.5 b), the reciprocal space map of the compound calculated from the (1, 0, -1, 20) reflection is shown. The bright spot signifies the value of the lattice constants of the quaternary compound, which amount to a = 4.285 Å and c = 29.95 Å. In the space map, the positions of the three binary topological insulators are also highlighted for reference. Comparing the reference positions and the position of the quaternary peak suggests, that the grown film consists of a mixture of the three binary TIs, more akin to Bi_2Te_3 and Sb_2Te_3 than Bi_2Se_3, which is confirmed by the RBS data. Moreover, the existence of one distinct peak suggests that only one crystal lattice is present, whereas a double peak would indicate the coexistence of two separate lattices.

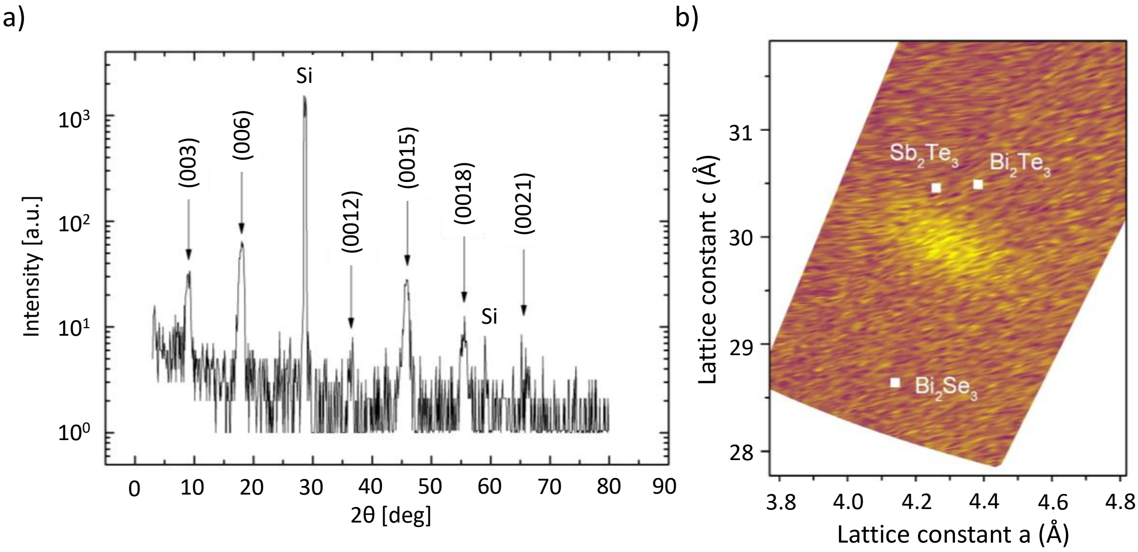

Fig. 5.5: *a) 2θ scan of the quaternary sample. Here characteristic peaks of the tetradymite crystal structure are labelled with the corresponding index (00n). b) Reciprocal space map of the quaternary sample. The color indicates the intensity, counts per second, for a lattice constant combination. Yellow indicates high, purple low intensity. Measurements performed by Gregor Mussler.*

Together with the peaks of the 2θ scan, these findings confirm that a tetradymite crystal has been fabricated, incorporating all four elements in the crystal lattice. However, to prove that a quaternary topological insulator has been fabricated in the MBE, measurements of the electronic structure are necessary. Therefore, a sample with the exact same recipe is grown and transferred within a vacuum suitcase at 10^{-10} mbar into the ARPES chamber of the PGI-6. As explained in section 3.4, the ARPES utilizes the photoelectric effect to uncover the band structure of a material in proximity to the Fermi level. The results of the ARPES investigation are shown in Fig. 5.6, where a) shows the electronic structure of the quaternary system around the Γ point at the center of the Brillouin zone. On the y-axis, the binding energy (E_B) needed to excite a photon from the bands to the continuum is plotted, on the x-axis the wave vector is indicated. The data for the graph was taken with the normal emission of a xenon lamp with a photon energy of $E_{Xe} = 8.4$ eV at room temperature. The color indicates the intensity of the signal, from blue for a low intensity to red for a high intensity and therefore a high density of states. Measurements at lower temperatures could not be performed, since the setup of molybdenum sample holder used for the growth did not provide a high heat conductance. The holders used for ARPES need to be flat on the backside, which is pointing upwards in the MBE chamber. Therefore, the sample has to be clamped into the holder, which in the case of the used holder is executed by a thin bent molybdenum sheet. This provides only little contact between the sample and the holder, resulting in a reduced cooling power. Thus, the sample was only cooled to some degrees below 0 °C.

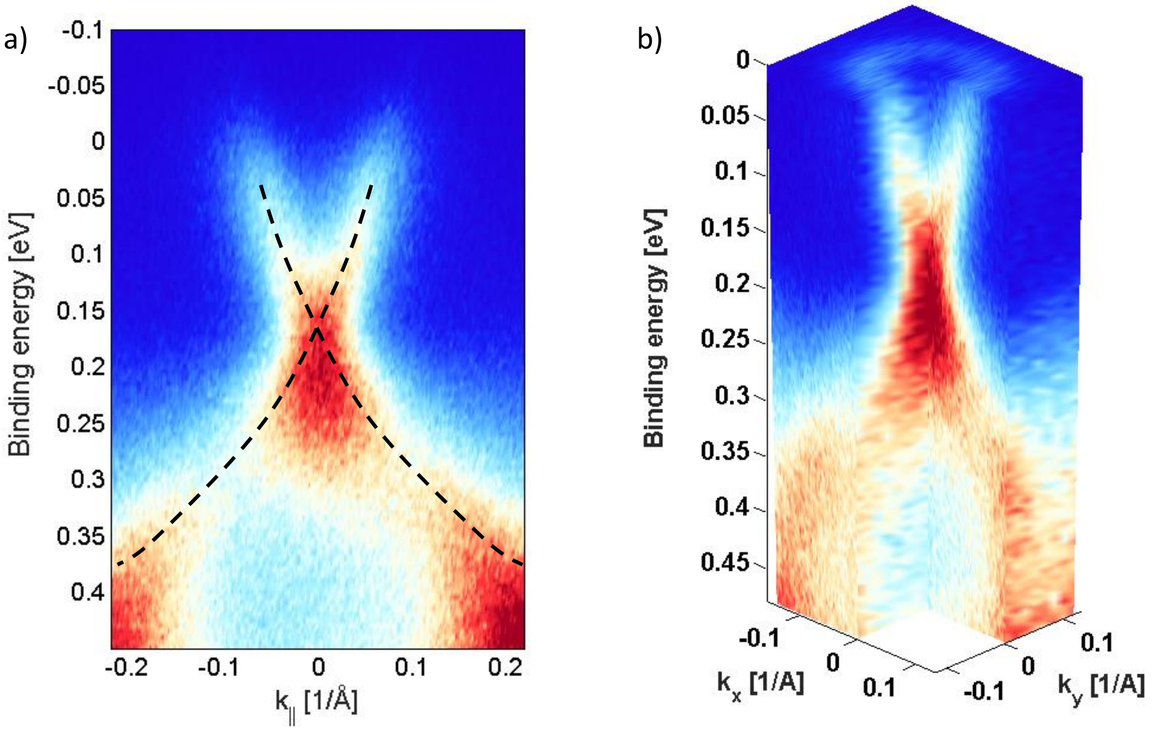

Fig. 5.6: *ARPES measurements of the (1.4, 1.8) quaternary system. The color indicates the intensity of the measured signal. Graph a) shows a cut through the Dirac cone at room temperature. The bulk valence states are visible at high binding energies. At roughly 0.15 eV a Dirac point is located, indicated by the dotted line. In b), the homogeneity and cone-like structure can be examined at lower temperatures. Measurements performed by Tristan Heider at PGI-6.*

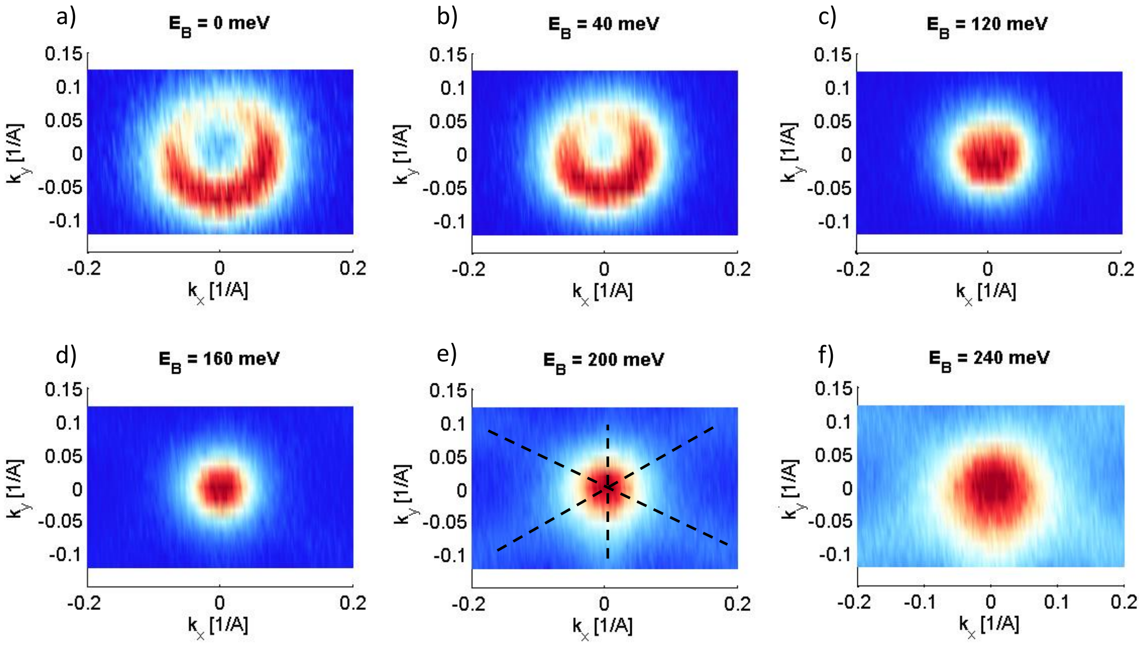

Fig. 5.7: *Constant energy cuts through the data of Fig. 5.6. The size of the circles indicates that the Dirac point is located between 160 meV and 200 meV binding energy. Dotted lines are used as a guide to the eye to illustrate the six-fold valence band symmetry in the constant energy graph at 200 meV. Measurements performed by Tristan Heider at PGI-6.*

The relatively high temperature caused high levels of noise in the measurements with the surface sensitive helium lamp, which is why the investigations were performed with the xenon lamp only. In Fig. 5.6 b) the result of the measurement at lower temperatures is shown. Here, not only one k-direction is scanned but also the perpendicular direction, providing a three-dimensional view of the Dirac cone. The position of the Dirac cone can be estimated to be at approximately 150 meV. Since the valence bands extend from roughly 250 meV downwards, the Dirac cone is free standing in the energy gap between the valence and conduction band. The shape of the Dirac cone resembles that of Bi_2Se_3 and ARPES measurements on quaternary systems [16, 55]. Fig. 5.6 b) also gives information about the symmetry of the Dirac cone. As is visible at 0 eV binding energy, the cone forms a neat circular shape in the constant energy plane at $E_B = 0$ eV, which forms the Fermi surface. For confirmation of the circular shape, Fig. 5.7 shows constant energy cuts through the Dirac cone. By the size of the circle of high intensity at the gamma point, the estimation of the position of the Dirac point can be concretized to be between 160 meV and 200 meV binding energy. This finding is similar to measurements performed by Arakane *et al.* on flakes exfoliated from single crystals grown by the Bridgman method, where they determined a binding energy of the Dirac point of 120 meV at 30 K in the (1.5,1.7) system [55]. Investigating Fig. 5.7 further, two features need to be explained in further detail. At low binding energies from 0 meV to 80 meV, an asymmetry in the circular shape can be observed, suggesting a higher density of state at negative k_y and positive k_x. This is an artifact of the measurements in the ARPES chamber and is not caused by the sample itself. The other feature however is a remnant of the symmetry of the tetradymite topological insulator crystal structure. At high binding energies, reaching into the bulk valence bands of the TI, a star like pattern of high density of states can be identified, indicated by the dotted lines in Fig. 5.7 e) at 200 meV. This is due to the six-fold symmetry of the valence bands in the topological insulator [57]. By comparing the center of the density of states with the intersection of the dotted lines, the effect of the asymmetry that is best visible at low E_B can already be observed.

The significance of the existence of a free-standing Dirac cone lies in the implication, that for a neat electronic structure, a high structural order in the crystal is needed. Therefore, the ARPES data show, that the grown quaternary topological insulator not only possesses the desired electronic structure, but the crystal structure is also well ordered. Comparison with TIs grown by Bridgman method show similar results, further proving the success of the MBE growth of a quaternary system [61].

In this chapter, it is shown that a quaternary tetradymite topological insulator can be grown in a molecular beam epitaxy chamber by combining the growth parameters of the BiTeSe and BiSbTe ternary TIs. The grown films are investigated by XRD and RBS to show that a compound ratio of (x, y) = (1.4, 1.8) is achieved, with lattice parameters supporting this result. Moreover, XRD shows distinct peaks, indicating an ordered tetradymite crystal structure. This is additionally confirmed by ARPES measurements, also showing a clear and free-standing Dirac cone. For further characterization of the TI, transport experiments are performed in chapter 7.2 to determine the mobility and charge carrier concentration. First however, a novel way of patterning the film for the transport measurements will be detailed in the next chapter 6.1.

6 The Interface to the Continuum and *in situ* Device Fabrication

This chapter will address the last section of a topological thin film, the surface of the film that is exposed to the continuum. As long as the sample is kept in the vacuum, no significant changes occur in the electronic structure of the TI, except for possible aging effects due to doping with stray atoms in the chamber [64]. However, as soon as the surface comes in contact with ambient conditions, it oxidizes, influencing the electronic structure of the TI [65–67]. Additionally, chemical and physical processes performed after the TI growth to pattern the film for further experiments can have a destructive impact on the surface states of the TI. How these negative impacts on the thin films can be prevented and how this influences the way topological insulator devices are fabricated will be the topic of the following sections.

6.1 Protecting the Surface States: Capping

In their works on the binary topological insulators Bi_2Se_3, D. Kong *et al.* and A. J. Green *et al.* describe the effects of oxidation on the properties of the TI [65, 66]. Kong *et al.* show in their paper, that during exposure to air more and more BiO_x forms in the compound, which Green *et al.* later observe as small crystallites on the surface. With depth resolved ARXPS (Angle Resolved X-ray Photoelectron Spectroscopy), they also show that the ratio of BiO_x to Bi_2Se_3 changes from bulk to surface. At and near the surface, the BiO_x outweighs the Bi_2Se_3, potentially destroying the precious surface states. K. Hofer *et al.* perform experiments on Bi_2Te_3 and also consider the effects of surface oxidation [67]. They determine that the exposure to air results in the formation of defects, which increases the amount of non-surface state charge carriers. Thus, the transport properties of the surface states that were supposed to be measured are heavily suppressed by the conventional conductance in the sample.

In the previous chapters, the interface to the substrate was optimized to have high quality thin films with only few defects, so that the bulk conductivity is low. Moreover, the quaternary system further decreases the conductivity due to the cancellation of acceptors and donors in the crystal structure. With this, the optimal conditions are prepared for a high bulk resistivity and high surface conductivity in the surface states. If the latter are however destroyed or impaired by surface contaminations, all the previous work becomes irrelevant. Therefore, it is of utmost importance to protect the surface states from any contaminations.

A possible solution to the contamination of the surface is the use of a *in situ* deposited capping layer on the TI film. There are many possible materials that can be used as a capping layer, that are either already oxidized or immune to oxidation when deposited on the sample, for example Si_3N_4 or stoichiometric SiO_2. Moreover, there are materials that oxidize to a certain depth when the grown sample is exposed to air, so that exactly that thickness of the original element can be deposited on the TI film, later forming the capping, for example pure Al which oxidizes to Al_2O_3. However, they on the one hand need to be available in the growth chamber and on the other hand must not influence the TI themselves.

In the case of the MBE chamber of the PGI-9, two approaches are possible. The first is the capping with Te or Se [68]. After the TI growth, the sample is cooled below 0 °C and a several nm thick layer of Te/Se is grown. At the low temperatures, the deposited films are amorphous and after exhibition to air react with oxygen to form a protective oxide. The capping can easily be removed by heating the sample to roughly 150 °C without harming the TI underneath [69]. Which element is suited is determined by the composition of the underlying TI. In the case of Bi_2Se_3 a Se capping can be applied and vice versa for Bi_2Te_3. Otherwise the group VI element of the capping will substitute some of the elements in the TI. For a Se capping Virwani *et al.* showed, that up to a depth of 7 nm in the underlying Bi_2Te_3 the Te was substituted by Se without structural changes, effectively creating an unintentional heterostructure [69]. These findings are presumably also applicable for the ternary BiSbTe compound. However, in the case of the quaternary sample, which is the focus of this work, the choice of capping material is more complicated, since both group VI elements are present in a delicate ratio. Capping the quaternary with either Te or Se will very likely result in a change of ratio, overriding the work previously done to find the right compound.

This will however not be discussed in this work, as the second possible approach was chosen to cap the TI films. This approach utilizes a thin layer of Al, which is deposited *in situ* in the MBE on the TI after growth. The possibility to use Al and AlO_x correspondingly was first illustrated by Lang *et al.*, and later picked up by Ngabonziza *et al.* [70, 71]. The former deposited pure Al on Bi_2Se_3, while the latter deposited Al_2O_3 via pulsed laser deposition (PLD) on Bi_2Te_3. Lang *et al.* were able to measure sensitive transport phenomena like Shubnikov-de Haas oscillations and weak antilocalization effects in the capped thin films, promising equal results for the measurements of the quaternary system investigated in this work.

An example for the capping with Al and the subsequent formation of AlO_x was already shown in Fig. 4.5 a) and b). The prestructured samples are cooled below 0 °C after growth and 2 - 3 nm of Al are deposited on the sample. When the sample is then exhibited to ambient conditions, the Al reacts to form aluminum oxide. Since it is important that no elemental Al is left on the TI which would later act as a short circuit in transport measurements, the Al layer thickness is adjusted so that it oxidizes fully. The full Al layer therefore is converted to the native oxide. Another possibility to cover the sample with AlO_x is by atomic layer deposition (ALD), which can be performed in the Nanocluster of the Helmholtz Nanofacility. To not break the vacuum, the samples are transferred after growth to the cluster with the vacuum-suitcase.

The importance of capping the topological insulator to protect its surface states is hereby explained, but for many applications of the topological insulator thin films, the capping has to be removed again for further experimentation. In the case of the Te or Se cappings, annealing can remove the protective layer while in vacuum, for example in ARPES. But for experiments like transport measurements, where the film needs to be structured and contacts need to be applied *ex situ*, this is not an option. The AlO_x capping moreover cannot be removed by annealing, but needs to be etched by chemical or physical processes, which could also potentially harm the TI surface. A possible answer to how these hindrances can be overcome will be explicated in further detail in the following paragraphs.

6.2 *In situ* Device Fabrication via Stencil Lithography

This section will deal with the fabrication of *in situ* devices in a sense that the surface of the topological insulator will never be directly exposed to ambient conditions and therefore air. To do so, a technique called stencil lithography is used. Stencil lithography performed in the MBE can be compared to the use of stencils or templates in graffiti art. In the latter, the picture to be reproduced is cut into a, for example, cardboard piece and the paint is sprayed through the openings to create an exact image of the cut out.

Transferring this image to the MBE, the spray paint is replaced by the evaporated materials, while the patterned cardboard piece is substituted with a patterned membrane or mask. By inserting the mask after depositing the TI film, metallic contacts can be grown *in situ* immediately on the TI film. Removing the mask afterwards and depositing a thin layer of Al on the whole sample would then provide a capping. By this process, TI films with contacts and capping can be fabricated *in situ* in the MBE chamber. The TI film would never be directly exposed to air, protecting the surface states from contaminations. In the following sections, this process will be explained in further detail. Firstly, the conventional process and other approaches to fabricate Hall bars will be explained. Secondly, the mask layout and the design of the holders used in the MBE will be established. Next the process of mask fabrication will be detailed and lastly the results of growth through the masks will be detailed.

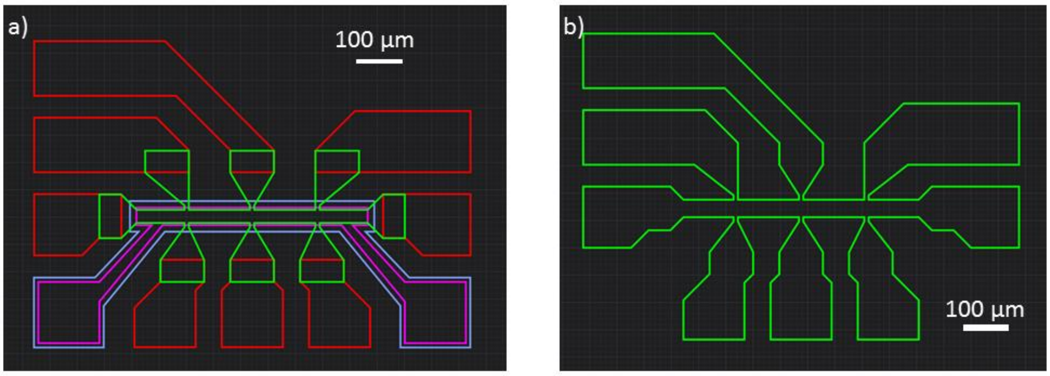

Fig. 6.1: *a) Layout of the conventional Hall bar pattern. The outline of the Hall bar itself is shown in green, with eight pads extending to the sides for contact deposition. The contacts are shown in red and overlap with the Hall bar. In blue, the pattern of the gate dielectric is illustrated, with the gate contact outline itself indicated by the purple pattern. b) Combined pattern used for structuring Hall bars with metal already deposited on top.*

6.2.1 First Attempts at Quasi Grown Devices

In order to characterize the transport through a topological insulator thin film, and also through thin films of other materials, a very common measurement setup is the Hall bar. It is named after Edwin Hall, who also gave his name to the eponymous Hall effect. The samples to be investigated are contacted at four ideally perpendicular positions. A current is sent through two opposing contacts, while a magnetic field is applied to the sample perpendicular to the plain spanned by the four contacts. Due to the magnetic field and the resulting Lorentz force a voltage arises between the sides, the Hall voltage U_H, which is measured with the remaining two contacts. By investigating the measured U_H and varying the magnetic field, many qualities of the thin film sample can be determined like mobility and charge carrier concentration, this will however be explained in further detail in chapter 7.

Conventionally, topological insulator thin film Hall bars are fabricated from a simple TI film on Silicon. The films are patterned via optical lithography as shown in Fig. 6.1 a). First, the Hall bar itself is etched out of the film by ion beam etching (IBE), green in Fig. 6.1 a), secondly metallic contacts (red) are put on the Hall bar which are later bonded to a carrier compatible with the measurement setup. If experiments with a gate are to be performed, an additional dielectric (blue) is deposited on the bar, on top of which an additional contact is put to apply a gate voltage (purple).

However, as stated in the previous paragraphs, TI films without capping oxidize or get contaminated by other elements, causing the features of the surface state transport to be suppressed. Including a capping may resolves this, but it also impedes the fabrication of Hall bars. The contacts cannot be deposited directly on the sample, due to the isolating layer on the TI. Therefore, *ex situ* processes need to be utilized on the contact to TI

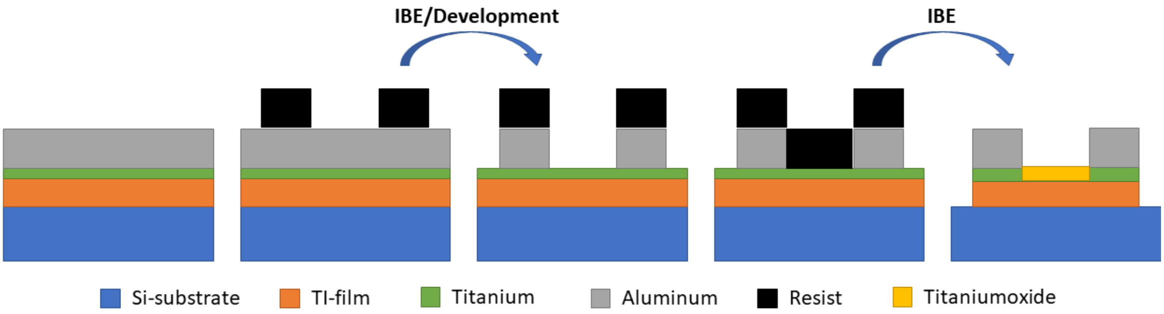

Fig. 6.2: *Process steps of creating a Hall bar out of a layered system without exposing the TI surface. The resist is patterned into a Hall bar structure with optical lithography.*

interface, which may lead to non ohmic contacts or contamination of the TI surface due to applied plasmas or ageing. Hence, the optimal way of fabricating a Hall bar structure would be to execute all processes *in situ*, effectively never leaving the vacuum, or at least to have the Hall bar and contacts finished after MBE growth.

This is first attempted by growing a layer of TI with a thickness of 20 nm on a Si (111) sample and subsequently covering it with a layer stack of 3 – 5 nm titanium and 50 nm of aluminum as shown on the left in Fig. 6.2. The thick aluminum is supposed to be used as contact pads and the Ti acts as a diffusion barrier between the TI and the aluminum on top. Earlier experiments in our group had shown that if Al is deposited on the topological insulator directly, it diffuses into the TI, vastly decreasing the transport properties [72]. Presumably, the Al forms insulating compounds with the elements in the TI, creating a barrier between contact and film, hindering the current from entering the sample film. By applying a thin layer of titanium, the Al is kept from entering the TI without forming an insulating barrier. With this layer stack prepared, the fabrication of the Hall bar can be initiated. The result would then be a quasi grown device, since only excess Al would have to be removed. The process is illustrated in Fig. 6.2.

First the sample is covered with optical resist, into which the selected Hall bar structure is patterned. Since the complete sample is covered with topological insulator and the Ti/Al stack, the majority of the film needs to be etched, so that only TI in the form of the desired Hall bar is left on the sample. However, since the metal for the contacts is already deposited on the TI film, the Hall bar and the corresponding contacts need to be patterned together. In case of a conventional Hall bar, only the bar is left after etching and the contacts are deposited on the uncovered Si substrate and parts of the patterned TI Hall bar. Therefore, for the preparation in the resist, only a separate bar pattern and contact pattern is available. Thus, a new lithography mask is designed, to combine both bar and contacts. The layout for the combined structure is shown in Fig. 6.1 b). The next step is then to protect only the contact pads with resist and etch the excess Al on top of the TI Hall bar with IBE down to the Ti, leaving a TI Hall bar with Ti/Al contacts. In Fig. 6.2, this process is illustrated by the double IBE process.

To pattern the Hall bar, the optical resist AZ 5214 E by MicroChemicals GmbH is used, which can be used as a negative or positive resist**.** Before coating with resist, the sample is cleaned in acetone and isopropanol for each five minutes, before heating to 120 °C for five minutes to evaporate left over fluids. After coating the sample on a spin coater, the resist is baked for five minutes at 90 °C and taken to optical lithography. There, the sample is covered with the optical lithography mask, onto which the aforementioned structures of Hall bar combined with contacts have been patterned with chromium. The parts of the sample, which are not shadowed by the chromium are illuminated with ultraviolet light from a mercury discharge lamp, providing light with a wavelength of λ = 365 nm. AZ 326 MIF developer, an alkaline solution of 2.38 % TMAH (Tetramethylammoniumhydroxide), is used to develop the resist, removing all resist except the hardened patterns on the contacts and bar. The parameters for the optical lithography are further detailed in Tab. 6.1.

AZ 5214 E optical lithography	
Dehydration	130 °C for 5 min
Spin coating	45 s with 4000 rpm
Softbake	90 °C for 5 min
Illumination	4.1 s with 7 $\frac{\mathrm{mW}}{\mathrm{cm}^2}$
Inversion	115 °C for 2 min, 20 s illumination with 7 $\frac{\mathrm{mW}}{\mathrm{cm}^2}$
Development	AZ 326 MIF for 35 s
Cleaning	5 min DI rinsing

Tab. 6.1: *Process parameters of the optical lithography with AZ 5214 E resist. Before dehydration, the samples are cleaned with 5 min dips in acetone and isopropanol.*

When this process was first executed, the color of the sample changed drastically during the development. The bright metallic shine of the aluminum deposited on the whole sample surface vanished, displaying a darker metallic shine, familiar from the surface of Si or topological insulators themselves. Investigations with optical microscopy and scanning electron microscopy showed that the aluminum is etched by the development with the alkaline MIF developer.

With this finding, the process is altered. First, only the contacts are patterned with optical resist, since only there the thick Ti/Al stack is needed. The samples are then developed for 80 seconds instead of the conventional 35 seconds to remove not only the excess resist, but also to etch the excess aluminum that is covering the Hall bar and the rest of the sample, as shown in Fig. 6.2, using development instead of IBE in the first step. The etching is stopped by the Ti interlayer, which is supposedly resistant to the alkaline developer [73]. The old resist is then removed and new resist in the form of the combined pattern is structured onto the etched pattern. The result of this process step is shown in Fig. 6.3 a).

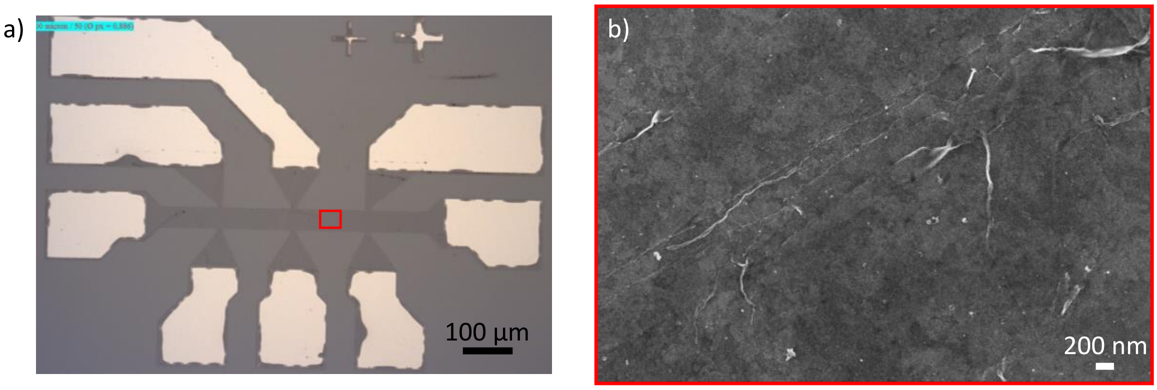

Fig. 6.3: *SEM micrographs of the etched Hall bar. In a) the structured Hall bar is shown. The Aluminum is patterned to the Hall bar layout, in dark grey the profile of the Hall bar itself is highlighted by resist. The resist is later used to remove the excess TI surrounding the Hall bar. In b), the marked area in a) is magnified after removal of the resist, illustrating the damaged surface of the TI.*

With ion beam etching, the excess TI surrounding the Hall bar, not covered by resist, is subsequently removed and only the desired device is left (c.f. Fig. 6.2). The TI is covered with Ti, which oxidizes and forms a TiO_x capping [74].

The SEM micrograph in Fig. 6.3 a) shows the TI film with the Al contacts left intact after developing. Between the contacts, in dark grey, the TI film is maintained, supposedly capped with titanium and covered with resist. However, investigation with the scanning electron microscope after the removal of the resist reveal a large-scale destruction of the TI, shown in Fig. 6.3 b), although Ti was included as an etch stop. Presumably the thickness of the titanium is either not high enough to fully prevent the diffusion of the aluminum into the topological insulator and the compounds formed of Al and TI are also etched by the developer, or the longer development causes the etching of the TI film itself. Either way, this approach to protect the surface during the Hall bar's preparation for transport measurements is not feasible and another approach needs to be found.

At this point, a concept for *in situ* device fabrication developed by Daniel Rosenbach and Peter Schüffelgen was picked up. They had worked on using patterned membranes made of silicon nitride in the MBE and utilizing them as stencils for the deposition of metals, a technique called stencil lithography [72, 75]. In their work, they structured masks bought from the company Norcada Inc. and developed a holder to position the mask under the sample in the MBE without breaking the vacuum for the sample. However, the distance between the mask and the sample was too large, causing the deposited structures to enlarge or blur. With this technique, the metallic contacts could be deposited directly, avoiding the necessity to pattern the contacts *ex situ* after growth. Moreover, by combining this technique with the prepatterned samples shown in section 4.1, deposition of topological insulator only in designated areas and *in situ* deposition of metals to contact

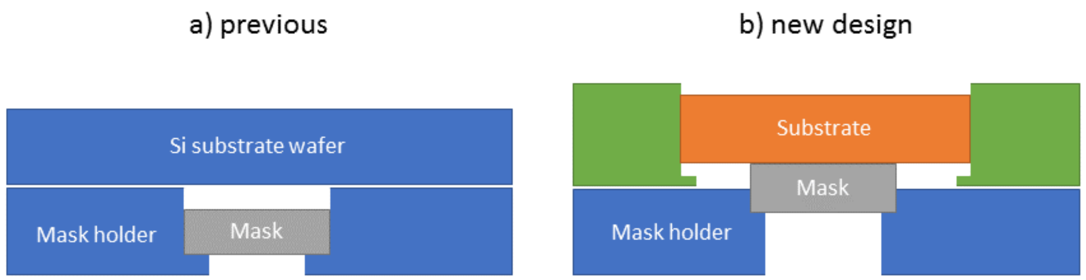

Fig. 6.4: *Comparison of the previous design a) and the new design b) for the mask holder and the sample holder. The mask and the sample are separated by several µm in a), while in the new set up in b) the mask is in close contact to the sample.*

the structures would be possible. Therefore, the next section of this work concentrates on improving the stencil lithography technique.

6.2.2 Holder Design and Transfer

As mentioned in the previous paragraph, the distance between the sample and the stencil in the MBE is the decisive parameter in creating structures with the stencil lithography technique. If the stencil and the sample are too far apart, the structures will blur. This blurring is allegedly less important for Hall bar structures, since the structures are comparably large. In his work, Daniel Rosenbach showed that the structures blurred over several microns, too far for closely positioned patterns, much less sub-micron patterns. Therefore, the distance between sample and mask has to be kept as small as possible. Thus, new holders are designed, to bring the mask and the holder in close contact. In Fig. 6.4 the previous and the newly designed process of stencil lithography are shown. In the old design shown in Fig. 6.4 a), the distance between the mask and the sample is several microns large, since the mask has a thickness of 200 µm in an extrusion 300 µm deep. In the new design on the other hand the sample is positioned deeper in the holder and the mask protrudes from the mask holder, effectively lifting the sample in the sample holder when brought into contact, as illustrated in Fig. 6.4 b). Hence, the distance between the sample and the mask is minimized, supposedly improving the structural resolution of deposited contacts.

To execute the procedure of depositing through a mask, an *in situ* transfer to position the mask under the sample has to be done. This is achieved via a transfer system that utilizes the load lock of the MBE chamber and the manipulator in the MBE chamber. The procedure is shown in Fig. 6.5 a) – e). First, the sample (orange) is put into the sample holder (green) and the desired TI is grown on the sample. The holder is then transferred back to the load lock and positioned over a plate with four protruding screws (Fig. 6.5 a)).

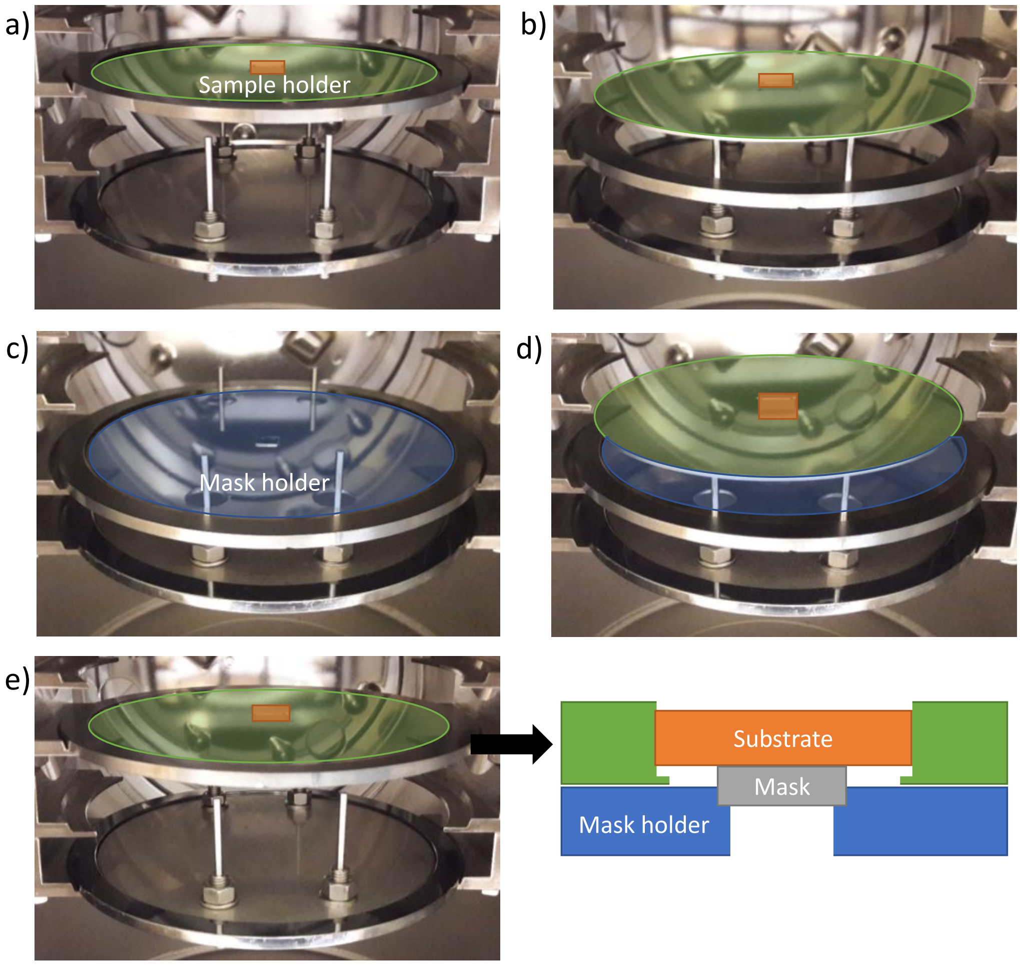

Fig. 6.5: *Transfer procedure for in situ insertion of a mask under a previously grown sample.*

Lowering the sample holder causes it to be lifted from the holder ring (b). The sample holder itself can then be transferred back into the middle chamber of the MBE so that the grown film is not exposed to oxygen.

The load lock is sealed and then opened to the outside. The mask holder (blue) is put into the holder ring, with the mask in the middle of the holder protruding slightly over its frame (c). The mask holder is designed with four holes, through which the four screws of the transfer system are led. The load lock is then closed and pumped down. At base pressure, the seal to the middle chamber is opened and the sample holder is transferred to the load lock. After being lowered onto the screws (d), the holder ring containing the mask holder is lifted up, picking up the sample holder at the top of the screws. Thus, in the holder ring, the mask holder is positioned under the sample holder (e). The opening in the sample holder and the mask are ideally at the same position, small deviations are however considered in the holder design. Therefore, the mask protrudes through the hole in the sample holder and lifts the sample in the sample holder, as illustrated in the diagram. Due to the low positioning of the sample in its extrusion, the sample is still fixated in its slot.

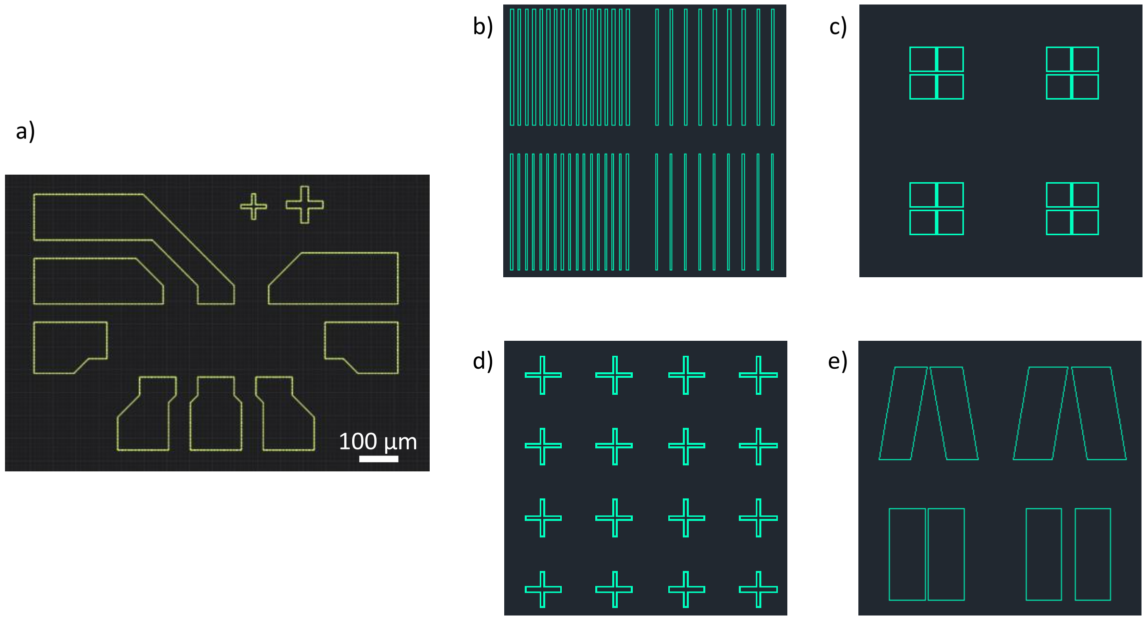

Fig. 6.6: *Examples for patterns etched into the mask. a) shows the conventional contact pad layout of a Hall bar. b) – c) show examples of sub-µm structures for tests. b) lines of varying width and pitch, c) four squares creating a negative cross, d) crosses of different sizes. d) shows contact pads with varying distance and size, down to distances of 100 nm.*

The holder stack can then be moved to the growth chamber to deposit metals. If after the metal deposition a second growth on the full sample is needed, the mask and the sample can be separated by revering the depicted procedure.

The last paragraphs dealt with the design of the holders and the procedure to use the masks in the MBE, however the nature of the masks has not been explicated yet. Therefore, the mask layout and the fabrication process will be detailed in the next section.

6.2.3 Mask Layout and Fabrication Process

In contrast to the earlier approaches with silicon (100) membranes that are patterned with focused ion beam (FIB), a reversed process is chosen. First, a layer of silicon nitride deposited on a Si wafer is structured and then the silicon is etched to reveal a membrane with the patterns inside.

In order to create membranes, a robust material needs to be found, which endures standing freely without support by a substrate underneath and which can be patterned by optical or electron beam lithography to the desired layout. F. J. Hackemüller shows in his master thesis that such membranes, although without patterns, can be achieved by depositing silicon nitride via low pressure chemical vapor deposition on a Si (100) wafer [76]. The silicon nitride covers the wafer on both sides and forms a low strain film on the whole substrate. Hackemüller then proceeds to etch square holes into the silicon nitride on the backside of the wafer to create windows for the removal of the silicon. The latter is performed by anisotropic etching via a potassium dioxide solution (KOH). After etching through the Si, only the silicon nitride membrane is left [76].

Two distinct mask layouts are designed in this work, one for micrometer sized Hall bar structures and one as test for sub-µm structures. In Fig. 6.6 examples of the two structures are shown. The Hall bar layout in Fig. 6.6 a) is taken from the conventional layout for Hall bar fabrication, with Hall bar widths from 20 µm to 60 µm. Two crosses are added in the top right corner for alignment during further processing. For sub-µm structures, several different forms are chosen. In Fig. 6.6 b) stripes are shown, which correspond to the patterns on the prestructured samples shown in Fig. 4.1. The stripes are designed with thicknesses ranging from 100 nm to 2 µm and pitches of the same order. Fig. 6.6 c) and d) show negative and positive crosses. In c), the squares are etched into the nitride, leaving only cross-like bridges of silicon nitride. MBE deposition through the holes then creates square pads of metals on the sample, with a cross void of metal in between. The layout in d) creates the opposite, crosses consisting of metal. By depositing twice with a 90° rotation of the sample between the growths, the creation of a closed metal film on the topological insulator with one or several holes could be possible. In the case of the positive metal crosses, if two crosses overlap, there will necessarily form a hole surrounded by metal if the displacement is large enough. The same is true for the negative crosses. If the metal is replaced with a superconducting material, Majorana fermions created by induced superconductivity are predicted to arise, allowing for compelling experiments proposed by Fu and Kane and others [10, 77]. The patterns in e) are larger than b) to d), since the structures are supposed to be used as contact pads for the prestructured samples of chapter 4.1. By careful alignment, the rectangular patterns can supposedly be positioned over the TI filled stripes and contacts with varying widths and distance could be created. By again replacing the metal with a superconductor and inducing superconductivity into the TI wires in the prestructure, the coupling of possible Majorana modes could be investigated, as shown for InAs by Albrecht *et al.* in [5].

For the creation of the patterned membranes two substrates are available. The first consists of a Si (100) wafer of 525 µm thickness covered with 160 nm silicon oxide and 200 nm silicon nitride. The second consists of 375 µm Si (100), covered only with 100 nm silicon nitride. Both oxide and nitride can be used as an etch stop for the KOH solution, the nitride however is better suited, since the oxide is still etched by the KOH, although much slower. The benefit of an additional layer of oxide might however be an additional support for the nitride membrane. The Hall bar patterns and square etch windows are structured onto the silicon nitride with optical lithography. AZ 5214 E resist is used as described in Tab. 6.1, however the reversal process needs to be executed to only remove the resist where the structures are supposed to be etched into the silicon nitride. After development, the samples are transferred to a reactive ion etching (RIE) chamber. In the low-pressure chamber, a mixture of flouroform (CHF_3) and oxygen is excited by an electromagnetic field and a plasma is generated.

Silicon nitride removal by reactive ion etching		
Step 1	Gas/Flow [sccm]	CHF_3/55 + O_2/5
	RF power [W]	40
	ICP power [W]	100
	Time [s]	5
Step 2	Gas/Flow [sccm]	CHF_3/55 + O_2/5
	RF power [W]	25
	ICP power [W]	100
	Time [s]	240

Tab. 6.2: *Parameters of the reactive ion etching process to remove the silicon nitride to structure the mask patterns. Inductively coupled plasma (ICP) ignited by a radio frequency (RF) electromagnetic field is used to create ions that chemically etch the nitride, accelerated towards the sample by a DC bias voltage.*

AR-P 6200 (CSAR-62) for electron beam lithography		
Dehydration	130 °C for 5 min	
Spin coating	30 s with 4000 rpm	
Softbake	150 °C for 1 min	
E-beam	Beam current	500 pA
	Dose	64 µC/cm^2
	Resolution	5nm
Development	1 min AR 600 – 546 at 0 °C	
RIE	See Tab. 6.2	
Resist lift-off	5 min dip with ultrasound in AR 600 – 71, acetone, isopropanol	
Cleaning	GIGAbatch 5 min, 600 W, 600 sccm O_2	

Tab. 6.3: *Process parameters for the electron beam lithography necessary to fabricate sub-µm structures. The used AR-P 6200 resist is a positive electron beam resist. Before dehydration, the samples are dipped into acetone and isopropanol for 5 min each.*

The ions in the plasma etch the exposed silicon nitride to reveal the Si surface underneath. Detailed information on the RIE etching are listed in Tab. 6.2. First, a short process step with higher power is executed to ignite the plasma, then in the second step with a radio frequency electromagnetic field with less power the nitride is etched. Inductively coupled plasma is utilized to lower the DC bias for ion acceleration, decreasing sputtering and therefore damages to the silicon. The same process is performed on the backside, onto which the square windows used for the KOH etching were patterned. By using alignment markers on the optical lithography mask, the windows on the back of the sample and the structures on the front can be matched, so that the etching reveals the structured areas of the sample. The windows are designed with side lengths of 0.7 mm to 2 mm, in order to allow for membranes with a side length of at least 1 mm, the length of the Hall bar structure.

The sub-µm structures cannot be patterned by optical lithography, since the resolution is not good enough. Therefore, the structures need to be created with electron beam lithography. Thus, the AR-P 6200 (CSAR-62) resist previously used for the fabrication of the prepatterned structures in chapter 4.1 is utilized. The process steps of the patterning with the resist are detailed in Tab. 6.3. First, the samples are cleaned by 5 minute dips into acetone and isopropanol. Subsequently, the resist is coated on top and baked. The sample is then transferred to the electron beam chamber and irradiated. After development with AR 600 – 546 at 0 °C for higher resolution, the samples are transferred to the RIE for removing the silicon nitride. When the nitride is removed, the excess resist is cleaned off with five minute dips into AR 600 – 71, acetone and isopropanol in an ultrasound bassin. Lastly, to clean off burnt remains of resist, the sample is placed into a GIGAbatch for five minutes at 600 W microwave power and 600 sccm O_2, incinerating the resist. Examples for etched structures created with this process are shown in Fig. 6.7.

With both sides of the sample prepared, the next process is the etching of the Si. Since it is essential that the samples are only etched on the side with the square windows, special holders are used. The sample, cut to a 1x1 cm^2 chip, is fixated in a holder with a 7x7 mm^2 window to one side and rubber rings are used to seal the window sides. This prevents the etchant from entering the holder and etching the backside of the sample.

Silicon can be etched by strong alkaline solutions like KOH and TMAH (Tetramethyl-ammoniumhydroxide) with a wide range of rates. The etch rate depends on the concentration and the temperature of the etchant, but the decisive factor is the orientation of the etched silicon surface. The (100) surface is etched, depending on temperature and concentration of the etchant, up to 300 times faster than the (111) surface. This fact is used in the fabrication of the masks. The alkaline KOH solution used in this work for the etching of Si is prepared with a concentration of 22 % and kept at a temperature of 85 °C. With these parameters, the surface exposed in the holder window, exhibiting the (100) facet, etches 160 times faster than the (111) facet. Due to this difference in etch rates, the hole created in the silicon wafer is formed like a truncated pyramid, with an angle from (111) to (100) of 125.3° [78]. The etching scheme is shown in Fig. 6.8 a).

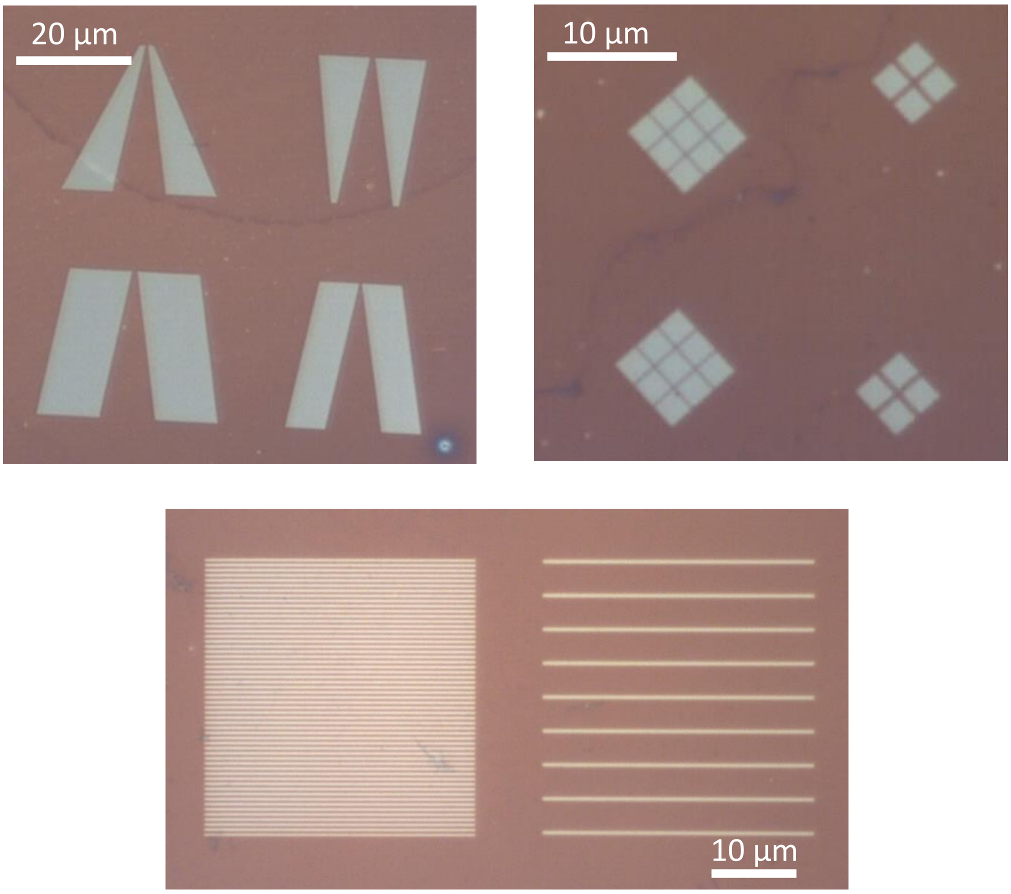

Fig. 6.7: *Silicon nitride patterned with reactive ion etching corresponding to the designs shown in Fig. 6.6 b)- d).*

Since the (111) directions is also etched, only slower, an underetch of the oxide and nitride layers occurs. In between etching steps, the depth of the etched trench is monitored with a profilometer. The latter uses a fine tip to scan the topography of a sample, similar to an atomic force microscope, but on a larger scale. Scan examples are shown in Fig. 6.8 b), after 185 minutes (blue), 275 minutes (orange) and 465 minutes (grey) for a 525 µm Si sample. Measuring the depth allows for calculating the etching rate, which amounts to roughly (1 ± 0.2) µm per minute. The etching rate varies heavily with the temperature, which supposedly is kept constant by the heating plate and the included thermometer. However, observing the temperature of the plate showed that it fluctuated between 75 °C and 85 °C, lowering the etch rate. The samples with thick silicon and additional silicon oxide, for stress release as mentioned in chapter 4.1, show very rough etching edges, illustrated by the curve after 465 min in Fig. 6.8 b). Moreover, the fabricated membrane on the thick Si substrates is larger than expected by calculating the width of the membrane with the Si (111) to (100) angle. Experiments by Hackemüller on samples without the oxide do not show this behavior, suggesting that the oxide at the etch windows is also removed by the alkaline solution [76].

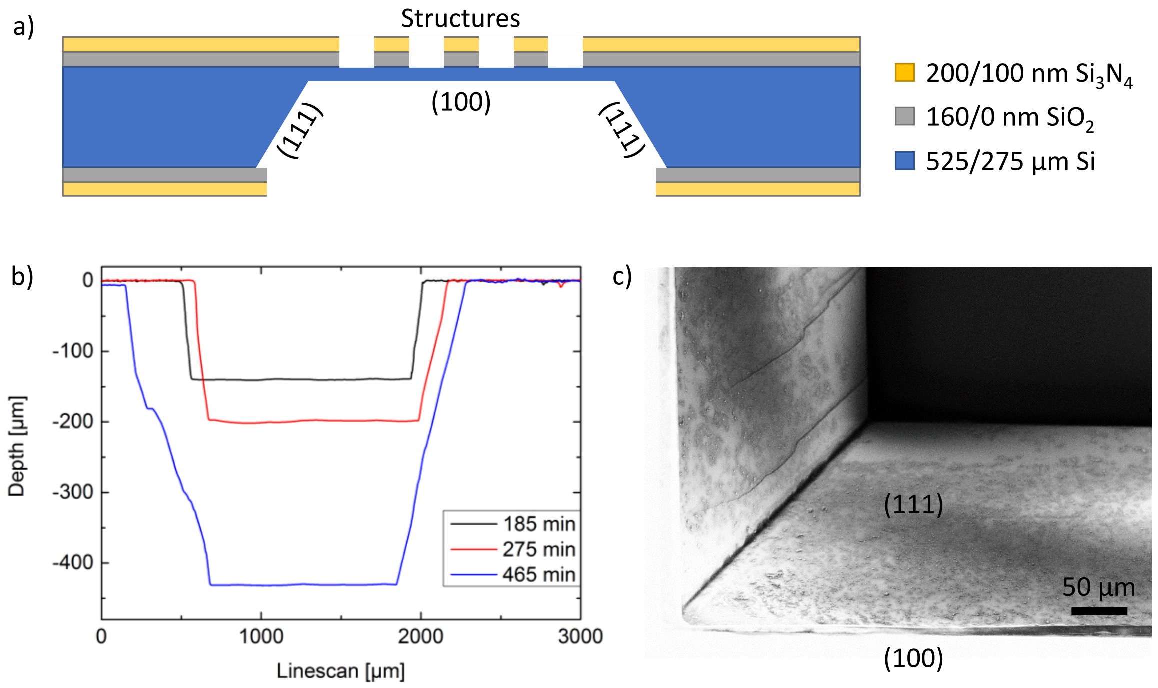

Fig. 6.8: *a) shows the schema of etching the Si down onto the patterned membrane. The Si is etched faster into the (100) direction, creating a trapezoid etch profile. The progress of the etching is checked with a profilometer, measuring the depth of the hole in the Si as shown in b). The position of the hole is shifted due to varying starting locations on the sample and not due to a feature of the etch process. The SEM micrograph in c) shows the corner of an etched trapezoid with the fabricated membrane in the black background of the picture.*

This enlarges the size of the etch window, resulting in larger, and therefore less stable, membranes. The gradual removal of the oxide can explain the existence of the steps in the pyramids side walls, indicated by the step at roughly 500 µm in the 465 min curve. Thus, only the samples with 100 nm Si_3N_4 on 275 µm Si are used for further mask fabrication. One corner of an etched window on such a sample is shown in Fig. 6.8 c), where the truncated pyramid like etch profile is clearly visible. The sides of the etch are smooth and steep, a light underetch can be observed at the bottom of the figure due to the thin protruding nitride. Additionally, the thinner substrate reduces the etching time from an average of eight hours down to four hours. However, the stability of the membrane is reduced due to the thinner nitride.

To counter the lower stability of the thinner nitride, the etching procedure is changed. First the bulk of the wafer is etched with KOH as illustrated before until only roughly 10 µm of Si are left. The sample is then taken out of the holder and transferred into a solution of 25 % TMAH at 80 °C. TMAH has a higher selectivity to both silicon nitride and oxide, so that the nitride is a more efficient etch stop, as well as a lower etch rate, which allows for higher precision for stopping the etching process. Taking the sample out of the holder for one sided etching results in the removal of silicon in the etch window as well as under the

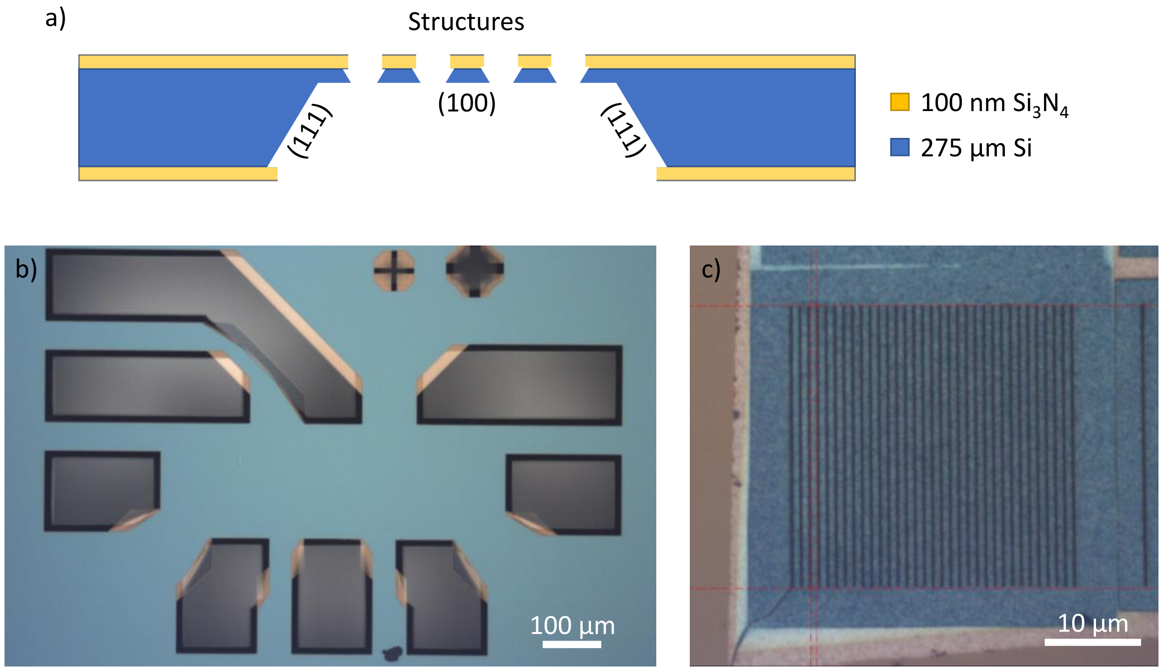

Fig. 6.9: *a) Schema of the improved etching process. The Si (100) is first etched until only roughly 10 µm of Si are left, then the sample is dipped completely into the base to etch from both sides, creating the double-trapezoid etch profile. The optical micrograph in b) shows a Hall bar pattern fabricated by this technique, with silicon reinforced nitride in blue and free-standing nitride in yellow. c) shows an example of the sub-µm mask. Free-standing nitride is shown in blue, reinforced nitride in yellow. The structures are not reinforced, due to their size, only the surrounding nitride.*

structures. The silicon is therefore etched from both sides, creating an hourglass like etch profile, shown in Fig. 6.9 a). As indicated in a), a thin layer of Si is left on the silicon nitride membrane. This increases the stability of the membrane greatly. In Fig. 6.9 b) and c) examples of the membranes fabricated this way are shown. The Hall bar layout in b) exhibits yellow and black areas apart from the bright blue silicon nitride and the grey areas, which are the holes in the wafer. The yellow areas are underetched and consist solely of nitride, while the black frames of the holes are the (111) facet created by the etching from the top side. In c), one panel of the stripe structures is shown. The underetching of the nitride in these patterns is visible at the edges of the blue nitride membrane in yellowish colors. In the bottom left corner, a rupture in the nitride can be identified. In fact, most of the sub-µm structures are destroyed during the etching, while the larger Hall bar structures can reproducibly be fabricated as shown in Fig. 6.9 b). With this finding, the optimization of the sub-µm mask fabrication is postponed and the successfully created Hall bar structures are used to fabricate *in situ* devices for the transport measurements in chapter 7. However, the successful fabrication of masks with sub-µm patterns is possible as shown in Fig. 6.9 c) and could be achieved by having wider spaces between the structures for more stability in the nitride. What is left is to show is that growths through the mask can be performed. Therefore, depositions and Hall bar fabrications are shown in the next section.

6.2.4 Results

In order to test the masks created in the previous section, pure aluminum depositions are firstly performed to test the stability and the reusability of the membranes. Therefore, the aluminum cell is heated to 1200 °C and aluminum is evaporated through the mask in the mask holder onto a pristine silicon sample at room temperature. In Fig. 6.10, the results of the Al growth are demonstrated with examples for each of the different patterns on the mask. Fig. 6.10 a) – d) show fabricated line patterns, see Fig. 6.6 b), Fig. 6.7 c) and Fig. 6.9 c). a) and b) illustrate a pattern with a designed line width of 300 nm and a pitch, the distance from a point in the line to the same point in the next line, of 2 µm. The detailed view of a) in b) reveals the formation of large aluminum crystallites in the middle of the line and decreasing crystallite size towards the edge of the structure. Comparing the width of the wire to the designed width, it becomes clear that the deposited structure is wider than the intended 300 nm. Measuring the edge to edge distance indicated by the arrow in Fig. 6.10 b) reveals a width of approximately 700 nm. Therefore, the pattern distends 200 nm to both sides. This enlargement, or blurring, to the sides can be caused by the diffusion of the material on the sample and by the distance of the mask to the sample. However, the diffusion is suppressed due to growing at lower temperatures, decreasing the kinetic energy of the deposited material. Thus, the distance from mask to sample is the determining factor. Unfortunately, it cannot easily be further decreased, since the sample is already laying on top of the mask. Pressure could be used to bring the two components closer to each other, which however is not realizable in the setup. The blurring is observable in all grown structures. Fig. 6.10 c) shows a line pattern with a designed width of 200 nm and a pitch of 1 µm, resulting in a pattern width of 650 nm and a distance between lines of 300 nm instead of 800 nm shown in d). In Fig. 6.10 e) an example of the contact deposition is shown. In the initial CAD design, the distance between the tips of the contact pads decreases down to 500 nm. However, due to the blurring, the two tips touch, although only hardly.

This suggests, that the enlargement by blurring to both sides is constantly of the order of 200 nm to 250 nm, independent of the grown pattern. In Fig. 6.10 g) and in the magnified h), the effect of the blurring on narrowly designed structures becomes evident. The structure consisting of multiple crosses with a designed width of 200 nm is supposed to create separate squares with a side length of 2 µm. However, due to the blurring, the space between the squares is, although less thickly, covered completely in aluminum.

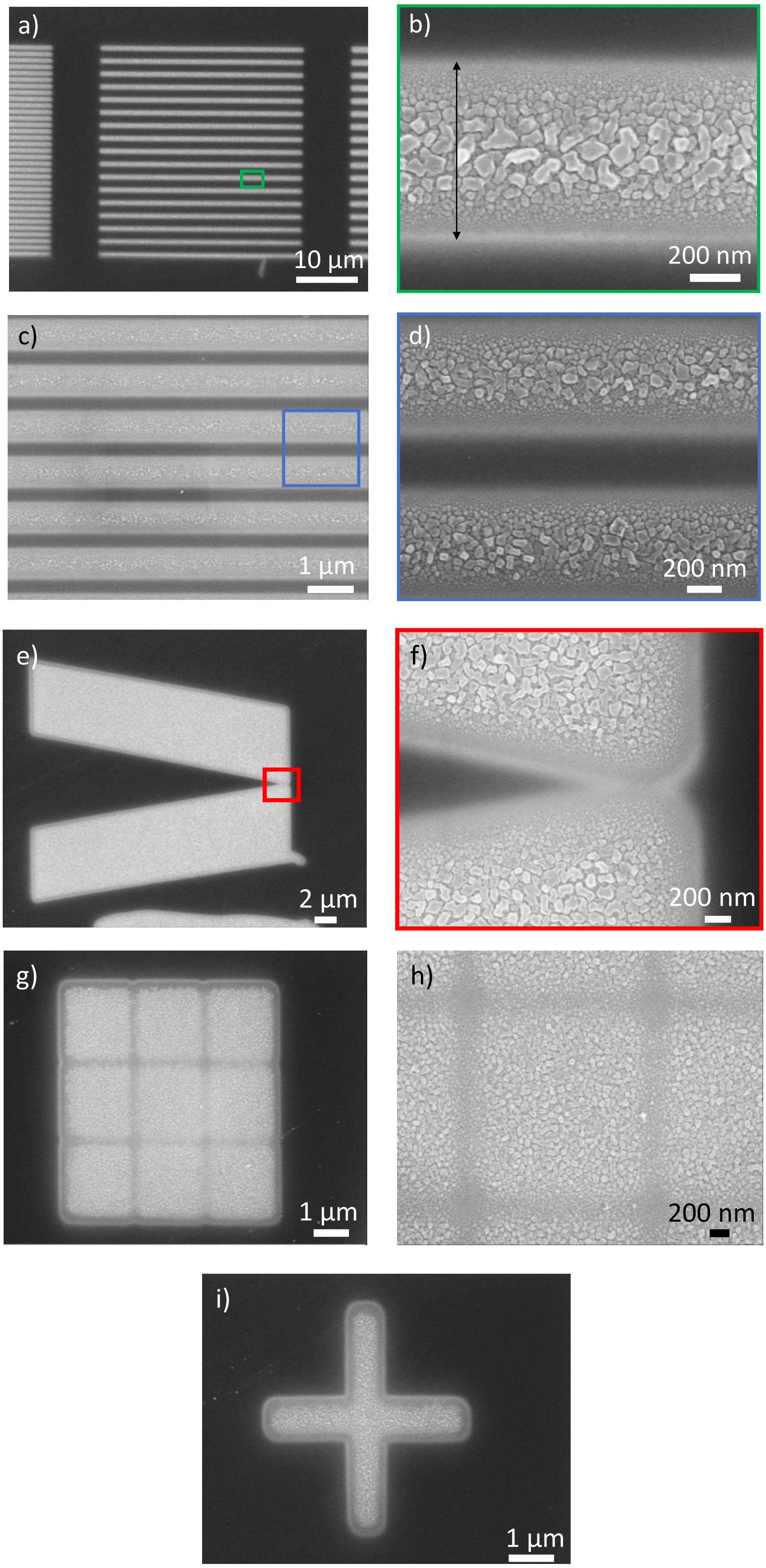

Fig. 6.10: *SEM micrographs of aluminum depositions through the sub-µm structure mask on pristine silicon.*

By changing the design to squares not 200 nm, but 400 nm apart, it should be possible to realize the holes in the superconductor needed for the experiment proposed by Fu and Kane [10]. The lines between the squares would still be covered with Al, since the blurring of 200 nm would cover the 400 nm line width, the crosses however would not be covered completely, since the diagonal distance amounts to 560 nm. Lastly, in Fig. 6.10 i), a deposited cross is shown. In the initial design, the width of on arm of the cross is 500 nm, the SEM image however provides a width of roughly 950 nm, complying with the order of blur of the other structures.

Fig. 6.10 shows that depositions through the mask are possible and create a mirrored image of the structures on the sample. Small features like ruptures that are created during the etching process are translated onto the sample, for example a rupture on the corner bottom right of the contact pad layout in the mask for Fig. 6.10 e) is copied onto the sample perfectly. However, the size of the structures changes due to the blurring and diffusion of the material. This enlargement ranges constantly between 200 nm and 250 nm for all structures on the sub-µm patterned mask. Increasing the growth time and therefore the thickness of the Al film could however lead to larger diffusion. Therefore, to successfully create sub-µm sized patterns, the widening of the structures on the sample has to be considered in the design by narrowing the structures and enlarging the spacing between them.

Since the blurring in the sub-µm pattern growth tests are consistently lower than 1 µm, the growth of structures on the order of several micrometers is supposedly not influenced as much as the sub-µm structure. To test this assumption, growth tests are also performed with the Hall bar structure mask. The results of the tests are shown in Fig. 6.11. In the SEM micrograph in Fig. 6.11 a) the deposited Hall bar pattern is illustrated, which is a mirrored image of the mask shown in b). The contact pattern is translated onto the Si surface accurately, without visible enlargement of the structures. Magnifying the edge of the structure marked in a) indicates a sharp edge of the aluminum to the Si surface. On the left part, the undulating surface of the thick aluminum is visible, while on the right part, the dark grey of the silicon surface is shown, separated by a line of brighter grey. Further magnification in d) reveals the transition of the aluminum film from a wavy structure (see also Fig. 4.5 a) and b)) to a flat and only faintly distinguishable layer, until it completely disappears over a distance of 200 – 300 nm, consistent with the previous findings. In comparison with the earlier attempts of Rosenbach and Schüffelgen, the blurring is decreased greatly, from several µm to less than 1 µm [72, 75]. Thus, it is confirmed that the *in situ* fabrication of metal contacts for Hall bars via the previously explained transfer is possible and produces contact pads which are not connected, necessary for transport measurements.

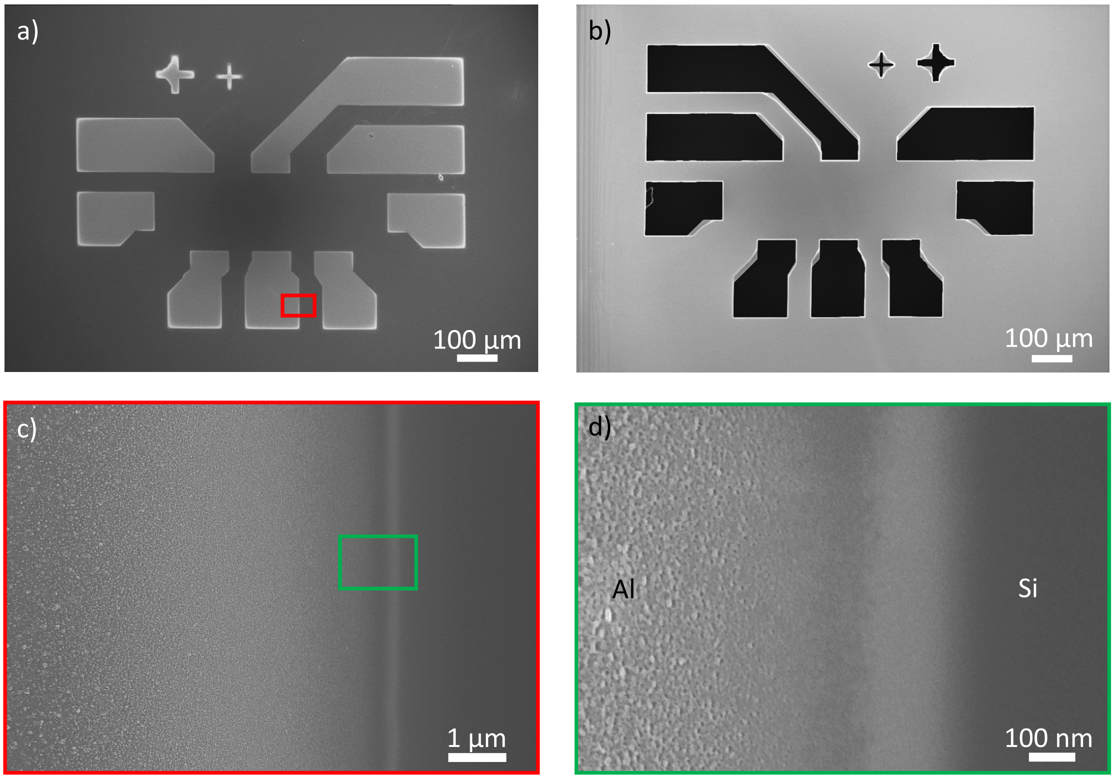

Fig. 6.11: *Al deposition through the Hall bar mask. The SEM micrograph a) shows the grown aluminum contact pads, fabricated with the mask shown in b). Since the mask rests immediately on the sample, the structures are mirrored. In c), the area marked with a red rectangle in a) is enlarged. The edge of the pads is further magnified in d), illustrating the area in c) marked with the green rectangle.*

For the characterization of the quaternary topological insulator introduced in chapter 5, the developed mask technique is used to fabricate a Hall bar with top gate. To do so, first an 18 nm layer of quaternary topological insulator is grown on the silicon wafer with the parameters elaborated in chapter 5.2. The thickness of the TI is estimated by applying the growth rate of a separated test sample with the same growth parameters. The sample is then transferred to the load lock and the positioning of the Hall bar mask is executed as previously described. First, a thick layer of titanium is deposited through the mask onto the sample. In contrast to the previously deposited thin Ti diffusion barrier with a thickness of roughly 3 to 4 nm deposited in one hour, the growth time is increased 16 hours to form a thick diffusion barrier, which should not be penetrable by the aluminum that is subsequently evaporated on the sample. After the aluminum deposition through the mask, it is removed with the transfer system, and a thin layer of approximately 2 nm of Al is deposited on the whole sample. This thin layer is used as a capping layer for the Hall bar. Though the Al may form an insulating layer within the TI as explained previously in this chapter, this only affects the topmost layers of the TI and as shown by Lang *et al.* does not hinder the topological transport through the surface states [70, 71].

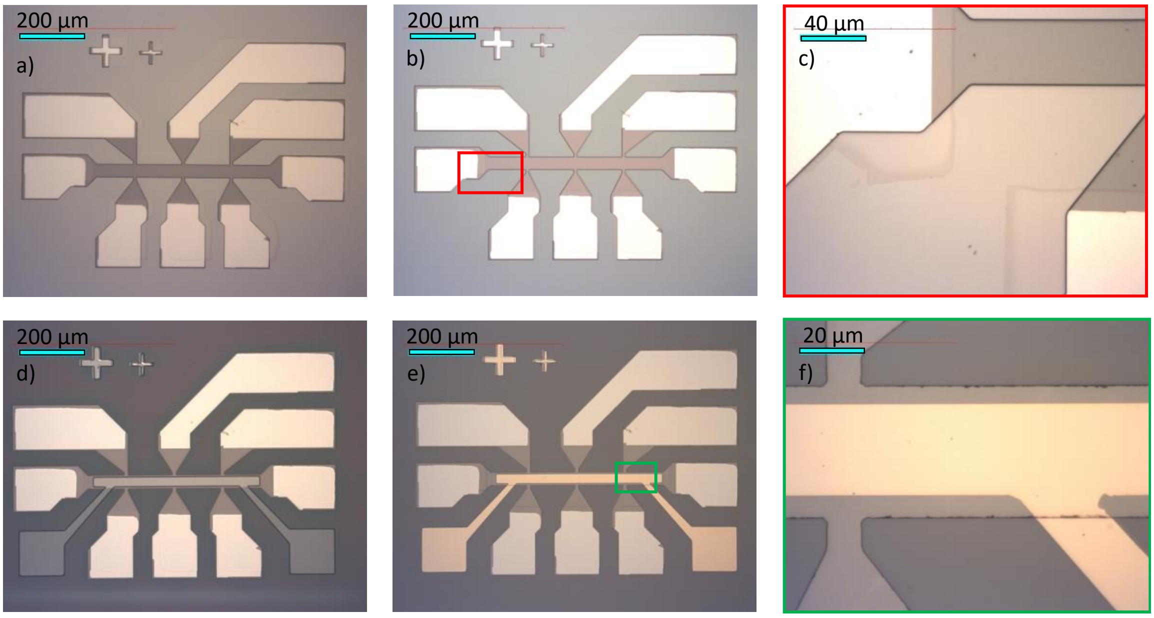

Fig. 6.12: *Optical micrographs of the continuative fabrication of the Hall bar after in situ contact deposition. a) Contact and Hall bar protection with resist (dark grey). b) and c) After removal of excess TI in the vicinity of the Hall bar via IBE. d) Resist patterning for top gate deposition. e) and f) Finished Hall bar with titanium/gold top gate.*

The formation of the insulating TI-Al layer is only problematic at the interface of the TI and contact, since at this point, a current is flowing into the TI and the existence of an insulating layer would negatively influence the transport behavior. Due to the Ti diffusion barrier, this is supposedly not the case. After the capping deposition, the sample is taken out of the MBE chamber and the excess topological insulator surrounding the Hall bar needs to be removed. Therefore, AZ 5214 E resist is patterned as shown in Fig. 6.12 a) to protect the contacts as well as the area of the TI, which will form the Hall bar. In the optical micrographs, the bright areas covered with the resist are the *in situ* deposited contacts.

The removal of the excess TI is achieved with ion beam etching (IBE). In the IBE chamber, argon ions are accelerated towards the sample. The high energy electrons proceed to mill the parts of the sample not protected by the resist down to the silicon surface. The results of the IBE milling are shown in Fig. 6.12 b) and c). In c), the area between the contacts shown in b) is magnified, revealing misaligned structures next to the bright contact pads. These patterns can occur due to the positioning of the Al and Ti evaporation cells in the MBE chamber. The cells are stationed with a 90° angle between them, which is roughly compensated by turning the sample after the titanium deposition, in order to align the sample to the Al cell. This cannot be done precisely enough by eye to fully erase the displacement though. However, the shown displacement is too large to originate just from the differing directions, suggesting that the mask moved when the sample was aligned with the Al cell. There is always some play provided to consider the dilation of the holders, which also allows the samples to move slightly. Thus, during movements of the holder stack, the mask can shift with respect to the sample, leading to deviating patterns. However, the majority of the pads overlap and no contact is established between different pads, so that the functionality of the contacts is maintained.

To fully characterize the Hall bar, a top gate is also applied to shift the Fermi level in the investigated film. Therefore, a dielectric needs to be applied to the Hall bar in order to avoid direct conduction from the top gate to the bar. Hafnium dioxide (HfO_2) is an established dielectric material and thus deposited on the whole sample conformally with a thickness of 10 nm via atomic layer deposition. On the dielectric, the gate is patterned into AZ 5214 E resist as shown in Fig. 6.12 d). With an UNIVEX 400 box-coating system, 10 nm of titanium as an adhesive and 100 nm of gold are deposited on the sample. Via a lift-off process with an acetone and isopropanol dip, each for five minutes, the resist is removed and excess Ti/Au covering the resist is taken away, leaving only the filled pattern. The results of the deposition are shown in Fig. 6.12 e) and f), illustrating the Hall bar covered with a stripe of gold, the top gate, linked to two golden contact pads. The magnified optical micrograph in f) exhibits the smoothness of the deposited gold and the transition off the TI Hall bar onto the HfO_2.

The full view presented in Fig. 6.12 e) shows the final result of this chapter, a Hall bar consisting of the quaternary TI developed in chapter 5 deposited on silicon, equipped with *in situ* added titanium/aluminum contact pads grown via stencil lithography and *in situ* capped with a thin layer of aluminum. The *in situ* contacts should provide high quality interfaces, without Al diffusion into the TI due to the thick Ti layer, while the AlO_x cap of the bar itself protects the surface states from environmental contaminations. The whole sample is then capped again with 10 nm of HfO_2 as a dielectric and completed with a top gate consisting of 10 nm Ti and 100 nm Au.

In this chapter it was shown, that by using silicon nitride stencil lithography masks, it is possible to fabricate arbitrary patterns of metals in an MBE. The mask structures were created with electron beam lithography and RIE, before etching the silicon down to the patterned membrane. Employing the holders designed in this chapter, the metal patterns can be *in situ* deposited on top of TI films. The resolution of this fabrication process can be estimated to roughly 200 nm, which is a great improvement, compared to several micrometers in previous works [72, 75]. This allows for the creation of sub-µm sized structures. However, due to shifting of the mask or sample, deviations in succeeding growths can occur. To finally confirm, that stencil lithography is suitable for the *in situ* fabrication of devices, the sample will be used for transport measurements, which are further explicated in the next chapter.

7 Transport Measurements

By measuring the electrical transport through the sample illustrated in Fig. 6.12 d), several characteristic values of the topological insulator can be determined. These include the carrier density n, the mobility μ and the temperature dependent phase coherence length l_φ, by which the TI can be compared to other TIs like the ternary or binary compounds. To do so, the samples need to be cooled to low temperatures and strong magnetic fields need to be applied. Therefore, the cryostat setups of the PGI-9 are used. These will be described in the next section, before proceeding with the evaluation of the measured data.

7.1 The VTI Cryostat and Measurement Setup

The measurements executed for this work are performed in a variable temperature insert (VTI) cryostat. The cryostat consists of two interleaved vacuum chambers, containing two separated chambers filled with liquidized helium (^{4}He) at a temperature of 4.2 K, as shown in Fig. 7.1. Due to the evacuated outer chamber, the helium is isolated from the surrounding temperature. The outer chamber contains a superconducting magnet cooled by the liquidized He, which can reach a magnetic field of up to 14 T perpendicular to the sample plain. The inner vacuum chamber separates the magnet chamber from the inner chamber, containing the sample, held by a sample rod, which can be inserted into the cryostat from the top. The two chambers are connected by a thin pipe, isolated by a needle valve. By providing a low pressure in the sample chamber, created with a vacuum pump, the helium entering the sample chamber from the He bath in the outer chamber is evaporated, leading to a further decrease in temperature down to 1.4 K.

The Hall bar is mounted in a chip carrier and connected to the leads of the carrier by aluminum wires. The wires were applied with a wedge bonder. The chip carrier is then put into the sample rod and inserted into the He bath in the sample chamber. There, it is cooled down to 1.4 K, however the temperature can be varied with an incorporated heater. A matrix box is connected to the end of the rod, by which the contacts on the Hall bar can be addressed. The measurement setup and wiring is shown in Fig. 7.2, where a four-terminal measurement of the Hall bar is illustrated. A current is applied to the Hall bar at the two contacts opposite of each other at the ends of the structure (orange), and sets of two contacts are applied for four-terminal sensing (green). In Fig. 7.2, this is done in order to measure $R_{xx,4p}$, with xx specifying the direction of the measurement, parallel to the Hall bar. The current utilized in the following experiments is a sinusodial 1 V amplitude voltage with a frequency of 17.3 Hz generated by a lock-in amplifier, which is

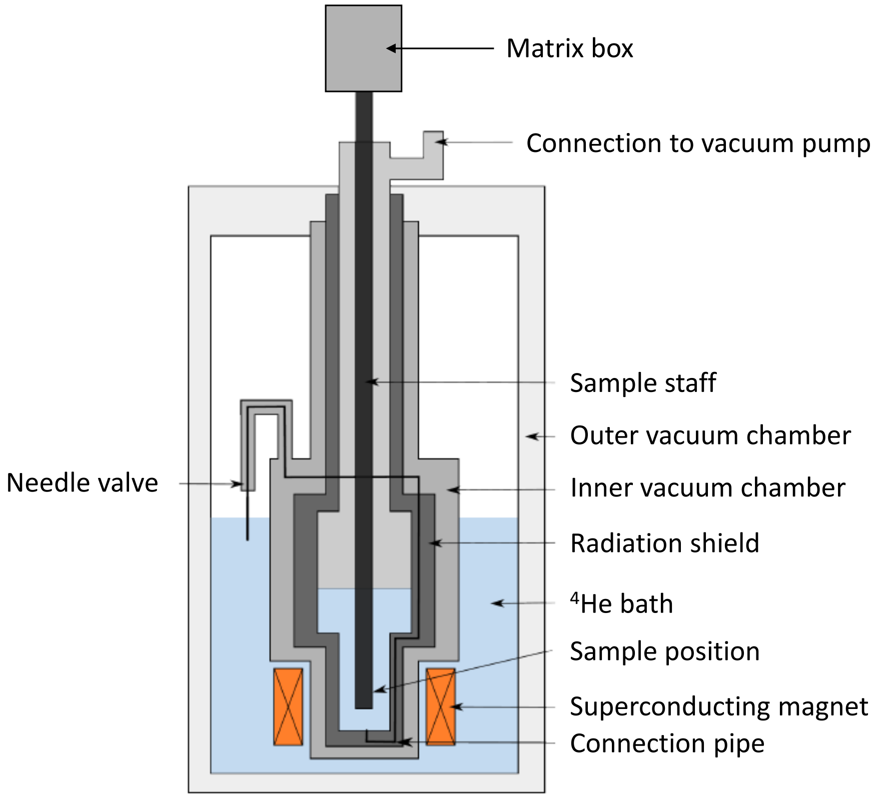

***Fig. 7.1**: Intersection of the variable temperature insert (VTI) cryostat used for the transport measurements in this work. Important parts are labeled, the liquidized helium used for cooling is shown in blue. Adapted from [35].*

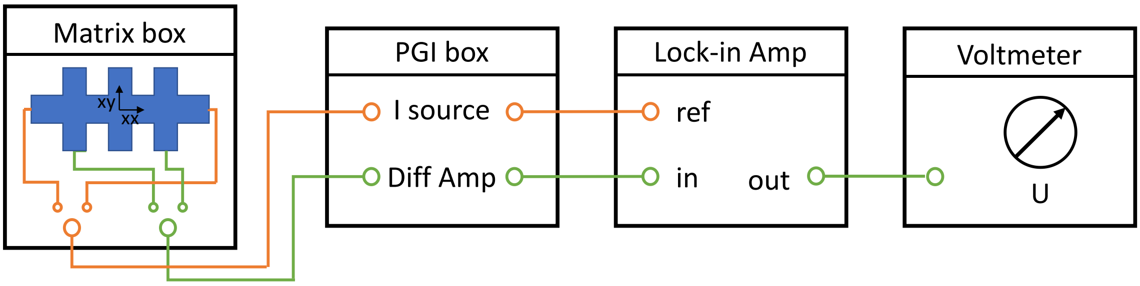

***Fig. 7.2:** Diagram of the measurement setup employed for investigating the Hall bar sample. Orange implies the course of the current, green the measured voltage at different points of the sample. The four-terminal measurement of the $U_{xx,4p}$ voltage is exemplified in the figure.*

translated with 10 µA/V by a PGI-box into a 10 µA amplitude AC current. The signal measured by the four terminal contacts is picked up by the differential amplifier (Diff Amp) of the PGI-box, where it is magnified by a gain factor of 1 to 1000, depending on the measured value. The amplified signal is measured by the lock-in amplifier (Lock-in Amp).

The lock-in is used to filter the noise present in the measurement, by multiplying the reference signal of 17.3 Hz with the measured signal. The result is integrated by a low-pass filter over an integrating time of 1 second, cancelling out all frequencies in the signal unequal to the reference signal, therefore attenuating the noise close to zero. After this process, a DC signal of the sinusodial voltage at the given frequency remains. Lastly, the DC signal is picked up by a voltmeter that is read out by a computer.

In the next section, the results measured with the depicted setup are presented.

7.2 Characterization of the Quaternary *in situ* Hall Bar

The sample examined in the following section is shown in Fig. 6.12. The 40 µm by 600 µm Hall bar consisting of 18 nm (1.4, 1.8) quaternary TI grown on Si (111) is covered with a 3 nm AlO_x capping and 10 nm of HfO_2 as a gate dielectric. On top, 10 nm of Ti and 100 nm Au are deposited as a gate. To characterize the sample, firstly the sheet resistance $R_\square$ and secondly the two-dimensional charge carrier density n_{2D} will be determined. Both values are then used to calculate the mobility µ of the charge carriers in the sample. The mobility denotes the relationship between the drift velocity of the charge carrier and an applied electric field and is proportional to the average scattering time, the time a charge carrier moves without scattering. In solids, the mobility is restricted by defects and impurities in the crystal. Therefore, a high mobility corresponds to a high quality crystal. Lastly, the phase coherence length will be determined. The initial measurement however will be the investigation of the sheet resistance $R_\square$ during cool down of the sample.

For the first experiment, the sample is put into the liquid helium bath and cooled down from room temperature to 1.5 K. The measurement of the longitudinal resistance is performed with a four-point setup ($R_{xx,4p}$). To calculate the sheet resistance $R_\square$ shown in Fig. 7.3, the measured $R_{xx,4p}$ four-point resistance is linked with the dimensions of the Hall bar by

$$R_\square = R_{xx,4p} \cdot \frac{bar\ width}{contact\ distance} \tag{7.I}$$

The bar width amounts to 40 µm, the contact separation to roughly 300 µm for the $R_{xx,4p}$ measurement. Fig. 7.3 shows that the resistance of the sample increases with decreasing temperature, however slightly saturating at low temperature. This finding indicates an insulating behavior, which matches the ARPES data of Fig. 5.6. In the latter figure, the Fermi level is situated in the band gap, cutting the topological surface states about 150 – 200 meV above the Dirac point. If the Fermi level is located in the band gap, the material is either an insulator or a semiconductor, depending on the gap size. In a normal insulator or semiconductor, the resistance increases monotonously with decreasing temperature,

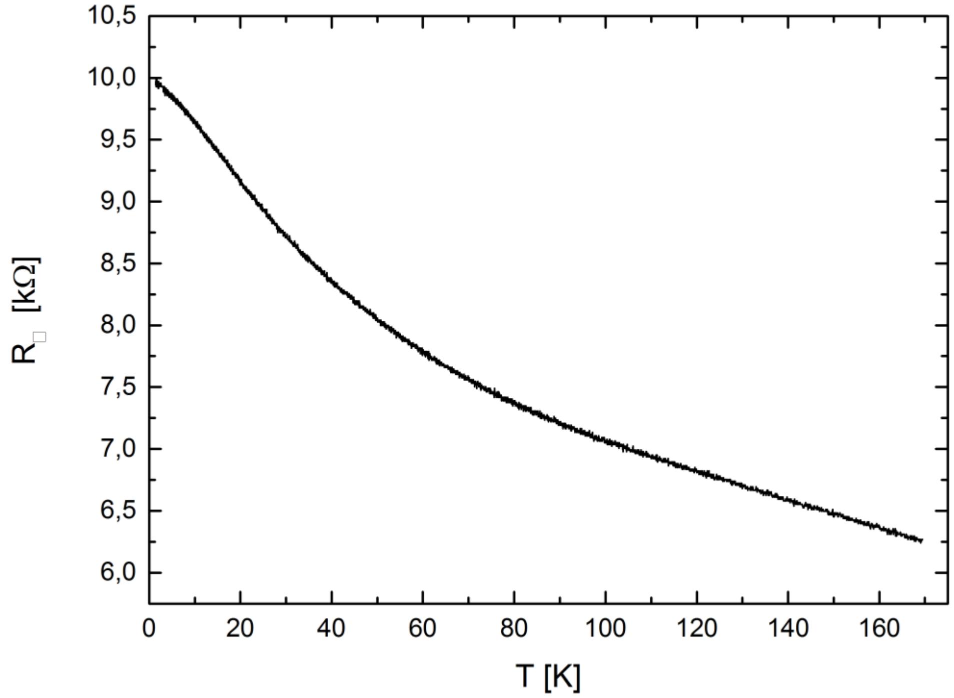

Fig. 7.3: *Cooldown curve of the resistance measured by four-terminal sensing across the Hall bar, thus in the direction of the current. The behavior is that of an insulator.*

however in Fig. 7.3 the resistance saturates at low temperatures, indicating an additional metallic behavior, which is presumably mediated by the surface states. The results of the cooldown curve are similar to the results by Ren, Weyrich, Pan and Zhang in ternary compounds, who also observe an insulating behavior of their films, which have the Fermi level in the band gap [53, 54, 61, 79]. They also measure high sheet resistances of the order of kΩ and a saturation at low temperatures, indicating surface transport.

In the next measurement, the current is swept from 0 µA to 12 µA, in order to measure the four-terminal resistance of the Hall bar. Moreover, the two-terminal resistance between the contacts where the current is applied is detected. The difference between the four- and the two-terminal resistance quantifies the contact resistance, the resistance arising at the interface between the contacts and leads and the TI film. By fitting a linear slope to the data in Fig. 7.4, the slope can be identified, which due to Ohm's law is the resistance. The two-terminal resistance $R_{xx,2p}$ measured between the current leads amounts to 20.6 kΩ, the four-terminal resistance $R_{xx,4p}$ equals 7.5 kΩ, resulting in a contact resistance of R_C = 6.6 kΩ for each of the two current contacts applied to the sample.

To determine the charge carrier density in the sample, Hall measurements are performed. As briefly explained in chapter 6.2.1, by applying a magnetic field perpendicular to the Hall bar plane, a voltage is created due to the Lorentz force, which affects moving electrons or

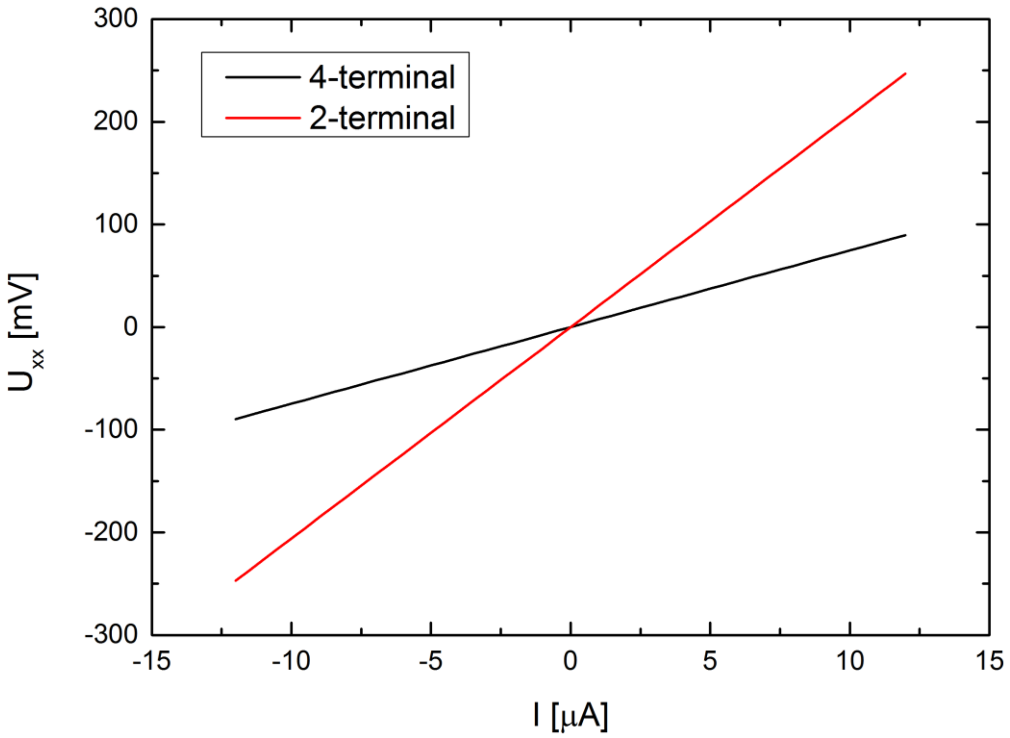

Fig. 7.4: *Four- and two-terminally measured voltages with variable current to determine the sheet resistance at 1.5 K and no magnetic field. The difference in slope denotes the contact resistance.*

holes in the film, corresponding to:

$$\vec{F_L} = q \cdot (\vec{v} \times \vec{B}) \tag{7.II}$$

In the equation (7.II), F_L describes the Lorentzian force, q the charge of the carriers, in this case the charge e of an electron, v the velocity of the charge carriers and B the perpendicular magnetic field. The Lorentz force deflects the charge carriers in the sample to opposite edges of the sample, effectively creating a charge separation. The arising Hall voltage U_{xy}, and therefore the Hall resistance R_{xy}, is measured similarly to the sheet resistance $R_{xx,4p}$ with a four-terminal measurement. During the measurement, the current and temperature is kept constant, while the perpendicular magnetic field is swept from - 10 T to 10 T. The result of the measurement is shown in Fig. 7.5. In order to eliminate possible superposition of signals symmetric to 0 T, distorting the fit, the data is anti-symmetrized.

By determining the slope of the Hall characteristic, the two-dimensional charge carrier concentration can be calculated. To do so, equation (7.II) is applied to the setup of the Hall bar, and can be converted to a one-dimensional form. Therefore, the magnetic field's direction is fixed to be the z direction in a cartesian coordinate system, while the current velocity is only unequal to 0 in the x direction.

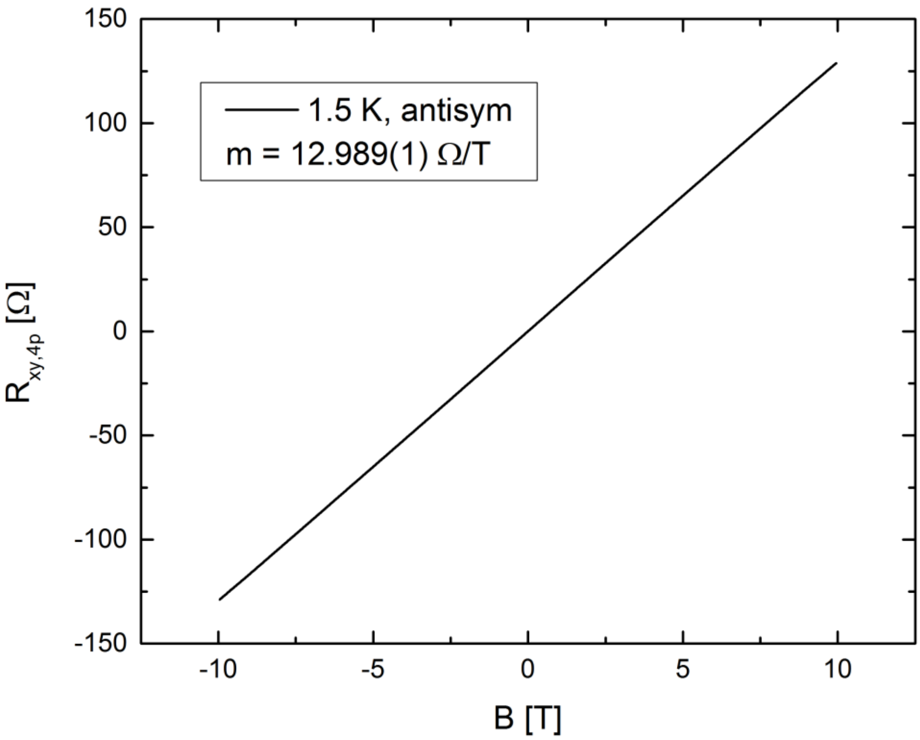

***Fig. 7.5:** Data of the Hall resistance $R_{xy,4p}$ measurement at 1.5 K with magnetic fields sweeps from -10 T to 10 T. A linear fit to the curve results in the slope given in the legend.*

The vector product thus simplifies to:

$$F_{L,y} = -q \cdot v_x \cdot B_z \tag{7.III}$$

Combining (7.III) with $F = q \cdot E$ and $E = U/d$, where E is the electric field, d is the distance of two plates of a capacitor and U denotes the voltage (in this case the Hall voltage), results in:

$$U_H = -d \cdot v_x \cdot B_z \tag{7.IV}$$

Including the current density $j_x = \frac{I}{b \cdot d} = nqv_x$, with n the three-dimensional charge carrier density, and Ohm's law $U = R \cdot I$, (7.IV) can be rewritten as:

$$R_H = R_{xy} = \frac{U_H}{I} = -\frac{1}{nqb} B_z = \frac{1}{e \cdot n_{2D}} B_z \tag{7.V}$$

The last transformation includes $q = -e$ and $n_{2D} = n_{3D} \cdot b$, where b is the thickness of the film. The latter transformation from the two- to the three-dimensional charge carrier density can be performed, since the investigated TI consists of 3 nm high unit cells made out of 3 quintuple layers. As each quintuple layer is supposedly conductive on its surface only and roughly 1 nm high, dividing by the height of the film results in the charge carrier density of one quintuple layer's surface. Comparing equation (7.V) with the slope of the linear curve in Fig. 7.5, it becomes clear that the slope m is equal to the fraction in (7.V), thus:

$$m = \frac{dR_{xy}}{dB_z} = \frac{1}{e \cdot n_{2D}} \Leftrightarrow n_{2D} = \frac{1}{e \cdot m} \tag{7.VI}$$

Thereby, the two-dimensional charge carrier density can be determined by fitting a linear curve to the data in Fig. 7.4. The slope of the fit, $m = 12.989\ \Omega/\mathrm{T}$, results in a two-dimensional charge carrier density of $n_{2D} = 4.81 \cdot 10^{13}\ \mathrm{cm}^{-2}$ at 1.5 K.

With the previously determined sheet resistance and the two-dimensional charge carrier density, the mobility of the charge carriers can be calculated via:

$$\mu = \frac{1}{R_{\square} \cdot e \cdot n_{2D}} \tag{7.VII}$$

Using the data determined at 1.5 K results in a mobility of $\mu = 143\ \mathrm{cm}^2\mathrm{V}^{-1}\mathrm{s}^{-1}$. The calculated carrier density and the mobility compare well with values determined by Snelder *et al.* and Lee *et al.* on exfoliated samples [60, 80].

Measuring the $R_{xx,4p}$ resistance while swiping the magnetic field reveals weak antilocalization effects. To understand weak antilocalization, weak localization (WL) should be explained first. It describes a quantum mechanical effect in disordered systems that arises due to interference of closed electron paths in the system at low temperatures. Closed electron paths occur due to elastic scattering in the film. However, it is important that the scattering lengths and therefore the circumference of the closed loop is smaller than the phase coherence length l_φ. If the latter is given, the counter- and the clockwise path the electron, more precisely the electron particle wave, can interfere constructively, as long as the magnetic field is zero. The constructive interference of the closed loop is independent of loop size and leads to a higher return probability, thus to a higher resistance. The weak localization therefore acts as a positive correction to the resistance of the sample. If the magnetic field is increased, the electron wave accumulates a phase while moving along the loop, which is different for every loop size. This is because the phase difference depends on the magnetic flux penetrating the loop. Thereby, the constructive interference is nullified on average. [6]

In contrast to the increasing resistance in weak localization, the resistance is lowered in weak antilocalization (WAL). Weak antilocalization is an effect involving the spin of the electron propagating in a closed loop. Due to various physical effects like Rashba spin-orbit coupling, spin scattering or a spin locked momentum, as in the investigated TI, the spin rotates while the electron travels through the loop. Therefore, this spin change depends on the size and the geometry of the loop, which needs to be considered when calculating the interference of the electron wave paths. In a spin-momentum locked material like the investigated TI, the spin accumulates a phase of 2π while progressing

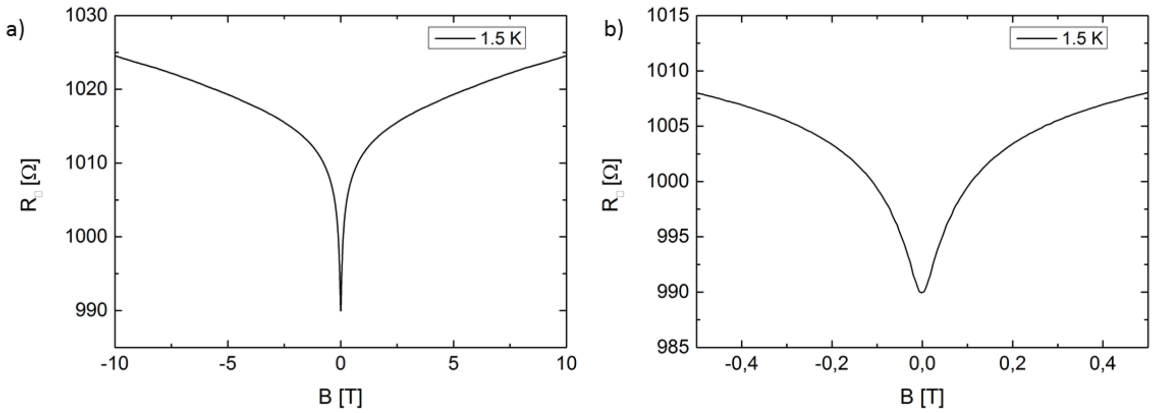

Fig. 7.6: *Characteristic WAL resistance dip in the sheet resistance R□ at 1.5 K. Graph a) illustrates the full measurement, b) highlights the region that is later used for fits.*

through the loop. Due to time reversal symmetry, this phase is acquired on the clockwise and the anticlockwise path. Combining this finding with the 4π periodicity of the fermionic wave function, destructive interference dominates. Thereby, the resistance is decreased at zero magnetic field. However, applying a magnetic field adds an additional phase, nullifying the negative WAL resistance correction [6, 81].

The dependency of the change of resistance on the magnetic field can be calculated with the Hikami-Larkin-Nagaoka (HLN) equation, that connects the magnetic field with the change in conductivity, utilizing the characteristic magnetic field B_φ [75]:

$$\Delta\sigma = \sigma(B) - \sigma(0) = -\alpha\frac{e^2}{2\pi h}\left[\ln\left(\frac{B_\varphi}{B}\right) - \psi\left(\frac{1}{2} + \frac{B_\varphi}{B}\right)\right], \quad (7.VIII)$$

$$B_\varphi = \frac{\hbar}{4el_\varphi^2}. \quad (7.IX)$$

In the equation (7.VIII), σ is the conductance, the inverse resistance, and ψ the Digamma function, the logarithmic derivative of the Gamma function Γ:

$$\psi(x) = \frac{d}{dx}\ln\Gamma(x). \quad (7.X)$$

The α in equation (7.VIII) denotes a prefactor that determines whether weak localization or weak antilocalization is present. If α = 1, WL is detected, indicating vanishing spin orbit coupling and therefore a decrease in conductance (rise in resistance). If α = -0.5, WAL is measured, with multiples of -0.5 indicating one conductance channel each. Moreover, the characteristic magnetic field B_φ can be used to determine the coherence length l_φ by utilizing equation (7.IX). In Fig. 7.6, the result of the WAL measurement, i.e. the R□ measurements, at 1.5 K is shown. The curve shows the characteristic WAL resistance dip

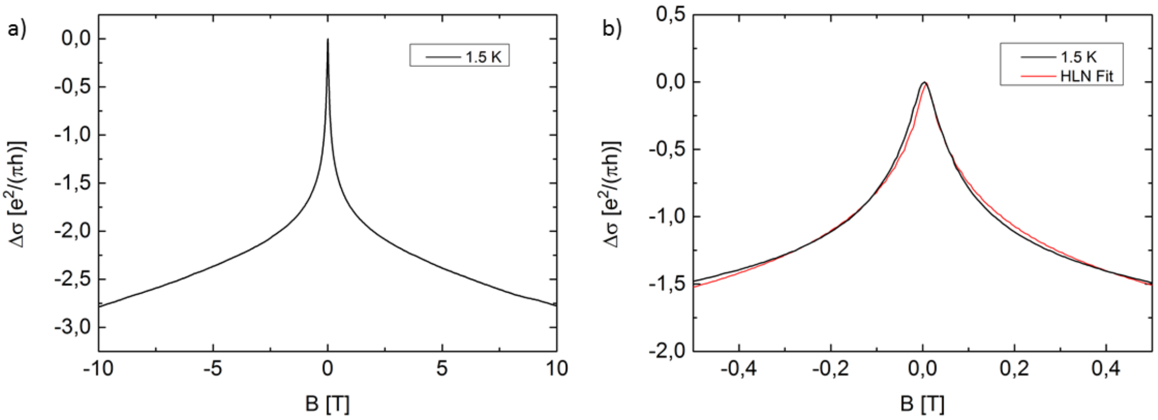

Fig. 7.7: *The graphs show $\Delta\sigma$ as a function of the magnetic field at 1.5 K on the full investigated range in a) and on the range used for fitting the HLN equation in b). a) clearly shows the WAL feature, increased conductance at low magnetic field. b) includes the HLN fit in red to acquire the coherence length.*

at low magnetic fields. From the dip, the phase coherence length of the electrons in the film can be determined by applying a fit in the form of the HLN equation to the difference in conductions, as shown in Fig. 7.7. The fit only considers magnetic fields up to |0.5| T, since the phase coherence length necessary for WAL is too short at high magnetic fields, causing the phase to shift while the electron propagates in a loop, preventing interference.

The fit in Fig. 7.7 b) reveals a spin coherence length l_φ of 222 nm at 1.5 K with an α of -0.49, indicating WAL with only one conductive channel. Whether the conductive channel lies at the interface of the thin film to the substrate, at the interface to the capping or whether a coupled channel exists cannot be determined. The size of the spin coherence length l_φ is greater than the values determined by Snelder *et al.* and Lee *et al.*, however, they measured at slightly higher temperatures [60, 80]. Therefore, in the next experiments, the temperature of the sample is varied in steps of 2.5 K to investigate the behavior of the previously measured quantities at higher temperatures. The measured Hall curves are shown in Fig. 7.8. The data show a linear behavior for all temperatures, with decreasing slopes for increasing temperatures. Due to temperature fluctuations around 0 T in the measurement setup that could not be avoided, the curves at 6.5 K and 9 K show a higher noise level than the other curves. The general behavior however is as expected, as visible in Fig. 7.8 b). Linear fits to the data result in temperature dependent charge carrier concentrations and mobilities. The results of the fits are illustrated in Fig. 7.9. As shown in the latter, the two-dimensional charge carrier density calculated from the fits to the Hall measurements increases after being almost constant until 4 K with increasing temperature, as expected, since more charge carriers are exited into the conduction band at higher temperatures. An increase in n_{2D} results in a decrease in the mobility μ due to (7.VII).

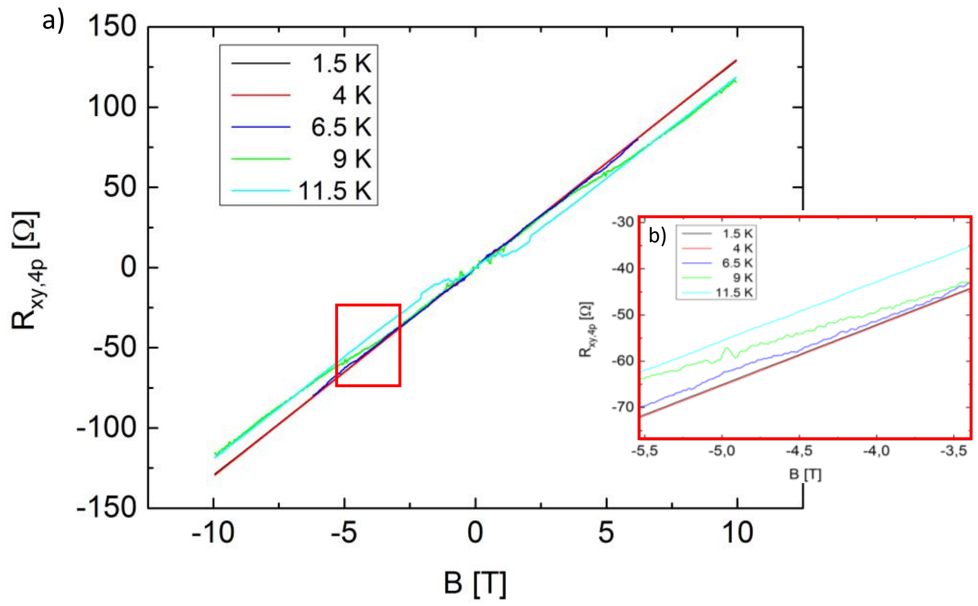

Fig. 7.8: *Graph a) shows the Hall resistance $R_{xy,4p}$ at different temperatures from 1.5 K to 11.5 K in steps of 2.5 K. b) shows the highlighted area of figure a).*

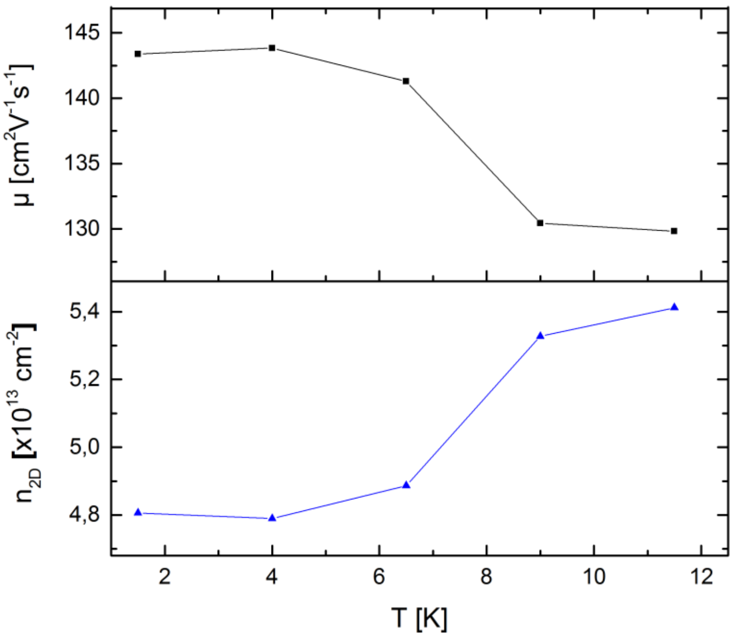

Fig. 7.9: *Temperature dependent mobility and charge carrier density, calculated from linear fits to the hall measurement data at different temperatures, see Fig. 7.8.*

However, the order of the two quantities stays at 10^{13} cm^{-2} for the charge carrier density and at 10^{2} cm^{2}V^{-1}s^{-1} for the mobility.

Temperature dependent measurements are also performed in the xx-direction, revealing the behavior of the WAL with increasing temperature. The data for the difference in conductance are shown in Fig. 7.10. As already mentioned, for 6.5 K and 9 K, irregularities

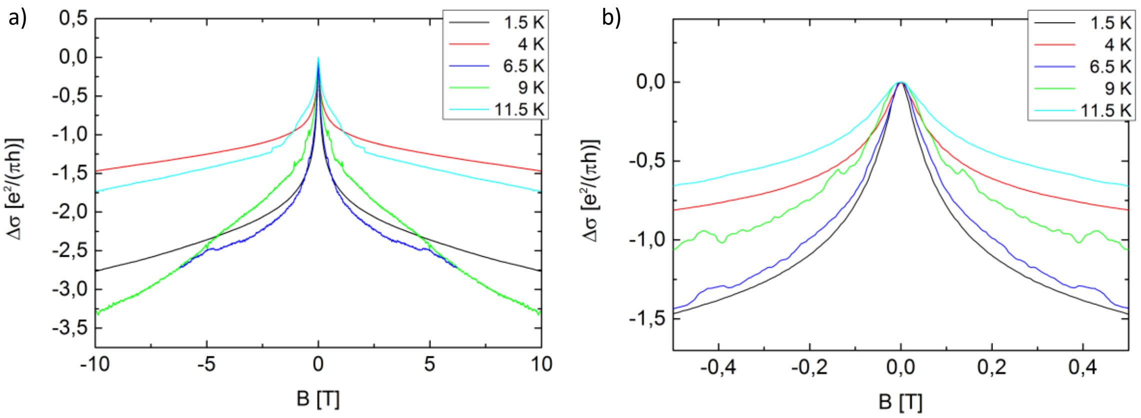

Fig. 7.10: *WAL curves for different temperatures. b) shows the range from -0.5 T to 0.5 T of a), which is also the range to which the HLN equation is fitted.*

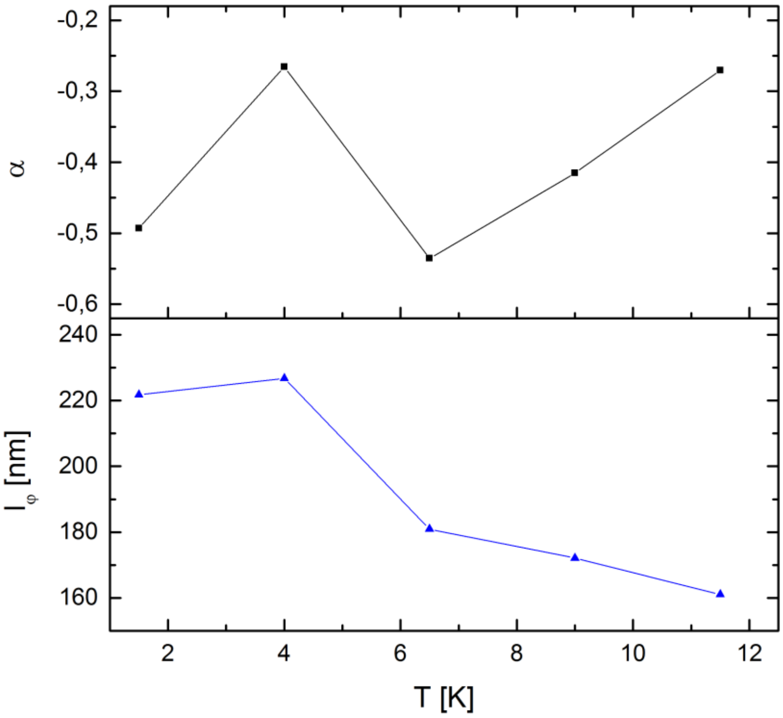

Fig. 7.11: *Temperature dependent factor α and phase coherence length l_ϕ, calculated from HLN fits to the data displayed in Fig. 7.10.*

are observed at low magnetic fields. These also arise in the $R_{xx,4p}$ measurements, but are partially filtered out by symmetrizing the data.

The curves for 1.5 K, 4 K and 11.5 K show the expected behavior of a decreasingly steep WAL characteristic, at least at low magnetic fields up to 0.5 T, shown in Fig. 7.10 b). The data for 6 K and 9.5 K show a larger noise level and also an interchanged order. HLN fits to the data yield the temperature dependent α and l_φ. The latter follows an expected behavior, a decreasing coherence length with increasing temperature, while the former fluctuates heavily between -0.5 and -0.2. The decrease in phase coherence length can be allocated to inelastic scattering, for example due to electron-electron and electron-phonon interactions that arise at higher temperatures. The fluctuations in α, especially the high value at 4 K, are unusual and no equivalent could be found in literature. The expected behavior would be an increase in α approaching 0, which can also be found in the data at higher temperatures. Since l_φ at 4K is also higher than expected by the general progression of the data, the measurements at 4K are interpreted as runaway values.

Lastly, gate measurements with the gate shown in Fig. 6.12 e) and f) are performed. By applying a voltage to the gate, an electric field is introduced that influences the position of the Fermi level in the investigated film. However, even at low applied voltages, a leaking current appeared. This indicates a short circuit in the Hall bar, either connecting the investigated film through the capping a gate dielectric with the top gate or that the dielectric is not thick enough to prevent conduction between the layers. Thus, gate dependent measurements could not be performed.

In this chapter, transport measurements of the device fabricated in chapter 6.2 were performed. The temperature dependent sheet resistance shows the behavior and resistance of an insulator, as expected from the ARPES measurements in chapter 5.2. Hall measurements at 1.5 K revealed a charge carrier density of $n_{2D} = 4.81 \cdot 10^{13}\ cm^{-2}$ and a mobility of $\mu = 143\ \mathrm{cm^2V^{-1}s^{-1}}$. The temperature dependence of the determined values follows the expected behavior, showing a decreasing mobility with increasing temperature. The magnetic field depending measurements exhibit the characteristic dip of the WAL in the resistance at zero magnetic field. Applying a HLN-fit to the data at 1.5 K reveals a phase coherence length l_φ of 222 nm, with $\alpha = 0.49$. Measurements at different temperatures yield a coherence length that decreases at higher temperatures. The value of α indicates one conductive channel, and decreases with increasing temperature. The results of the transport measurements are comparable to measurements of other groups on exfoliated TI samples, showing that the novel way of fabricating the Hall bar developed in this work can be used to create devices *in situ*. Moreover, the similar results indicate that the MBE grown quaternary film is an equivalent alternative to exfoliated flakes from single crystals [60, 80].

8 Conclusion & Outlook

The goal of the present thesis was to improve the structural and electronical quality of topological insulator thin films grown by molecular beam epitaxy and to fabricate devices with the improved films *in situ.* To do so, over the course of this master's thesis, the three significant partitions of a topological insulator device, the interface to the substrate, the bulk and the interface to the continuum, were examined.

First, the interface to the substrate was investigated. This included the choice of a fitting substrate for improved TI growths as well as considering prestructured samples to avoid *ex situ* patterning of the grown film for later experiments. The use of prestructured samples allows for the creation of sub-µm sized structures of topological insulator, imbedded into a prepatterned layer. Thus, the otherwise exposed side surfaces of the TI layer are protected. The work presented in this thesis is the conceptual continuation of T. Heider's work in his master's thesis [35]. However, the stack of the structured layer was changed and a thin interlayer of silicon oxide was introduced to relieve stress on the silicon surface, which might arise at a direct silicon to silicon nitride interface. By this method and determination of the right growth temperatures, binary TI compounds were reproducibly grown into the structures. Applying a thin interlayer of Bi_2Te_3 enabled the subsequent growth of ternary compounds into the patterns down to widths of 50 nm. If a capping is added, for example aluminum oxide, it is possible with this method to create TI structures capped on all interfaces by either substrate, nitride or capping. To additionally increase the structural quality of the TI thin film, indium phosphide was utilized as substrate. It is known from literature that Bi_2Se_3 grown on rough InP (111) exhibits high crystalline order due to a low lattice mismatch and a peculiar initial growth [16, 43]. In this work, these findings were successfully reproduced, fabricating Bi_2Se_3 films with only one domain, strongly suppressing rotated twins as proven by XRD measurements. Next, the grown Bi_2Se_3 was used as a highly ordered pseudo substrate. Quaternary TI compounds grown onto the pseudo substrate exhibit the same domain reduced crystalline structure. This proved that using a lattice matched substrate and a thin structurally improved pseudo substrate positively influences the final film. The effect is present even though the van-der-Waals growth of the TI supposedly cancels disadvantageous initial conditions, for example the lattice mismatch to silicon of roughly 14 %.

To improve the electronic qualities of the bulk of MBE grown TIs for transport measurements, this work concentrated on fabricating a quaternary topological insulator. Quaternary tetradymite TIs promise low crystal defect contributions to transport, due to the unique way the atoms are arranged in the quintuple layers of the crystal structure. Moreover, the variation of Bi/Sb and Te/Se enables shiftability of the position of the Fermi level of the TI with respect to the Dirac cone. Thus, the Fermi level can be moved into the band gap and close to the Dirac point by changing the ratio between the elements. Quaternary compounds with a composition following $Bi_xSb_{2-x}Te_ySe_{3-y}$ had been studied before, however were grown by the Bridgman method only, resulting in comparatively large single crystals of which flakes need to be exfoliated [59, 60, 79]. There, however, exists no literature of an MBE grown quaternary TI. To exploit these promising features of the quaternary for transport measurements, first the $Bi_2Te_xSe_{3-y}$ system was grown to establish whether a blend of Te and Se in one compound is realizable in the MBE of the PGI-9. By optimizing the source temperatures, $Bi_2Te_xSe_{3-y}$ alloys with variable compositions were grown. Adding Sb with effusion temperatures known from the $Bi_xSb_{2-x}Te_3$ compound, that had already been grown in the chamber by M. Lanius [40], resulted in a $Bi_{1.4}Sb_{0.6}Te_{1.7}Se_{1.3}$ compound, comparable to those used for exfoliation. Moreover, the previously mentioned effectiveness of the structurally improved pseudo substrate was proven with this compound. To investigate the crystalline and electronic qualities of the TI, XRD and ARPES measurements were performed. The XRD data revealed a tetradymite crystal structure with lattice parameters a = 4.285 Å and c = 29.95 Å, intermediate to the lattice parameters of the binary compounds, suggesting an alloy of them. ARPES measurements showed a distinct Dirac cone in the band gap, roughly 160 meV beneath the Fermi energy. The latter results not only showed that a quaternary TI had been successfully produced, but also that the crystalline quality is good enough to show the band structure even at room temperature. In conclusion, the MBE growth of a quaternary topological insulator was achieved, with high crystalline quality, especially in combination with the InP/Bi_2Se_3 pseudo substrate, and with a Dirac cone situated in the band gap.

Lastly, the interface of the TI to the environment was examined. It had been shown by multiple groups that exposing a TI to ambient conditions results in structural changes, leading to unintended alterations in crystalline and electronic properties of the TI [65, 66, 82]. These effects can be prevented by applying a capping to the film, protecting it from environmental influences. However, to structure the films for transport measurements, chemical and physical processes are utilized, potentially destroying the capping. To bypass these processes, the stencil lithography technique developed by P. Schüffelgen and D. Rosenbach was utilized, but refined by designing new holders [72, 75]. Using self-made structured membranes consisting of silicon nitride placed under the substrate during growth, metallic contact pads were grown *in situ* on the previously fabricated TI film. Thus, the interface between pad and film is supposedly pristine, promising a high-quality interface for transport measurements. The membrane masks were fabricated by KOH etching and had Hall bar structures and sub-µm structures imbedded. In this work, it was shown that the masks can be used to fabricate neat *in situ* Hall bar contacts consisting of Ti and Al, as well as sub-µm structures for continuative experiments ([5, 77]), while protecting the TI with a capping.

To further investigate the quality of the, via stencil lithography deposited, contacts and the electronic properties of the quaternary, Hall measurements were performed in the VTI of PGI-9. Measurements at 1.5 K exhibited high resistances of the film, which showed the temperature dependent behavior of an insulator, confirming the results of the ARPES data. The determined two-dimensional charge carrier density n_{2D} = $4.81 \cdot 10^{13}\ cm^{-2}$ as well as the mobility $\mu = 143\ \mathrm{cm^2V^{-1}s^{-1}}$ are comparable to values found in literature, verifying that the MBE grown quaternary is capable of competing with exfoliated flakes [60, 80]. Measurements of the sheet resistance during magnetic field swipes revealed the characteristic WAL resistance correction at low magnetic fields. Applying a HLN fit resulted in a phase coherence length l_φ of $222\ \mathrm{nm}$ at 1.5 K and an α-factor of -0.49, which confirmed the WAL behavior with one conductive channel. Temperature dependent transport experiments showed an expected increase in n_{2D} due to excitation of carriers and a decrease in μ and l_φ, a result of enhanced scattering. Unfortunately, gate measurements were not possible due to current leaks through the gate dielectric.

As a conclusion, it was shown that quaternary TIs can be grown selectively and structurally improved with the right choice of substrate in an MBE, which had not been achieved before, and contacts for transport measurements can be added *in situ*, resulting in transport data comparable to findings on exfoliated samples.

Outlook

In the future, many further experiments that could not be performed in the frame of this thesis, can and should be conducted. This includes low temperature ARPES measurements of the quaternary TI for higher resolution, as well as TEM studies of the growth of the quaternary TI on the InP/Bi_2Se_3 pseudo substrate to investigate the interface between the binary and quaternary TI. Moreover, gated transport investigations can reveal further information about the band gap and the electronic structure of the TI. The most interesting and promising experiment that could not be performed in this thesis however is the combination of all the established processes. An InP substrate would be covered with SiO_2 and Si_3N_4, which would be patterned into a Hall bar or sub-µm structure as in chapter 4. By growing a Bi_2Se_3 pseudo substrate with subsequent quaternary on top, a Hall bar or sub-µm structure supposedly consisting of rotated domain suppressed TI would be fabricated. Aligning the mask with the prepatterned structure, depositing contacts and subsequent capping would then result in a device of high quality, capped to all sides as well as structurally and electronically improved.

When these procedures are established, it is possible to consider advanced experiments to investigate the nature of topological insulators, especially with respect to Majorana physics. By applying *in situ* contacts of superconductive materials onto a structured TI, it should be possible to examine hybridized Majorana modes in the tertradymite TIs, as Albrecht *et al.* did on InAs nanowires [5]. Using an STM, the characteristic length of zero-energy states and therefore Majorana signatures can be investigated. Moreover, by growing thin TI films into the structures, it is possible to investigate the behavior of quasi two-dimensional TIs. At very low thicknesses below 6 quintuple layers (roughly 6 nm), the top and bottom surface states of the TI hybridize, as shown by Zhang *et al.* in [83]. Thus, the TI exhibits gapped surface states on the two surfaces, creating a topology protected quantum spin hall system with one-dimensional edge states on the remaining surfaces. This system shows similar qualities to those fabricated by Molenkamp *et al.* in HgTe/CdTe quantum wells [14, 84, 85]. So far, repeating the experiments of the latter on ultrathin MBE grown films was not successful, since the films oxidized fully. This destroyed the edge channels and prevented transport experiments. However, using the techniques developed and refined in this work, repeating the experiments on capped tetradymite TI systems protected from oxidation should come in reach. Additionally, by applying superconducting contacts or ferromagnetic insulators to the sides of such a quasi two-dimensional topological insulator, it is proposed to be possible to gap the edge states, creating located Majorana zero modes [86, 87]. These can then be moved, or braided, by magnetic fluxes, allowing for the demonstration of non-abelian exchange statistics [88, 89]. Thus, by fabricating capped quasi two-dimensional QSH systems from thin topological insulators via the techniques presented in this work and combining them with superconductors or magnetic insulators, it is possible to create, manipulate and therefore braid Majorana zero modes. Using the non-abelian exchange statistics possible with this braiding, unitary gate operations can be performed. These operations are robust to decoherence and an important requirement to pave the way to topological quantum computation [90, 91].

9 References

1. Kane, C.L., Mele, E.J.: Quantum spin Hall effect in graphene. Physical review letters (2005). doi: 10.1103/PhysRevLett.95.226801
2. Ando, Y.: Topological Insulator Materials. J. Phys. Soc. Jpn. (2013). doi: 10.7566/JPSJ.82.102001
3. Sato, M., Ando, Y.: Topological superconductors: a review. Reports on progress in physics. Physical Society (Great Britain) (2017). doi: 10.1088/1361-6633/aa6ac7
4. Beenakker, C.: Search for Majorana Fermions in Superconductors. Annu. Rev. Condens. Matter Phys. (2013). doi: 10.1146/annurev-conmatphys-030212-184337
5. Albrecht, S.M., Higginbotham, A.P., Madsen, M., Kuemmeth, F., Jespersen, T.S., Nygård, J., Krogstrup, P., Marcus, C.M.: Exponential protection of zero modes in Majorana islands. Nature (2016). doi: 10.1038/nature17162
6. Schäpers, T.: Semiconductor Spintronics, 1st edn. De Gruyter Textbook. Walter de Gruyter GmbH Co.KG, s.l. (2016)
7. Moore, J.E.: The birth of topological insulators. Nature (2010). doi: 10.1038/nature08916
8. Roy, A., DiVincenzo, D.P.: Topological Quantum Computing (2017)
9. Bernevig, B.A., Hughes, T.L., Zhang, S.-C.: Quantum spin Hall effect and topological phase transition in HgTe quantum wells. Science (New York, N.Y.) (2006). doi: 10.1126/science.1133734
10. Fu, L., Kane, C.L.: Superconducting proximity effect and majorana fermions at the surface of a topological insulator. Physical review letters (2008). doi: 10.1103/PhysRevLett.100.096407
11. Wang, J., Chang, C.-Z., Li, H., He, K., Zhang, D., Singh, M., Ma, X.-C., Samarth, N., Xie, M., Xue, Q.-K., Chan, M.H.W.: Interplay between topological insulators and superconductors. Phys. Rev. B (2012). doi: 10.1103/PhysRevB.85.045415
12. Ringel, Z., Kraus, Y.E., Stern, A.: Strong side of weak topological insulators. Phys. Rev. B (2012). doi: 10.1103/PhysRevB.86.045102
13. Eschbach, M., Lanius, M., Niu, C., Młyńczak, E., Gospodarič, P., Kellner, J., Schüffelgen, P., Gehlmann, M., Döring, S., Neumann, E., Luysberg, M., Mussler, G., Plucinski, L., Morgenstern, M., Grützmacher, D., Bihlmayer, G., Blügel, S., Schneider,

C.M.: Bi1Te1 is a dual topological insulator. Nature communications (2017). doi: 10.1038/ncomms14976

14. Maier, L., Oostinga, J.B., Knott, D., Brüne, C., Virtanen, P., Tkachov, G., Hankiewicz, E.M., Gould, C., Buhmann, H., Molenkamp, L.W.: Induced superconductivity in the three-dimensional topological insulator HgTe. Physical review letters (2012). doi: 10.1103/PhysRevLett.109.186806
15. Fu, L., Kane, C.L., Mele, E.J.: Topological insulators in three dimensions. Physical review letters (2007). doi: 10.1103/PhysRevLett.98.106803
16. Ginley, T., Wang, Y., Law, S.: Topological Insulator Film Growth by Molecular Beam Epitaxy. A Review. Crystals (2016). doi: 10.3390/cryst6110154
17. Eschbach, M.: Band Structure Engineering in 3D Topological Insulators Investigated by Angle-Resolved Photoemission Spectroscopy. Ph.D. Thesis (2016)
18. Blügel, S. (ed.): Topological matter - topological insulators, skyrmions and majoranas. Lecture notes of the 48th IFF Spring School 2017. Schriften des Forschungszentrums Jülich : […], Reihe Schlüsseltechnologien, volume 139. Forschungszentrum Jülich GmbH, Zentralbibliothek, Verlag, Jülich (2017)
19. Rosenbach, D.: Induced superconductivity in molecular beam epitaxy grown topological insulator thin films. Master's Thesis (2016)
20. Thouless, D.J., Kohmoto, M., Nightingale, M.P., den Nijs, M.: Quantized Hall Conductance in a Two-Dimensional Periodic Potential. Phys. Rev. Lett. (1982). doi: 10.1103/PhysRevLett.49.405
21. Haldane, F.D.M.: Nonlinear Field Theory of Large-Spin Heisenberg Antiferromagnets. Semiclassically Quantized Solitons of the One-Dimensional Easy-Axis Néel State. Phys. Rev. Lett. (1983). doi: 10.1103/PhysRevLett.50.1153
22. Klitzing, K.v., Dorda, G., Pepper, M.: New Method for High-Accuracy Determination of the Fine-Structure Constant Based on Quantized Hall Resistance. Phys. Rev. Lett. (1980). doi: 10.1103/PhysRevLett.45.494
23. Morgenstern, M.: Solid State Physics II: Interactions and Topology. Script, RWTH Aachen (2016)
24. Kane, C.L., Mele, E.J.: Z2 topological order and the quantum spin Hall effect. Phys. Rev. Lett. (2005). doi: 10.1103/PhysRevLett.95.146802

25. Markov, I.V.: Crystal growth for beginners. Fundamentals of nucleation, crystal growth and epitaxy. World Scientific, Singapore (1996)
26. Frank, F.C., van der Merwe, J. H.: One-Dimensional Dislocations. I. Static Theory. Proceedings of the Royal Society A: Mathematical, Physical and Engineering Sciences (1949). doi: 10.1098/rspa.1949.0095
27. Volmer, M., Weber, A.: Keimbildung in übersättigten Gebilden. Zeitschrift für Physikalische Chemie (1926). doi: 10.1515/zpch-1926-11927
28. Lanius, M.: Topological Insulating Tellurides: How to tune Doping, Topology, and Dimensionality. PhD Thesis (2017)
29. Stranski, I.N.: Beitrag zur Theorie der orientierten Ausscheidung von Ionenkristallen aufeinander und zur Frage der Bildung von Grimmschen Mischkristallen. Zeitschrift für Physikalische Chemie (1931). doi: 10.1515/zpch-1931-s124
30. Bauer, E.: Phänomenologische Theorie der Kristallabscheidung an Oberflächen. I. Zeitschrift für Kristallographie (1958). doi: 10.1524/zkri.1958.110.1-6.372
31. Koma, A.: Van der Waals epitaxy—a new epitaxial growth method for a highly lattice-mismatched system. Thin Solid Films (1992). doi: 10.1016/0040-6090(92)90872-9
32. Tarakina, N.V., Schreyeck, S., Borzenko, T., Schumacher, C., Karczewski, G., Brunner, K., Gould, C., Buhmann, H., Molenkamp, L.W.: Comparative Study of the Microstructure of Bi 2 Se 3 Thin Films Grown on Si(111) and InP(111) Substrates. Crystal Growth & Design (2012). doi: 10.1021/cg201636g
33. Kampmeier, J., Weyrich, C., Lanius, M., Schall, M., Neumann, E., Mussler, G., Schäpers, T., Grützmacher, D.: Selective area growth of Bi2Te3 and Sb2Te3 topological insulator thin films. Journal of Crystal Growth (2016). doi: 10.1016/j.jcrysgro.2016.03.012
34. Kim, D., Cho, S., Butch, N.P., Syers, P., Kirshenbaum, K., Adam, S., Paglione, J., Fuhrer, M.S.: Surface conduction of topological Dirac electrons in bulk insulating Bi2Se3. Nat Phys (2012). doi: 10.1038/nphys2286
35. Heider, T.R.M.: Magnetotransport measurements on selectively grown Telluriumbased Topological Insulator nanoribbons. Master's Thesis, RWTH Aachen (2015)

36. Rajagopalan, N., Han, X., Park, J.A., Kiyohara, T., Park, S., Kim, B.H.: PECVD oxide-nitride and oxide-silicon stacks for 3D memory application
37. Isomae, S.: Stress in silicon at Si 3 N 4 /SiO 2 film edges and viscoelastic behavior of SiO 2 films. Journal of Applied Physics (1985). doi: 10.1063/1.334791
38. Schmitt, T.: Low-dimensional Josephson junctions based on molecular beam epitaxy grown topolgical insulator thin films. Master's thesis, RWTH Aachen (2017)
39. Lanius, M., Kampmeier, J., Kölling, S., Mussler, G., Koenraad, P.M., Grützmacher, D.: Topography and structure of ultrathin topological insulator Sb 2 Te 3 films on Si(111) grown by means of molecular beam epitaxy. Journal of Crystal Growth (2016). doi: 10.1016/j.jcrysgro.2016.08.016
40. Kellner, J., Eschbach, M., Kampmeier, J., Lanius, M., Młyńczak, E., Mussler, G., Holländer, B., Plucinski, L., Liebmann, M., Grützmacher, D., Schneider, C.M., Morgenstern, M.: Tuning the Dirac point to the Fermi level in the ternary topological insulator (Bi 1−x Sb x) 2 Te 3. Appl. Phys. Lett. (2015). doi: 10.1063/1.4938394
41. Lanius, M., Kampmeier, J., Weyrich, C., Kölling, S., Schall, M., Schüffelgen, P., Neumann, E., Luysberg, M., Mussler, G., Koenraad, P.M., Schäpers, T., Grützmacher, D.: P–N Junctions in Ultrathin Topological Insulator Sb 2 Te 3 /Bi 2 Te 3 Heterostructures Grown by Molecular Beam Epitaxy. Crystal Growth & Design (2016). doi: 10.1021/acs.cgd.5b01717
42. Borisova, S., Krumrain, J., Luysberg, M., Mussler, G., Grützmacher, D.: Mode of Growth of Ultrathin Topological Insulator Bi 2 Te 3 Films on Si (111) Substrates. Crystal Growth & Design (2012). doi: 10.1021/cg301236s
43. Schreyeck, S., Tarakina, N.V., Karczewski, G., Schumacher, C., Borzenko, T., Brüne, C., Buhmann, H., Gould, C., Brunner, K., Molenkamp, L.W.: Molecular beam epitaxy of high structural quality Bi 2 Se 3 on lattice matched InP(111) substrates. Appl. Phys. Lett. (2013). doi: 10.1063/1.4789775
44. Tarakina, N.V., Schreyeck, S., Borzenko, T., Grauer, S., Schumacher, C., Karczewski, G., Gould, C., Brunner, K., Buhmann, H., Molenkamp, L.W.: Microstructural characterisation of Bi 2 Se 3 thin films. J. Phys.: Conf. Ser. (2013). doi: 10.1088/1742-6596/471/1/012043

45. Takagaki, Y., Papadogianni, A., Jenichen, B., Jahn, U., Bierwagen, O.: Step-bunched Bi2Te3 and Bi2Se3 layers epitaxially grown on high-index InP substrates. Thin Solid Films (2015). doi: 10.1016/j.tsf.2015.03.027
46. Wang, Z.Y., Li, H.D., Guo, X., Ho, W.K., Xie, M.H.: Growth characteristics of topological insulator Bi2Se3 films on different substrates. Journal of Crystal Growth (2011). doi: 10.1016/j.jcrysgro.2011.08.029
47. Tarakina, N.V., Schreyeck, S., Luysberg, M., Grauer, S., Schumacher, C., Karczewski, G., Brunner, K., Gould, C., Buhmann, H., Dunin-Borkowski, R.E., Molenkamp, L.W.: Suppressing Twin Formation in Bi 2 Se 3 Thin Films. Adv. Mater. Interfaces (2014). doi: 10.1002/admi.201400134
48. Xie, M.-H., Guo, X., Xu, Z.-J., Ho, W.-K.: Molecular-beam epitaxy of topological insulator Bi 2 Se 3 (111) and (221) thin films. Chinese Phys. B (2013). doi: 10.1088/1674-1056/22/6/068101
49. AXT, I.: Semi-Insulating InP. http://www.axt.com/site/index.php?q=node/35. Accessed 26 October 2016
50. Fu, L., Kane, C.L.: Topological insulators with inversion symmetry. Phys. Rev. B (2007). doi: 10.1103/PhysRevB.76.045302
51. Zhang, H., Liu, C.-X., Qi, X.-L., Dai, X., Fang, Z., Zhang, S.-C.: Topological insulators in Bi2Se3, Bi2Te3 and Sb2Te3 with a single Dirac cone on the surface. Nat Phys (2009). doi: 10.1038/nphys1270
52. Maaß, H., Schreyeck, S., Schatz, S., Fiedler, S., Seibel, C., Lutz, P., Karczewski, G., Bentmann, H., Gould, C., Brunner, K., Molenkamp, L.W., Reinert, F.: Electronic structure and morphology of epitaxial Bi 2 Te 2 Se topological insulator films. Journal of Applied Physics (2014). doi: 10.1063/1.4902010
53. Ren, Z., Taskin, A.A., Sasaki, S., Segawa, K., Ando, Y.: Large bulk resistivity and surface quantum oscillations in the topological insulator Bi2Te2Se. Phys. Rev. B (2010). doi: 10.1103/PhysRevB.82.241306
54. Weyrich, C., Drögeler, M., Kampmeier, J., Eschbach, M., Mussler, G., Merzenich, T., Stoica, T., Batov, I.E., Schubert, J., Plucinski, L., Beschoten, B., Schneider, C.M., Stampfer, C., Grützmacher, D., Schäpers, T.: Growth, characterization, and transport properties of ternary (Bi1-x Sb x)2Te3 topological insulator layers. Journal of

physics. Condensed matter : an Institute of Physics journal (2016). doi: 10.1088/0953-8984/28/49/495501

55. Arakane, T., Sato, T., Souma, S., Kosaka, K., Nakayama, K., Komatsu, M., Takahashi, T., Ren, Z., Segawa, K., Ando, Y.: Tunable Dirac cone in the topological insulator Bi(2-x)Sb(x)Te(3-y)Se(y). Nature communications (2012). doi: 10.1038/ncomms1639
56. Lohani, H., Mishra, P., Banerjee, A., Majhi, K., Ganesan, R., Manju, U., Topwal, D., Kumar, P.S.A., Sekhar, B.R.: Band Structure of Topological Insulator BiSbTe1.25Se1.75. Scientific reports (2017). doi: 10.1038/s41598-017-04985-y
57. Ko, W., Jeon, I., Kim, H.W., Kwon, H., Kahng, S.-J., Park, J., Kim, J.S., Hwang, S.W., Suh, H.: Atomic and electronic structure of an alloyed topological insulator, Bi1.5Sb0.5Te1.7Se1.3. Scientific reports (2013). doi: 10.1038/srep02656
58. Wang, W., Li, L., Zou, W., He, L., Song, F., Zhang, R., Wu, X., Zhang, F.: Intrinsic topological insulator Bi(1.5)Sb(0.5)Te(3-x)Se(x) thin crystals. Scientific reports (2015). doi: 10.1038/srep07931
59. Ren, Z., Taskin, A.A., Sasaki, S., Segawa, K., Ando, Y.: Optimizing Bi2−xSbxTe3−ySey solid solutions to approach the intrinsic topological insulator regime. Phys. Rev. B (2011). doi: 10.1103/PhysRevB.84.165311
60. Snelder, M., Molenaar, C.G., Pan, Y., Wu, D., Huang, Y.K., Visser, A. de, Golubov, A.A., van der Wiel, W G, Hilgenkamp, H., Golden, M.S., Brinkman, A.: Josephson supercurrent in a topological insulator without a bulk shunt. Supercond. Sci. Technol. (2014). doi: 10.1088/0953-2048/27/10/104001
61. Pan, Y., Wu, D., Angevaare, J.R., Luigjes, H., Frantzeskakis, E., Jong, N.d., van Heumen, E., Bay, T.V., Zwartsenberg, B., Huang, Y.K., Snelder, M., Brinkman, A., Golden, M.S., Visser, A. de: Low carrier concentration crystals of the topological insulator Bi 2− x Sb x Te 3− y Se y. A magnetotransport study. New J. Phys. (2014). doi: 10.1088/1367-2630/16/12/123035
62. Wang, W., Zou, W.Q., He, L., Peng, J., Zhang, R., Wu, X.S., Zhang, F.M.: Magnetoresistance and nonlinear Hall effect in quaternary topological insulator Bi 1.5 Sb 0.5 Te 1.8 Se 1.2. J. Phys. D: Appl. Phys. (2015). doi: 10.1088/0022-3727/48/20/205305
63. Stehno, M.P., Hendrickx, N.W., Snelder, M., Scholten, T., Huang, Y.K., Golden, M.S., Brinkman, A.: Conduction spectroscopy of a proximity induced superconducting

topological insulator. Semicond. Sci. Technol. (2017). doi: 10.1088/1361-6641/aa7f88

64. Park, K., Beule, C.D., Partoens, B.: The ageing effect in topological insulators. Evolution of the surface electronic structure of Bi 2 Se 3 upon K adsorption. New J. Phys. (2013). doi: 10.1088/1367-2630/15/11/113031
65. Green, A.J., Dey, S., An, Y.Q., O'Brien, B., O'Mullane, S., Thiel, B., Diebold, A.C.: Surface oxidation of the topological insulator Bi 2 Se 3. Journal of Vacuum Science & Technology A: Vacuum, Surfaces, and Films (2016). doi: 10.1116/1.4964637
66. Kong, D., Cha, J.J., Lai, K., Peng, H., Analytis, J.G., Meister, S., Chen, Y., Zhang, H.-J., Fisher, I.R., Shen, Z.-X., Cui, Y.: Rapid surface oxidation as a source of surface degradation factor for Bi_2Se_3. ACS nano (2011). doi: 10.1021/nn200556h
67. Hoefer, K., Becker, C., Rata, D., Swanson, J., Thalmeier, P., Tjeng, L.H.: Intrinsic conduction through topological surface states of insulating Bi2Te3 epitaxial thin films. Proceedings of the National Academy of Sciences of the United States of America (2014). doi: 10.1073/pnas.1410591111
68. Fornari, C.I., Rappl, P.H.O., Morelhão, S.L., Peixoto, T.R.F., Bentmann, H., Reinert, F., Abramof, E.: Preservation of pristine Bi 2 Te 3 thin film topological insulator surface after ex situ mechanical removal of Te capping layer. APL Materials (2016). doi: 10.1063/1.4964610
69. Virwani, K., Harrison, S.E., Pushp, A., Topuria, T., Delenia, E., Rice, P., Kellock, A., Collins-McIntyre, L., Harris, J., Hesjedal, T., Parkin, S.: Controlled removal of amorphous Se capping layer from a topological insulator. Appl. Phys. Lett. (2014). doi: 10.1063/1.4904803
70. Lang, M., He, L., Xiu, F., Yu, X., Tang, J., Wang, Y., Kou, X., Jiang, W., Fedorov, A.V., Wang, K.L.: Revelation of topological surface states in Bi2Se3 thin films by in situ Al passivation. ACS nano (2012). doi: 10.1021/nn204239d
71. Ngabonziza, P., Stehno, M.P., Myoren, H., Neumann, V.A., Koster, G., Brinkman, A.: Gate-Tunable Transport Properties of In Situ Capped Bi 2 Te 3 Topological Insulator Thin Films. Adv. Electron. Mater. (2016). doi: 10.1002/aelm.201600157
72. Schüffelgen, P., Rosenbach, D., Neumann, E., Stehno, M.P., Lanius, M., Zhao, J., Wang, M., Sheehan, B., Schmidt, M., Gao, B., Brinkman, A., Mussler, G., Schäpers, T., Grützmacher, D.: Stencil lithography of superconducting contacts on MBE-grown

topological insulator thin films. Journal of Crystal Growth (2017). doi: 10.1016/j.jcrysgro.2017.03.035

73. Powell, O., Sweatman, D., Harrison, H.B.: The use of titanium and titanium dioxide as masks for deep silicon etching. Smart Mater. Struct. (2006). doi: 10.1088/0964-1726/15/1/013
74. Gemelli, E., Camargo, N.: Oxidation kinetics of commercially pure titanium. Matéria (Rio J.) (2007). doi: 10.1590/S1517-70762007000300014
75. Rosenbach, D.: Fabrication and characterization of topological insulator devices with aluminum oxide capping. Intership report, University of Twente (2016)
76. Hackemüller, F.J.: Halbleiternanodrahtproben für die Elektronenholographie: Präparation und Transportmessungen. Master's Thesis, RWTH Aachen (2015)
77. Akzyanov, R.S., Rozhkov, A.V., Rakhmanov, A.L., Nori, F.: Tunneling spectrum of a pinned vortex with a robust Majorana state. Phys. Rev. B (2014). doi: 10.1103/PhysRevB.89.085409
78. Sato, K., Shikida, M., Matsushima, Y., Yamashiro, T., Asaumi, K., Iriye, Y., Yamamoto, M.: Characterization of orientation-dependent etching properties of single-crystal silicon. Effects of KOH concentration. Sensors and Actuators A: Physical (1998). doi: 10.1016/S0924-4247(97)01658-0
79. Zhang, J., Chang, C.-Z., Zhang, Z., Wen, J., Feng, X., Li, K., Liu, M., He, K., Wang, L., Chen, X., Xue, Q.-K., Ma, X., Wang, Y.: Band structure engineering in (Bi(1-x)Sb(x))(2)Te(3) ternary topological insulators. Nature communications (2011). doi: 10.1038/ncomms1588
80. Lee, J., Park, J., Lee, J.-H., Kim, J.S., Lee, H.-J.: Gate-tuned differentiation of surface-conducting states in Bi 1.5 Sb 0.5 Te 1.7 Se 1.3 topological-insulator thin crystals. Phys. Rev. B (2012). doi: 10.1103/PhysRevB.86.245321
81. Bergmann, G.: Weak anti-localization—An experimental proof for the destructive interference of rotated spin. Solid State Communications (1982). doi: 10.1016/0038-1098(82)90013-8
82. Hoefer, K., Becker, C., Wirth, S., Hao Tjeng, L.: Protective capping of topological surface states of intrinsically insulating Bi 2 Te 3. AIP Advances (2015). doi: 10.1063/1.4931038

83. Zhang, Y., He, K., Chang, C.-Z., Song, C.-L., Wang, L.-L., Chen, X., Jia, J.-F., Fang, Z., Dai, X., Shan, W.-Y., Shen, S.-Q., Niu, Q., Qi, X.-L., Zhang, S.-C., Ma, X.-C., Xue, Q.-K.: Crossover of the three-dimensional topological insulator Bi2Se3 to the two-dimensional limit. Nat Phys (2010). doi: 10.1038/nphys1779
84. Oostinga, J.B., Maier, L., Schüffelgen, P., Knott, D., Ames, C., Brüne, C., Tkachov, G., Buhmann, H., Molenkamp, L.W.: Josephson Supercurrent through the Topological Surface States of Strained Bulk HgTe. Phys. Rev. X (2013). doi: 10.1103/PhysRevX.3.021007
85. Bocquillon, E., Deacon, R.S., Wiedenmann, J., Leubner, P., Klapwijk, T.M., Brüne, C., Ishibashi, K., Buhmann, H., Molenkamp, L.W.: Gapless Andreev bound states in the quantum spin Hall insulator HgTe. Nature nanotechnology (2017). doi: 10.1038/nnano.2016.159
86. van Heck, B., Hyart, T., Beenakker, C.W.J.: Minimal circuit for a flux-controlled Majorana qubit in a quantum spin-Hall insulator. Phys. Scr. (2015). doi: 10.1088/0031-8949/2015/T164/014007
87. Liu, C., Jia, J.-F.: Creating Majorana fermions in topological insulators. National Science Review (2014). doi: 10.1093/nsr/nwt036
88. van Heck, B., Akhmerov, A.R., Hassler, F., Burrello, M., Beenakker, C.W.J.: Coulomb-assisted braiding of Majorana fermions in a Josephson junction array. New J. Phys. (2012). doi: 10.1088/1367-2630/14/3/035019
89. Mi, S., Pikulin, D.I., Wimmer, M., Beenakker, C.W.J.: Proposal for the detection and braiding of Majorana fermions in a quantum spin Hall insulator. Phys. Rev. B (2013). doi: 10.1103/PhysRevB.87.241405
90. Sarma, S.D., Freedman, M., Nayak, C.: Majorana zero modes and topological quantum computation. npj Quantum Inf (2015). doi: 10.1038/npjqi.2015.1
91. Freedman, M.H., Kitaev, A., Larsen, M.J., Wang, Z.: Topological quantum computation. Bull. Amer. Math. Soc. (2003). doi: 10.1090/S0273-0979-02-00964-3

10 Acknowledgments

Many people helped and supported me during my studies and my time in Jülich and in this section, I want to thank them for what they have done for me.

First of all, I want to thank Prof. Dr. Grützmacher for giving me the opportunity of working and writing my thesis at his institute.

Special thanks go to the best supervisor and motivator there is: Peter Schüffelgen. Without his knowledge of the topic, his never ending ideas and solutions, him always having time to discuss problems and his all-around optimistic attitude, my time in the FZ would only have been a tenth of the fun, most probably even less.

Tobias Schmitt I want to thank for being a great, cookie supplying, office mate and for the many fun and fruitful discussions about processes, growths and about other things happening in the FZ.

I want to thank Daniel Rosenbach for helping me with the transport measurements and the evaluation of the data, as well as the for the discussions about both and other topics.

I am very thankful to Dr. Gregor Mussler for all the XRD work he did and especially for always having an open ear about problems at the MBE. Also I want to thank Jalil for helping me out and the fruitful discussions about working at the MBE.

I want to thank Prof. Dr. Thomas Schäpers for letting me use his cryostat and especially Christian Weyrich for supporting me with words and deeds during the transport measurements.

Also, I want to thank Jonas Kölzer, Pujitha Perla, Saher Abusulaiman and Meng “Meng Meng” Wang for being great colleagues and generally people who talking with is always great fun.

I am very grateful to Denis Rainko, Konstantin Mertens and Niels von den Driesch for the great RBS measurements, without which the quaternary could not have been realized.

I want to thank Tristan Heider for the excellent ARPES measurements and also for carrying the vacuum suitcase to our lab. Moreover, I am grateful to Lidia Kibkalo for the nice TEM measurements.

I want to thank Stefan Trellenkamp and Mona Nonn for their reliable and fast electron beam lithography work and optical lithography mask fabrication, respectively. Benjamin Bennemann and Christoph Krause I want to thank for their cooperation during vacuum transfers.

I want to thank the HNF staff for their great work of keeping the cleanroom in perfect condition. Special thanks go to Elmar Neumann for maintaining the SEMs, Stephi Bunte for her work on the saw and Irina Kempf for keeping an eye on me at WB 11.

Naturally, I want to thank my family and friends for supporting me during my studies and my thesis, particularly Gregor, who also proofread this thesis and motivated me not to go to lectures after long nights.

Most importantly I want to thank my girlfriend Jenny, who supported me throughout my whole studies and especially during my theses. Without her being my motivation, I probably would have never finished my studies, or anything in general.